ulm university universität ulm

Paving the Way for Structure Mapping Measurements of Biological Macromolecules Using a Single Quantum Sensor

DISSERTATION

zur Erlangung des Doktorgrades Dr. rer. nat.
der Fakultät für Naturwissenschaften der Universität Ulm

vorgelegt von
Timo Benjamin Weggler
aus Weißenhorn
2020

Amtierender Dekan:	Prof. Dr. Thorsten Bernhardt
Erstgutachter:	Prof. Dr. Jens Michaelis
Zweitgutachter:	Prof. Dr. Fedor Jelezko
Tag der Prüfung:	28.April 2021

Abstract

This thesis is working towards the development of a new method in the field of structure determination of biomolecules. Until now, single molecule Förster resonance energy transfer (smFRET) represents the method of choice for obtaining dynamic structure information at the level of single molecules. To do so, organic dye molecules are attached to specific sites of the biomolecule and based on their dipole–dipole coupling and the resulting energy transfer efficiency, the distance, and, therefore, also the molecular conformation can be reconstructed.
In this project, we aim towards a similar method based on quantum metrology measurements, using nitrogen vacancy (NV) centres in diamond as sensors for dipolar interactions of molecular spin labels. The main advantage of this approach is based on the NV as stable sensor and the actual size of the spin labels, being much smaller than the organic dye molecules used in FRET.
For the establishment of the NV centre as sensor for electron spin dipolar interactions, we use double electron-electron resonance (DEER) measurements as a known tool in electron paramagnetic resonance (EPR) experiments. Yet, the AXY sequence, another method developed from dynamical decoupling measurements is employed aswell. It is applied in order to be able to gather more information about the detected systems by the detection of individual frequencies, resolving the individual couplings of the interacting electron spins. At this point, this thesis analyses the various approaches and requirements for the sensing measurements necessary for these detection methods.
A major difficulty of this approach got evident during the evaluation of the gathered data. For the reconstruction of the DEER measurement results with a unknown depth of the used NV centre, the information about the applied magnetic field was insufficient. Thereupon, we addressed this issue of the insufficient information with the development of a novel magnetic field reconstruction, obtaining all measurable parameters for a precise determination of the three-dimensional magnetic field orientation. Additionally, a benchmark study of this method proofs its reliability and consistency for magnetic field variations.
The final part of this thesis combines the gathered information of the dipolar coupling parameters measured with the help of NVs into a simulation for the reconstruction of the distance between coupled electron spins. Since the actual measurement of all quantities is still challenging, an artificial system of two interacting electron spins is used for the validation of this simulation.

Contents

1 Introduction

Understanding living organisms starts by the mere investigation of macro-organisms, observable by the unaided human eye, continues on a smaller scale with micro-organisms, only visible with the help of instruments, and – nowadays – concludes in observations on the nano-meter scale: the world of molecules and atoms. Yet, any scale reduction of the observables, as for example the distance of participating molecules in biological processes, requires more complex measurement or analysis techniques. These obstacles are introduced by the errors and deviations from the sample preparation, movement, and the sheer amount of samples necessary to allow a processing in the first place. Well-known examples for such techniques are the **X-Ray Crystallography** (XRC) and the **Cryogenic Electron Microscopy** (cryo EM), both observing the entire three-dimensional structure of crystals and molecules with a sub-atomic resolution[1,2], or the **Förster Resonance Energy Transfer** (FRET), reconstructing relative positions on molecules and molecular complexes[3] together with their variation during cellular processes on a nano-meter scale.

These techniques are limited by constraints, which measurements on such small scales can bring forth. For instance, possible deviations from the natural structure can be introduced by the necessary sample preparation process for measurements based on XRC and cryo EM techniques. Here, the inherent crystallisation or rapid freezing can generate artificial environments or trap the molecules in specific states.[4,5] Additionally, this trapping of the molecule state can prohibit the observation of dynamic processes. However, such impacts on natural occurrence and structure are not intended and, therefore, have to be addressed.

The FRET technique therefore takes a different approach at observation and preparation. It does not intend to observe the entire macro-molecule at the same time, but only specific sites, and can thus omit strongly impacting preparations. It thereby enables the real-time distance measurement between molecular sites in vitro and in vivo[6] on a single molecule level.[7–11]

In order to measure FRET and reconstruct relative positions between molecular complexes, fluorophores are flexibly linked to single sites on the biomolecules of interest.[12] However, the created antennas on the sites, consisting of the linkers in combination with the fluorophores, introduce a measurement uncertainty with their relative positioning, orientation and rotation, as well as dynamics. Altogether, the size of these antennas influence the dipole-dipole interaction of the linked fluorophores and, thus, the measured energy transfer efficiency used in the calculation of their relative distance.

Trying to overcome these uncertainties, most approaches assume a time-wise averaging or time-regime partitioning, ultimately reconstructing the entire build-up of the molecular complexes through simulations.[13,14]

In recent developments, dipole-dipole interaction experiments similar to FRET measurements are performed by exchanging the interacting fluorophores with coupled electron spins.[15] Prominent examples of such electron spin labels are various nitroxide spin-based structures, strictly smaller in size than common fluorophores. This exchange reduces the accessible volume of the antenna and its associated degrees of freedom and, consequently decreases the uncertainty introduced by these parameters. The distance between the labels may then be measured by observing the interaction strength of coupled electron spin labels.
However, measuring electron spin interactions using **Electron Paramagnetic Resonance** (EPR) experiments proves difficult as well. Due to the utilised sensor and comparably weak signal strengths in these measurements, it is necessary to detect a large amount of interacting pairs at the same time, leading to a statistical averaging of individually contributing conformations. An approach to overcome this downside relies on the variation of the detection method, allowing the detection of double-electron resonances on a single molecule level regardless of the almost negligible amount of energy transferred in this process.
Recent experiments showed the possibility to determine the positions of single electron spins performing EPR measurements by using **Nitrogen Vacancy** (NV) centres in diamond as sufficiently sensitive sensors. Two striking experiments hereof are the reconstruction of electron spin positions on a diamond surface, performed by Sushkov et al.[16], and the detection of a single spin-labelled biomolecule by Shi et al.[17]. These model examples are based on the favourable properties of NV centres in diamond as magnetic resonance sensors for quantum metrology experiments. This is mainly founded on the outstanding features of NVs, such as the possibility to coherently manipulate and readout their quantum states with an exceedingly long lifetime even at ambient conditions.[18–20]

In order to establish a general overview on this work's achieved development towards NV based EPR measurements of electron-spin labelled complexes, this thesis is divided into three partitions: First and foremost, the beginning chapters are dedicated to the experimental theory and relevant fundamentals around NV centres in diamond. In this regard, the theory of in this work employed measurement sequences and their general interpretations are introduced as well.
Subsequently, the following chapters discuss the performed magnetic resonance experiments with their particular interpretation, the consequently arising open question about the absolute magnetic field vector orientation, and the development of a new measurement routine as a possible solution.
Concluding the experimental part, this work presents a model system, allowing to reconstruct the distance of coupled electron spins with the help of NV-based EPR measurements, as performed in the previous chapters.

2 Physical Fundamentals for NV-based Sensing

As a key requirement for EPR measurements on a single spin sensor basis, it is essential to understand the fundamentals of all involved building blocks individually, as well as their interconnection in the experiment. Therefore and as an introduction to the experiments, this chapter gives a detailed overview of the NV centre, which serves as the quantum sensor in the experiments discussed in this work. More precisely, presented are the basic properties of the NV centre, its environment, and its interplay with external fields, as for example magnetic fields or proximal nuclear and electron spins.
To offer a pictorial representation of the employed spin manipulations, the **Bloch sphere representation** provides a powerful tool, visualising the performed spin state changes.

However, before proceeding to the dynamics of the NV centre, the following section deals with NV impurities in diamond lattices and their physical properties, such as the electronic structure and optical accessibility. These properties motivate the sole use of NV centres in diamond as quantum sensors for the performed experiments.

2.1 Diamonds - Properties and Manufacturing

Diamonds are not only known for their elegance as jewellery, but also their outstanding physical properties, which are almost all exceptionally pronounced when compared to other naturally occurring materials. The most often mentioned properties are the high thermal conductivity, extreme hardness, and electronic characteristics[21]. Additionally, diamonds have remarkable optical features. For instance, the high refractive index of $n = 2.42$ and its resulting transparency for all wavelengths of visible light. Those characteristics altogether make diamonds of great use and variability in nowadays scientific and engineering applications.

2.1.1 Atomic Structure of Diamond

In the work with diamonds as environment for quantum sensing, it is important to discuss the underlying lattice structure. With this, also its atom composition and basic effects arising due to different occupants on the lattice sites are crucial.

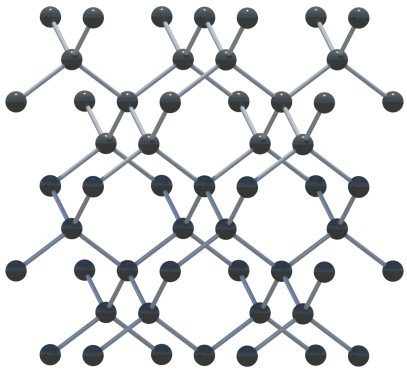

Figure 2.1: Face centred cubic lattice structure of diamond with covalent bonds. Each carbon atom is connected to its four nearest neighbours, spanning a tetrahedron. The inter atomic distance is 1.54 Å with a lattice constant of $a_0 = 3.57$ Å.

Condensed Matter Topology

The physical properties of diamonds at ambient temperature are determined by its **face-centred cubic** (fcc) structure. The pure atomic structure consists of carbon atoms in sp^3 hybridisation exclusively, where each atom itself is bound to its four nearest neighbours with an inter-atomic distance of 1.54 Å.

Due to the tetrahedral conformation of the atoms with a bonding angle of 109.47°, the lattice constant is followingly given as $a_0 = 3.57$ Å. Its cubic unit cell consists of eight whole atoms, composed by the partial eight corner atoms ($\frac{1}{8} \cdot 8$), the three partial face centred atoms ($\frac{1}{2} \cdot 6$), and the four inner atoms. Thus, the two-atomic *Bravais lattice* basis is determined by their respective origins in $(0, 0, 0)$ and $(\frac{1}{4}, \frac{1}{4}, \frac{1}{4})$.

Atomic Composition

There exist two naturally occurring stable isotopes of carbon, which can both be found in diamond. Firstly and more common, there is the ^{12}C isotope with a natural abundance of 98.9 %[22]. Since this isotope consists of each six protons and neutrons, it has no free nuclear spin or charge. In contrast, the second stable isotope ^{13}C possesses one additional neutron, resulting in a non-zero nuclear spin quantum number $I_n = \frac{1}{2}$. The natural abundance of ^{13}C is given by only 1.1 %[22], but in terms of mean distance between atom sites in the diamond lattice, this leads to roughly 10 lattice sites between two adjacent ^{13}C atoms.
While a diamond lattice theoretically consists of a strict, equidistant repetition of atoms, there have been many defects observed. A typical defect is the substitution of a carbon atom with an atom of a different element. There have already been more than 80 other elements forming impurities detected in the crystal lattice of diamond, whereas nitrogen, boron, oxygen, and hydrogen are the most prominent of those[22]. Since boron (atomic number 5) and nitrogen (atomic number 7) atoms are roughly of the same size and mass as carbon, they are the most likely to be substituted into the diamond lattice[23]. This incorporation is dependent on the growth conditions, hence for natural diamond, the composition can vary drastically, although for industrially produced diamonds, those values can be controlled quite accurately.
Comparable to carbon, natural nitrogen also occurs in two stable isotopes with one additional proton and neutron each. The vast majority of nitrogen occurs as ^{14}N with a natural abundance of 99.6 %, while ^{15}N makes up only 0.4 %. For ^{14}N, each of the seven protons and neutrons contribute a nuclear spin of $\pm\frac{1}{2}$, giving the nucleus a total magnetic spin number $I_n = 1$. As a result of the additional neutron in ^{15}N, this leads to a total spin quantum number $I_n = \frac{1}{2}$.

Classification

Due to nitrogen impurities, diamonds can be classified into two different categories, **Type I** with a high nitrogen content and **Type II** with a lower nitrogen content[23]. Going even further, in 1965, Dyer et al.[24] subdivided those types into four more specific groups:

- **Type Ia:** high nitrogen content with *platelets* of nitrogen ($500 - 3000$ ppm),
- **Type Ib:** high nitrogen content with nitrogen as single substitutional atoms (< 100 ppm),
- **Type IIa:** very low nitrogen content (< 1 ppm), or
- **Type IIb:** very low nitrogen content (< 1 ppm) with boron impurities.

Resulting from the amount and type of impurities incorporated into the diamond lattice, the crystal can appear in different colours, giving those crystal impurities also the name **colour centres**.

2.1.2 Production of Artificial Diamonds

Naturally grown diamonds, as used for the manufacturing of jewellery, are very rare, making them an expensive resource. In addition, the high amount and variety of impurities in natural diamond make them unfit for scientific and industrial purposes.
Hence, the development of techniques to produce artificial diamonds was an industrially driven priority from the 1950's on[25] and lead to the possibility to engineer artificial diamonds with a high purity since the early 1980's[26]. Nowadays, there exist two different prominent production approaches. Both rely on a seed, where the diamond is grown onto.

HPHT

The first production approach involves **High-Pressure High Temperature** (HPHT) techniques, mimicking the conditions of natural diamond growth with pressures up to 10 GPa and temperatures of at least 1400 °C. For those techniques, the seed diamond is placed together with a high purity carbon source and a metal alloy solvent in a press system. In this system, the metal is melted due to the high temperatures. Then, the carbon gets dissolved and diffuses through the metal solvent until it ultimately precipitates onto the seed. While graphite is the more stable allotrope of carbon atoms, the high pressure of this process shifts the reaction equilibrium to the creation of a diamond structure. After the pressure is released, the grown structure inherits the crystal structure of the diamond seed[27].

CVD

The second approach is based on **Chemical Vapour Deposition** (CVD) and can be categorised into normal CVD and enhanced CVD. For both techniques, the diamond is also grown onto a seed, though with a much lower pressure compared to the HPHT production. The main difference of the two CVD techniques is the required seed, which has to be a diamond for common CVD, whereas due to the development of thermal- and plasma-enhanced CVD, a non-diamond seed can be used in enhanced CVD. For all CVD methods, the temperature during the diamond growth is much lower, being between 500 °C – 1200 °C, and an activated carbon source (e.g. methane) leads to the sedimentation of carbon atoms onto the seed substrate. Yet, since the pressure is lower than for HPHT, not only carbon-containing feed-gas, but also atomic hydrogen is needed in the gas mixture to ensure the growth of diamond instead of graphite. The atomic hydrogen selectively etches off the double bonds created in the formation of graphite. Hence, only the diamond structure is allowed to expand. The growth rate of this process is dependent on the transport efficiency of the reactant species to the seed[28].
Those techniques are much more expensive than HPHT, but allow to produce high-purity diamonds with only few embedded impurities. For those techniques, the amount of crystal impurities is dependent on the quality of the feed-gas and condition of the growth chamber. Going even one step further, it is also possible to achieve isotopically pure diamond layers consisting of almost pure ^{12}C, as used for one diamond sample employed in this work (Sec. 5.1.1), or ^{13}C respectively.[29]

2.2 Nitrogen Vacancy Centres in Diamond

As already mentioned, the crystal structure of real diamond, even if fabricated industrially, is not perfect. However, if impurities are implanted deliberately, they offer a lot of potential for today's research. The most mentioned impurities for quantum sensing applications are the nitrogen, the silicon, and the germanium vacancy defects. Nevertheless, due to the remarkable usability even at room temperature, this work exclusively relies on the NV centre. Therefore, it is the only defect taken into further consideration from now on.

2.2.1 Creation of Nitrogen Vacancy Centres

For the creation of NV centres, a nitrogen atom in combination with a vacancy in the diamond lattice are required. Here, a vacancy is an unoccupied site in the crystal lattice. Those vacant sites are able to diffuse through the diamond lattice at temperatures of around 600 °C[30]. This process of annealing is usually driven between 400 °C – 1000 °C[31] and after binding to a nitrogen atom, the combination stays stable up to more than 1400 °C[30]. Due to the almost uniform distribution of nitrogen atoms in type I diamonds, this would lead to an equally uniform distribution of NV centres in the sample.

One possible method for NV creation is focusing a nitrogen ion beam onto the diamond surface[31,32]. It leads to the implantation of nitrogen atoms and the removal of extra carbon atoms from the lattice. The amount of implanted defects is hereby dependent on the implantation dose and the depth depends on the acceleration energy applied to the ion beam (discussed for the employed samples in Sec. 5.1.1). Therefore, if a type II substrate with a very low amount of intrinsic nitrogen is used, distinct areas (shape and depth) of NVs can be implanted.

Another method is the contamination of the feed-gas during the growth process (described in Sec. 2.1.2) with nitrogen. In this realisation, confined layers containing NVs can be grown onto diamond substrates. Here, the amount of defects is dependent on the gas composition and the depth can be controlled by the layer height and the subsequent uncontaminated overgrowth with pure carbon.

2.2.2 Properties of the Nitrogen Vacancy Centre

When speaking about the NV centre as a quantum sensor, it is essential to understand the underlying features, as the lattice structure and the thus resulting electronic structure which determindes the optical addressability.

Lattice Incorporation

The NV centre is a point defect in diamond, replacing two adjacent carbon atoms by one nitrogen atom and a vacant site, the *vacancy*. This incorporation into the diamond lattice, leads to eight possible orientations of the NV principal axis, connecting the nitrogen atom with the vacancy, along the four crystallographic axes: $[\bar{1}\bar{1}1]$, $[1\bar{1}\bar{1}]$, $[111]$, and $[\bar{1}1\bar{1}]$. A measurement technique for the determination of directionality is described in Doherty et al.[33].
In this thesis, all used properties of the NV centre are invariant to sequence changes of the nitrogen and vacancy, for what reason their order can be ignored. Thus, only four orientations remain, depicted in Fig. 2.2.
The NV centre's neighbouring atoms are three carbon atoms on both sides, which creates an overall tetrahedral structure.
Due to this structure, the NV centre belongs to the symmetry group designated by C_{3v}. This group is characterised by a three-fold axis symmetry and an additional three-vertical-plane symmetry. The axis symmetry is given by rotations of 120° around the principal axis and the three vertical planes are spanned by the NV axis with the connecting carbon atoms.

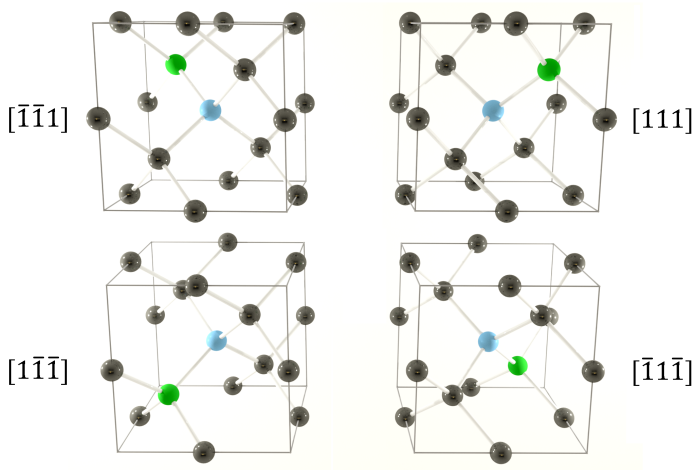

Figure 2.2: The four possible orientations of the NV centre in diamond (nitrogen green; vacancy blue). Due to symmetry, the principal axis connecting the nitrogen atom and the vacancy can be along the four crystallographic axes $[\bar{1}\bar{1}1]$, $[1\bar{1}\bar{1}]$, $[111]$, and $[\bar{1}1\bar{1}]$.

Electronic Structure

NV centres can exist in two stable charge states, the neutral NV^0 and the negatively charged NV^-. Those two states can be inter-converted by photo-induced ionisation with blue or red laser light.[34]
The NV^0 electron configuration has five electrons in total: three obtained by the dangling carbon bonds and two from the dangling nitrogen bond. Out of those five electrons, four combine to pairs with sp^3-like orbitals and the fifth electron remains free. This odd number of electrons leads to an effective spin singlet state with spin angular momentum $S = \frac{1}{2}$. Contrary, the negatively

charged NV^- has an even number of electrons, carrying an integer spin angular momentum of $S = 1$.[18] The additional sixth electron is acquired from an arbitrary donor in the diamond lattice, for example another substitutional nitrogen atom (shown in Fig. 2.3), leading to spin triplet states for the NV^- .

Since all measurements described in this thesis are exclusively performed with specimen of the NV^- , the minus sign will be omitted and the name 'NV' will be used synonymously.

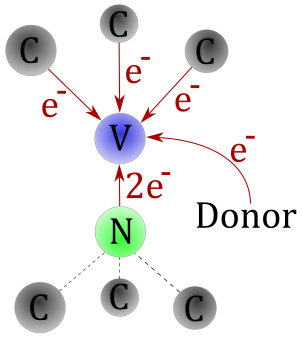

Figure 2.3: A schematic of the NV electronic structure for the negatively charged NV^- . In total, five electrons are provided by the surrounding atoms and one additional by a donor in the lattice.

Due to the integer spin number of the NV centre, the ground and excited states are triplets, with the $m_s = \pm 1$ states being degenerate. This leaves the third state, the $m_s = 0$ state, with no magnetic moment. The resulting level scheme is displayed in Fig. 2.4.

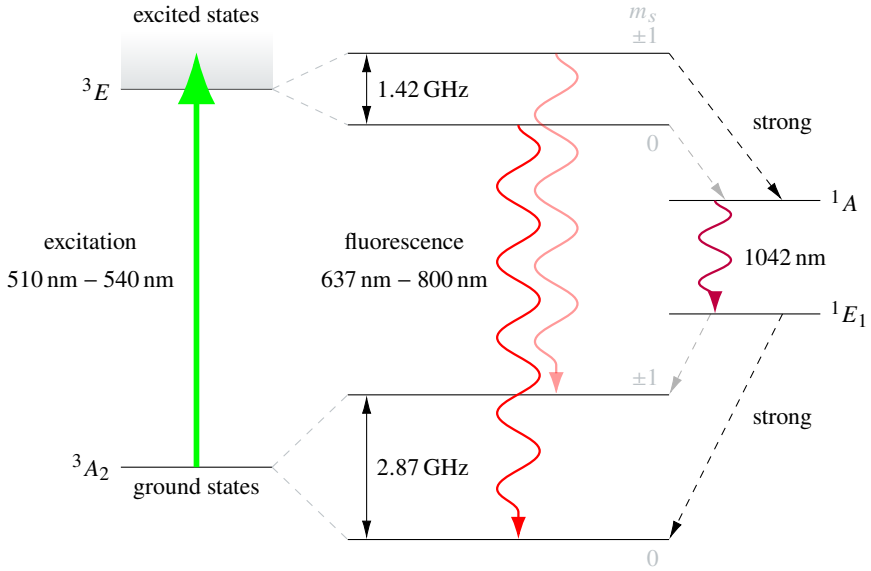

Figure 2.4: The energy structure of a NV with the triplet ground and excited states, both degenerate due to their electronic spin state. The decay path over the metastable intermediate singlet states connects the $m_s = \pm 1$ excited states with the $m_s = 0$ ground state strongly (according to McGuinness[35]).

Besides the ${}^3A_2$ ground state $|g\rangle$ and ${}^3E$ excited state $|e\rangle$, there exist the singlet intermediate states ${}^1A_1$ and ${}^1E_1$. Yet, since there is neither a connection expected between the ${}^1E_1$ singlet state to the ${}^3E$ state, nor from the ${}^1A$ state to the ${}^3A_2$ state, those two intermediate states can be combined into an effective state $|ds\rangle$.[36]
Regarding the energy differences of the given states, the spin-spin interaction of the two unpaired electrons introduces a splitting of the $m_s = 0$ and $m_s = \pm 1$ ground states. This **Zero-Field Splitting** (ZFS) separates the two states by $D = 2.87\,\mathrm{GHz}$[37] and is present even without any additional field. For the excited state, this effect results in a ZFS of $D = 1.42\,\mathrm{GHz}$[38].
The typical lifetimes of the excited states are 12 ns for the $|e, m_s = 0\rangle$ state, 7.8 ns for the $|e, m_s = \pm 1\rangle$ states,[39] and on the order of 370 ns for the effective state $|ds\rangle$[36].

Optical Addressability

One of the most crucial properties of the NV centre, leading to its great impact on many quantum applications, is its optical addressability. It not only allows to initialise the system into a defined state, but also enables the optical readout of the actual spin state.
For the initialisation, an off-resonant green laser with a wavelength of $\lambda = 510\,\mathrm{nm} - 540\,\mathrm{nm}$[34] is applied to the NV centre, exciting the system into the $|e\rangle$ states. After this excitation, there are two different decay paths back to the ground state:

- The direct decay and
- the indirect decay via the intermediate singlet states.

The first decay path is spin-conserving and leads to the emission of a red photon with a wavelength of $\lambda = 637\,\mathrm{nm} - 800\,\mathrm{nm}$.
The second decay path is partially non-radiative and connects to the metastable singlet states $|ds\rangle$, where the inter-singlet decay is expressed via the emission of infra-red light ($\lambda = 1042\,\mathrm{nm}$)[40].
The probability of this *inter-system crossing* is state-dependent. On the one hand, the coupling of the $|e, m_s = \pm 1\rangle \rightarrow |ds\rangle$ transition is strong, compared to the second excited state coupling of the $|e, m_s = 0\rangle \rightarrow |ds\rangle$ transition. On the other hand, the coupling of the $|ds\rangle \rightarrow |g, m_s = \pm 1\rangle$ transition is weaker than the $|ds\rangle \rightarrow |g, m_s = 0\rangle$ ground state coupling. The combination of those effects lead to a population conversion into the $|g, m_s = 0\rangle$ state and also to a reduction of the fluorescence signal by approximately 30 %. This second decay path is more likely to happen if the initial state was one of the $|g, m_s = \pm 1\rangle$ states. Therefore, those states are called dark states.

In conclusion, the optical excitation has two significant meanings for this work: it allows the optical initialisation in the $m_s = 0$ ground state by application of green laser light. Additionally, this optical excitation enables the optical readout of the initial NV state by detection of the fluorescence signal.[20]

2.3 Spins and Spin Dynamics

For electrons and nuclei, spin is an intrinsic form of angular momentum resulting from a magnetic dipole moment $\boldsymbol{\mu}$. The mathematical treatment in a magnetic field and the coupling between two similar spins is identical, yet, the magnetic moment of nuclear spins is much smaller than that of electron spins. Therefore, different properties and interactions are relevant for the performed measurements for both species.
For the description of a spin in a magnetic field $\boldsymbol{B}$ it is practical to start with the classical picture of a magnetic moment in the magnetic field. Hence, the energy is given as

$$E = -\boldsymbol{\mu} \cdot \boldsymbol{B}. \tag{2.1}$$

The spin magnetic moment can be calculated by its charge q, mass m, and spin angular momentum $\boldsymbol{S}$ via

$$\boldsymbol{\mu} = g\frac{q}{2m}\boldsymbol{S}, \tag{2.2}$$

with the dimensionless g-factor g, which is dependent on the particle type (values given in Tab. 2.1) and the spin angular momentum $\boldsymbol{S} = \frac{\hbar}{2}\boldsymbol{\sigma}$ defined by the *Pauli matrices*.

Table 2.1: Electron and nuclear spin g factors.[41]

Particle type	g-factor
electron	−2.00232
proton	5.586
neutron	−3.8261

Assuming an alignment of the magnetic field with the quantisation axis z and the magnetic field amplitude B_0, Eq. 2.1 rewrites as

$$E = -\mu_z B_0. \tag{2.3}$$

Now, with the quantisation of the spin eigenvalues for a spin-$\frac{1}{2}$ particle, the magnitude of the spin angular momentum along the z-axis is given by $\pm\frac{\hbar}{2}$ (see Fig. 2.5):

$$E = \pm\frac{\hbar}{2}\widetilde{\gamma}_i B_0, \tag{2.4}$$

where the reduced gyromagnetic ratio is defined dependent on the particle type i via

$$\widetilde{\gamma}_i = \frac{\gamma_i}{2\pi} = \frac{g_i \mu_i}{2\pi}. \tag{2.5}$$

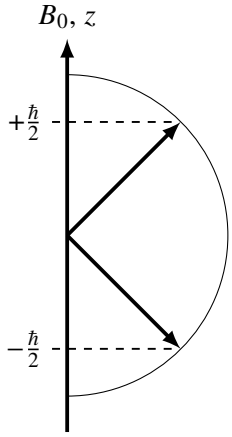

Figure 2.5: Allowed spin angular momentum values for the z projection of a spin-$\frac{1}{2}$ particle leads to a half integer magnitude of $\pm\frac{1}{2}$.

2.3.1 Larmor Precession of Spins

As shown in Fig. 2.6, the tilt between the magnetic field $\boldsymbol{B}$ and the magnetic moment of the spin leads to a torque, resulting in a precession of the spin around the magnetic field direction.

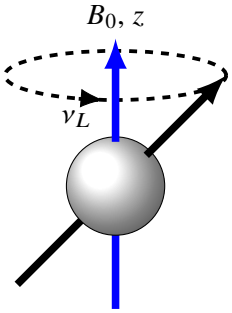

Figure 2.6: In a semi-classical picture, a magnetic moment exposed to a magnetic field precesses around the magnetic field direction with its specific Larmor frequency ν_L. The sign of the gyromagnetic ratio of the spin determines the rotation direction of the precession and the frequency is proportional to the magnetic field strength.

This *Larmor frequency* of the spin can be calculated using the time derivative of the angular momentum

$$\frac{\mathrm{d}\boldsymbol{\mu}}{\mathrm{d}t} = \gamma\boldsymbol{\mu} \times \boldsymbol{B}. \tag{2.6}$$

For a magnetic field $\boldsymbol{B} = (0, 0, B_0)^T$ aligned along z, the Larmor frequency is

$$\nu_L = \frac{\omega_L}{2\pi} = \widetilde{\gamma} B_0. \tag{2.7}$$

The sign of the gyromagnetic ration determines the rotation direction of the Larmor precession and the frequency is directly proportional to the strength of the magnetic field.

2.3.2 Dipole-Dipole Interaction Hamiltonian

Since spins carrying a magnetic moment $\boldsymbol{\mu}$ are not only influenced by the magnetic field, but also by other spins in close proximity, the *dipolar coupling* which leads to the *interaction* has to be discussed. Those dipolar interactions arise due to the magnetostatic field, created by a magnetic dipole $\boldsymbol{\mu}_i$ of spin i which in turn affects the magnetic dipole $\boldsymbol{\mu}_j$ of spin j. The distance $\boldsymbol{r}_{ij}$ of those spins is given by their individual positions $\boldsymbol{r}_i$ and $\boldsymbol{r}_j$, shown in Fig. 2.7.

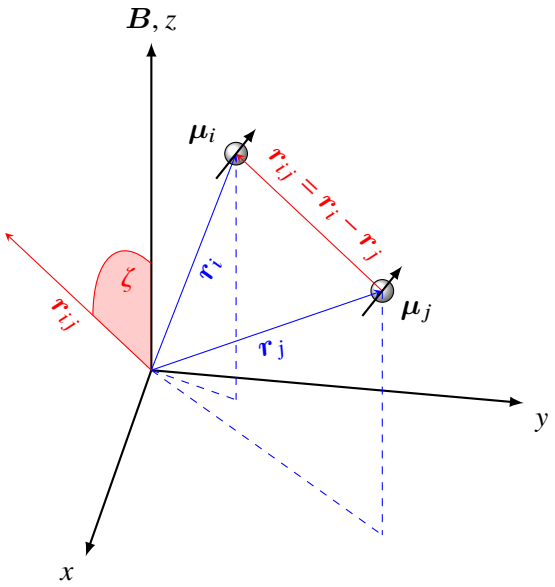

Figure 2.7: Schematic 3d-illustration of two coupled magnetic moments $\boldsymbol{\mu}_\mathrm{i}$ and $\boldsymbol{\mu}_\mathrm{j}$. The distance between the spins is given by $\boldsymbol{r}_{ij} = \boldsymbol{r}_i - \boldsymbol{r}_j$. The angle ζ between the z-direction and the connection vector $\boldsymbol{r}_{ij}$ holds true for the magnetic field alignment along z with $\boldsymbol{B} = (0, 0, B_0)^T$.

For two dipoles in close proximity, the potential energy reads as

$$E = \frac{\boldsymbol{\mu}_1 \cdot \boldsymbol{\mu}_2}{\boldsymbol{r}_{12}^3} - \frac{3\,(\boldsymbol{\mu}_1 \cdot \boldsymbol{r}_{12})\,(\boldsymbol{\mu}_2 \cdot \boldsymbol{r}_{12})}{\boldsymbol{r}_{12}^5}. \tag{2.8}$$

This equation can now be used to infer a general dipolar contribution to the N-spin-coupling Hamiltonian by the superposition principle:

$$\mathcal{H}_\mathrm{dip} = \sum_{\substack{i,j \\ i \neq j}} \frac{\boldsymbol{\mu}_i \cdot \boldsymbol{\mu}_j}{\boldsymbol{r}_{ij}^3} - \frac{3\,(\boldsymbol{\mu}_i \cdot \boldsymbol{r}_{ij})\,(\boldsymbol{\mu}_j \cdot \boldsymbol{r}_{ij})}{\boldsymbol{r}_{ij}^5}. \tag{2.9}$$

Considering the dipole moment $\boldsymbol{\mu}_i = \gamma_i \hbar \boldsymbol{S}_i$, Eq. 2.9 can be rewritten in terms of magnetic moment vector $\boldsymbol{S}_i$ as

$$\mathcal{H}_\mathrm{dip} = \sum_{\substack{i,j \\ i \neq j}} \frac{\mu_0 \gamma_i \gamma_j \hbar}{4\pi \left|\boldsymbol{r}_{ij}\right|^3} \left[\boldsymbol{S}_i \boldsymbol{S}_j - \frac{3}{\left|\boldsymbol{r}_{ij}\right|^2} (\boldsymbol{S}_i \cdot \boldsymbol{r}_{ij})\,(\boldsymbol{S}_j \cdot \boldsymbol{r}_{ij}) \right], \tag{2.10}$$

with the vacuum magnetic permeability μ_0. For strong magnetic fields $\boldsymbol{B} = (0, 0, B_0)$, this Hamiltonian can be rewritten as

$$\mathcal{H}_{\text{dip}} = \frac{1}{2} \sum_{\substack{i,j \\ i \neq j}} d_{ij} \left(1 - 3\cos^2 \zeta_{ij}\right) \left[3S_i^z S_j^z - \boldsymbol{S}_i \cdot \boldsymbol{S}_j\right], \tag{2.11}$$

with the dipolar coupling $d_{ij} = \frac{\mu_0 \gamma_i \gamma_j \hbar}{4\pi |\boldsymbol{r}_{ij}|^3}$ and the angle θ_{ij} between the connection vector $\boldsymbol{r}_{ij}$ and the magnetic field vector $\boldsymbol{B}$. Using the common ladder operator definitions $S^+ = S^x + iS^y$ and $S^- = S^x - iS^y$, the Hamiltonian can be reduced further to

$$\mathcal{H}_{\text{dip}} = \frac{1}{2} \sum_{\substack{i,j \\ i \neq j}} d_{ij} \left(1 - 3\cos^2 \zeta_{ij}\right) \left[2S_i^z S_j^z - \frac{1}{2}\left(S_i^+ S_j^- + S_i^- S_j^+\right)\right], \tag{2.12}$$

with the transverse coupling part dependent on $S_i^{\pm}$ and the parallel coupling part dependent on S_i^z.

In Eq. 2.12, the angle dependent contribution $\left(1 - 3\cos^2 \zeta_{ij}\right)$ vanishes for all connection angles $\zeta_{ij} = 54.74°$ between spins i and j. This *magic angle* and the resulting phenomena are well exploited in many different applications of nowadays magnetic resonance measurements[42].

Electron Spins

From Eq. 2.2, the definition of the magnetic moment of an electron, or also called *Bohr magneton*, follows as

$$\mu_B = \frac{e\hbar}{2m_e} = 9.2740 \times 10^{-24} \frac{\text{J}}{\text{T}}, \tag{2.13}$$

with the electron mass m_e, the elementary charge e, and the reduced Planck constant $\hbar$. The electron spin operator is from here on denoted as $\boldsymbol{S} = \left(S_x, S_y, S_z\right)^T$.

The energy splitting of a single unpaired electron with spin quantum number $\pm\frac{1}{2}$ and the two energy levels $E_{\pm} = \pm\frac{1}{2} g_e \mu_B B_0$ is given as

$$\Delta E = g_e \mu_b B_0, \tag{2.14}$$

and shown in Fig. 2.8. The corresponding transition frequency is calculated via $\omega = \frac{\Delta E}{\hbar}$.
For two strongly coupled electron spins, the two levels $|\uparrow\uparrow\rangle$ and $|\downarrow\downarrow\rangle$ are energy-wise well separated, and do not contribute to the transition frequency sensed by the NV centre. Therefore, the dipolar interaction for two coupled electron spins described by Eq. 2.12 becomes

$$\mathcal{H}_{e^-e^-} = -\frac{1}{2} d_{ij} \left(1 - 3\cos^2 \zeta_{ij}\right) \widetilde{S}_x, \tag{2.15}$$

with the transition spin operator $\widetilde{S}_x = \frac{1}{2}\left(|\uparrow\downarrow\rangle \langle\downarrow\uparrow| + \text{h.c.}\right)$.

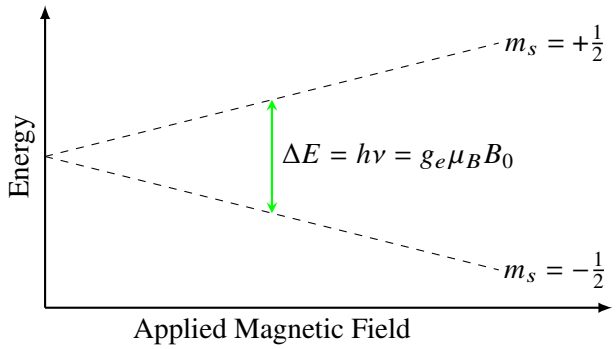

Figure 2.8: Energy levels of a single unpaired electron spin in a static magnetic field $\boldsymbol{B}$, with amplitude B_0. The magnetic field is aligned along the electron spin quantisation axis. In green, the energy difference ΔE depicts the transition frequency of the two spin states $+\frac{1}{2}$ and $-\frac{1}{2}$.

Nuclear Spins

As for the Bohr magneton, Eq. 2.2 defines the nuclear magneton similar as

$$\mu_N = \frac{e\hbar}{2m_p} = 5.0508 \times 10^{-27} \frac{\mathrm{J}}{\mathrm{T}}, \tag{2.16}$$

with the only difference of using the proton mass m_p instead. The nuclear spin operator is from here on denoted as $\boldsymbol{I} = \left(I_x, I_y, I_z\right)^T$.

For resonance measurements performed at a few hundred Gauss, the detected Larmor frequencies of nuclear spins are between 50 kHz – 10 000 kHz. Values for typical nuclear spin species and the corresponding Larmor frequencies at a commonly measured magnetic field amplitude are given in Tab. 2.2.

Table 2.2: Exemplary nuclear Larmor frequencies, commonly sensed by NV centres in diamond at $B_0 = 250\,\mathrm{G}$.

Nucleus type	$\widetilde{\gamma}$ in $\frac{\mathrm{kHz}}{\mathrm{G}}$	$\lvert\nu_L\rvert$ in kHz
^{1}H	4.257747892	1064.4
^{13}C	1.0708	267.7
^{14}N	0.3077	76.9
^{15}N	−0.4316	107.9
^{19}F	4.0052	1001.3

Since electron spins also precess in a magnetic field, a way to differ between the response to the magnetic field of both types is necessary. By calculating the ratio of Eq. 2.13 and Eq. 2.16, the mass ratios of both particles determines the relative strength of the interactions which are

roughly three orders of magnitude smaller for nuclear spins. Therefore, the Larmor frequency of electron spins for weak magnetic fields of 100 G − 500 G is already quite large (in the order of MHz) compared to the Larmor frequencies of nuclear spins.

2.3.3 The Bloch Sphere Representation

In the Bloch sphere representation the north and south poles of a sphere are assigned to the basis vectors of a two-level system, namely $|\uparrow\rangle$ and $|\downarrow\rangle$. Hence, each point on this sphere corresponds to one particular superposition state $|\Psi\rangle = \alpha\,|\uparrow\rangle + \beta\,|\downarrow\rangle$, depicted in Fig. 2.9. Using the probability normalisation $|\alpha|^2 + |\beta|^2 = 1$ allows to determine the pre-factors α and β by two spherical angles θ and ϕ:

$$\alpha = \cos\left(\frac{\theta}{2}\right), \tag{2.17}$$

$$\beta = \sin\left(\frac{\theta}{2}\right) e^{i\phi}. \tag{2.18}$$

Here, the system is assumed to be a pure state, leading to a radius equal to 1. The angle intervals are given as $\phi \in [0, 2\pi)$ and $\theta \in [0, \pi)$, whereas the complex phase $e^{i\phi}$ in Eq. 2.18 has no impact on the expectation value $|\beta|^2$.

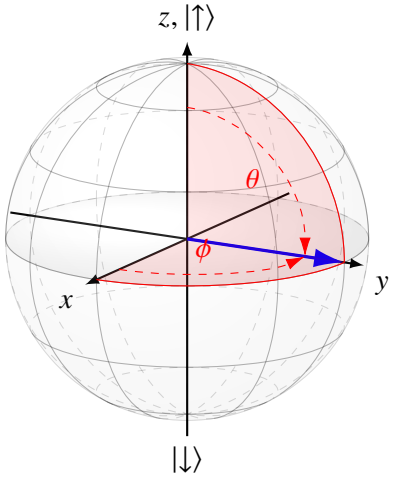

Figure 2.9: Bloch sphere representation for a superposition state $|\Psi\rangle$. The state is depicted as a vector pointing into the direction of a single point on the unit sphere and can be described using the two corresponding angles θ and ϕ.

Following the Bloch representation, the Bloch vector $\boldsymbol{R}$ for an arbitrary pure state $|\Psi\rangle$ is the expectation value of the Pauli spin matrices $\boldsymbol{\sigma} = (\sigma_x, \sigma_y, \sigma_z)^T$:

$$\boldsymbol{R} = \langle \boldsymbol{\sigma} \rangle = \langle \Psi | \, \boldsymbol{\sigma} \, | \Psi \rangle = \begin{pmatrix} \sin\theta\cos\phi \\ \sin\theta\sin\phi \\ \cos\theta \end{pmatrix}. \tag{2.19}$$

2.4 NV Spin Hamiltonian

The NV spin Hamiltonian describes the different interactions of a NV with its environment, static magnetic fields, different type of spin-spin interactions, and **microwave** (MW) fields present in the system. Due to the in this work performed spin state manipulations, *quantum gates* or just *gates*, the total Hamiltonian is split into two parts: the time-independent system Hamiltonian $\mathcal{H}_0$ and the time-dependent interaction Hamiltonian $\mathcal{H}_{\text{int}} = \mathcal{H}_{\text{int}}(t)$. Accordingly, the system Hamiltonian is

$$\mathcal{H} = \mathcal{H}_0 + \mathcal{H}_{\text{int}}. \tag{2.20}$$

2.4.1 Static System Hamiltonian

The main influence on the time-independent system Hamiltonian comes from the inter-electron interaction $\mathcal{H}_{\text{ZFS}}$, the electron spin Zeeman interaction $\mathcal{H}_{\text{B}}$, the hyperfine interaction $\mathcal{H}_{\text{HF}}$ of the NV electron spin with nuclear spins, and the dipolar coupling $\mathcal{H}_{\text{Dip}}$ of the NV electron spin to other proximal electron spins:

$$\mathcal{H}_0 = \mathcal{H}_{\text{ZFS}} + \mathcal{H}_{\text{B}} + \mathcal{H}_{\text{HF}} + \mathcal{H}_{\text{Dip}}. \tag{2.21}$$

As described in Sec. 2.2.2, the NV is assumed to be a triplet system where the basis is chosen such that the spin quantisation is along the z-direction. Now, the individual contributions of Eq. 2.21 are discussed in more detail.

Zero-Field Hamiltonian

The first and one of the strongest contribution to the static Hamiltonian is the *inter-electron interaction* Hamiltonian $\mathcal{H}_{\text{ZFS}}$. Since the two unpaired electrons of the NV centre are very close together, they have a strong dipole-dipole interaction. This interaction exists without an additional field and the resulting energy shift is therefore called zero-field splitting. It is described by the electron spin ($\boldsymbol{S}$) interaction connected with the ZFS tensor $\mathcal{D}$ as[37,43]

$$\mathcal{H}_{\text{ZFS}} = \boldsymbol{S}^{\dagger} \mathcal{D} \boldsymbol{S}, \tag{2.22}$$

where $\mathcal{D}$ is a symmetric ($\widetilde{D}_{ij} = \widetilde{D}_{ji}$) and traceless ($\text{tr}(\mathcal{D}) = 0$) tensor which can be diagonalised. Its diagonal elements fulfil $D_{xx} + D_{yy} + D_{zz} = 0$, which allows to rewrite Eq. 2.22 as

$$\mathcal{H}_{\text{ZFS}} = D_{xx} S_x^2 + D_{yy} S_y^2 + D_{zz} S_z^2. \tag{2.23}$$

For $S = 1$ systems like the NV centre, it only requires two independent parameters D and E to represent the symmetry and strain of the crystal field. Those parameters are connected with the ZFS tensor via $D = \frac{3}{2}D_{zz}$ and $E = \frac{D_{xx}-D_{yy}}{2}$, reducing Eq. 2.23 to

$$\mathcal{H}_{\mathrm{ZFS}} = D\left(S_z^2 - \frac{S(S+1)}{3}\right) + E\left(S_x^2 - S_y^2\right). \tag{2.24}$$

Considering the NV as distortion free ($D_{xx} \approx D_{yy}$), the associated strain parameter E is negligible compared to the ground state splitting $D = 2.87\,\mathrm{GHz}$. Consequently, the $S = 1$, inter-electron spin interaction Hamiltonian simplifies to

$$\mathcal{H}_{\mathrm{ZFS}} = DS_z^2. \tag{2.25}$$

Electron Zeeman Interaction Hamiltonian

The second contribution in Eq. 2.21, ranging from a weak disturbance to a very strong interaction, is the interaction of the electron spin with the magnetic field $\boldsymbol{B}$. This *electron spin Zeeman interaction* $\mathcal{H}_{\mathrm{B}}$ is dependent on the magnetic field's strength and orientation with respect to the electron spin $\boldsymbol{S}$. It connects both via

$$\mathcal{H}_{\mathrm{B}} = -\gamma_e \boldsymbol{B}^{\mathrm{T}}\boldsymbol{S}, \tag{2.26}$$

where $\gamma_e \approx 2.8\,\frac{\mathrm{MHz}}{\mathrm{G}}$ is the gyromagnetic ration of the NV centres' electron spin. For common measurements, the magnetic field is aligned along the quantisation axis z of the NV centre, resulting in $\boldsymbol{B} = (0, 0, B_z)^T$ and further leads to the final, aligned Zeeman interaction Hamiltonian

$$\mathcal{H}_{\mathrm{B}} = -\gamma_e B_z S_z. \tag{2.27}$$

In the case of a misaligned magnetic field, as it is necessary for the reconstruction EPR measurements (chapter 7), the assumption $\boldsymbol{B} = (0, 0, B_z)^T$ does not hold true. Therefore, a more general Zeeman interaction Hamiltonian, containing the magnetic field alignment, has to be considered. This leads to the angular dependency

$$\mathcal{H}_{\mathrm{B}} = -\gamma_e B_0\left[\cos(\theta)S_z + \sin(\theta)S_x\right], \tag{2.28}$$

with θ the misalignment angle between the magnetic field and the NV axis and B_0 the absolute field amplitude.

Hyperfine Interaction Hamiltonian

The third contribution to the system Hamiltonian Eq. 2.21 is the *hyperfine interaction* $\mathcal{H}_{\mathrm{HF}}$, describing the interaction between the NV centre's electron spin $\boldsymbol{S}$ and coupled nuclear spins $\boldsymbol{I}$. This Hamiltonian can be seen as two parts: the first part corresponds to the coupling with the very own nitrogen nuclear spin (e^-N), and the second part corresponds to the interaction with surrounding nuclear spins (e^-nuc). Consequently, the hyperfine interaction becomes

$$\mathcal{H}_{\mathrm{HF}} = \mathcal{H}_{\mathrm{HF}(e^-\mathrm{N})} + \mathcal{H}_{\mathrm{HF}(e^-\mathrm{nuc})}. \tag{2.29}$$

While the contribution of the ZFS and magnetic field Hamiltonian have a large impact on the NV energy levels (on the order of some GHz), the hyperfine interaction with the own nitrogen atom is only on the order of a few MHz.
For the first part of the hyperfine interaction, the connection between the nuclear spin $\boldsymbol{I}$ and the electron spin $\boldsymbol{S}$ is characterized by the hyperfine interaction tensor $\mathcal{A}$ with

$$\mathcal{H}_{\mathrm{HF}(e^-\mathrm{N})} = \boldsymbol{I}^\dagger \mathcal{A} \boldsymbol{S}. \tag{2.30}$$

Similar to the case of the ZFS tensor $\mathcal{D}$, the hyperfine interaction tensor is also symmetric ($A_{ij} = A_{ji}$) and can therefore be diagonalised with its parallel $A_\parallel$ and perpendicular $A_\perp$ components as diagonal elements. For nuclei with $I \geq 1$ there exists an additional contribution by the quadrupole moment with a non-zero quadrupole interaction $\mathcal{P}$. Combining this, the hyperfine interaction Hamiltonian can be written as

$$\mathcal{H}_{\mathrm{HF}(e^-\mathrm{N})} = A_\parallel S_z I_z + A_\perp \left(S_x I_x + S_y I_y\right) + \mathcal{P} I_z^2. \tag{2.31}$$

As discussed in Sec. 2.1.1, there exist two nitrogen isotopes ^{14}N and ^{15}N. Consequently, the nitrogen atom of the NV centre can carry different nuclear spin numbers I_n, dependent on the type of isotope present.
For the ^{14}N isotope, which has a nuclear spin $I_n = 1$, the non-zero quadrupole interaction $\mathcal{P}$ has to be taken into account. Whereas, for the ^{15}N the nuclear spin $I_n = \frac{1}{2}$ results in no quadrupole interaction, simplifying Eq. 2.31 by setting the third term to zero. The different interaction constants are given in Tab. 2.3.

Table 2.3: The hyperfine parameters $A_\parallel$, $A_\perp$, and $\mathcal{P}$ for the nitrogen spin interaction in the NV centre. This particular table for the isotopes ^{14}N and ^{15}N is taken from Felton et al.[44].

Isotope type	$A_\parallel$ in MHz	$A_\perp$ in MHz	$\mathcal{P}$ in MHz
^{14}N	−2.14	−2.70	−5.10
^{15}N	3.03	3.65	-

Due to the hyperfine interaction, the energies of the electron spin states split further as depicted in Fig. 2.10. The allowed transitions are nuclear spin state conserving and thus of the form $\Delta m_S = \pm 1$ and $\Delta m_I = 0$. Therefore, the $m_s = 0 \leftrightarrow m_s = \pm 1$ transition frequencies are split isotope-dependent into triplets or doublets: For the ^{14}N isotope, the splitting leads to three transition frequencies, split by $\Delta\nu = 2.2$ MHz, ordered symmetrically around the $\mathrm{m}_I = 0$ transition. For the ^{15}N isotope, the difference between the two possible frequencies is $\Delta\nu = 3.1$ MHz.[45]

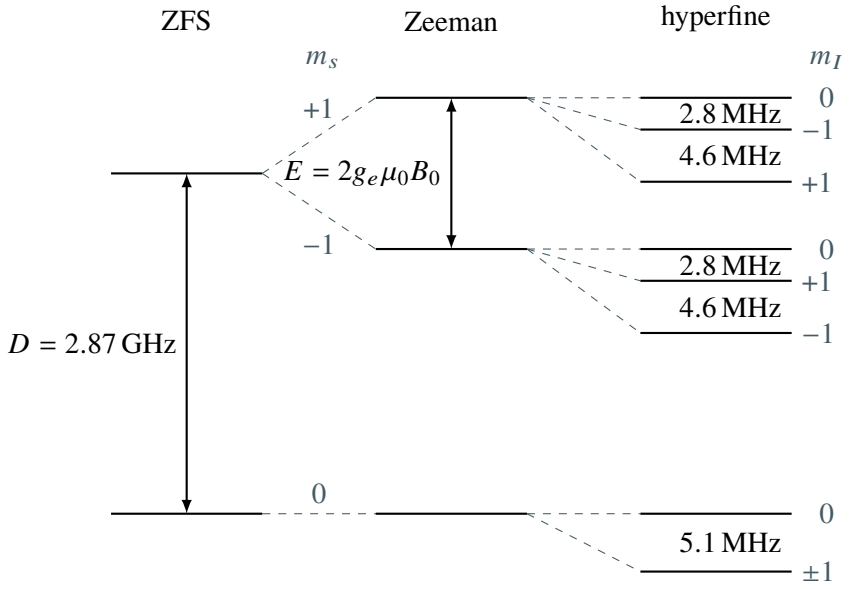

Figure 2.10: Exemplary energy level scheme for the NV centre with a ^{14}N isotope. Included are the static effects of the ZFS, the electron spin Zeeman interaction, and the hyperfine interaction. The allowed transitions are nuclear spin state conserving and thus of the form $\Delta m_S = \pm 1$ and $\Delta m_I = 0$.

The second part of the hyperfine interaction is the magnetic dipole-dipole interaction between the NV and other nearby nuclear spins. It can be written according to Cai et al.[46] and in agreement with the general dipolar interaction described by Eq. 2.10 as

$$\hat{\mathcal{H}}_{\mathrm{HF}(e^-\mathrm{spin})} = \sum_i d_i \ \{3\,(\boldsymbol{S}\cdot r_i)\,(\boldsymbol{I}_i\cdot r_i) - \boldsymbol{S}\cdot\boldsymbol{I}_i\}\,. \tag{2.32}$$

Here, the only difference compared to Eq. 2.10 is the mixture of an electron spin with nuclear spins, and due to that, the exchange of the gyromagnetic ratios by the proper species $\gamma_e\gamma_n$. As a result, the interaction strength is defined by $d_i = \frac{\mu_0\gamma_e\gamma_n\hbar}{4\pi|\boldsymbol{r}_i|^3}$ and refers to the i-th coupled nuclear spin with the connection vector $\boldsymbol{r}_i$.
The energy mismatch resulting from the high ZFS does not allow direct spin flip-flop processes, which permits the secular approximation[47] simplifying Eq. 2.32 to

$$\mathcal{H}_{\mathrm{HF}(e^-\mathrm{spin})} = S_z \sum_i g_i \ \left\{3r_z\left(r_{i,x}I_{i,x} + r_{i,y}I_{i,y}\right) + \left(3r_{i,z}^2 - 1\right)I_{i,z}\right\}. \tag{2.33}$$

Dipolar Interaction Hamiltonian

Similar to the hyperfine interaction with proximal nuclear spins, the NV centre is also sensible to electron spins in close proximity. The coupling is defined by Eq. 2.11 with the second spin operator - the NV spin operator - independent of the summation. Hence, Eq. 2.11 can be simplified to

$$\mathcal{H}_{\mathrm{Dip}} = S_z \sum_i d_i \ \left(1 - 3\cos^2\zeta_i\right)\ S_i^z. \tag{2.34}$$

Additionally to the direct interaction, the coupled electron spins are also influenced by the magnetic field. Thus, their Zeeman effect (similar to Eq. 2.27) contributes to the total Hamiltonian via

$$\mathcal{H}_{e^-,\text{Zeeman}} = -\gamma_e \sum_i B\ S_i^z, \tag{2.35}$$

for each i-th coupled electron spin.

2.4.2 Time-Dependent Interaction Hamiltonian

If an additional driving field is applied to the NV centre, a time-dependent perturbation leads to a state transition of the electron spin state. This *time-dependent interaction* Hamiltonian $\mathcal{H}_{\text{int}} = \mathcal{H}_{\text{int}}(t)$ is introduced by a controlled, oscillating magnetic field $\boldsymbol{B}(t)$, which leads to a perturbation of the system. This magnetic field is generated by MW radiation applied to the NV centre.[48] Hence, the interaction Hamiltonian reads

$$\mathcal{H}_{\text{int}}(t) = -\gamma_e \boldsymbol{B}(t)\, \boldsymbol{S}. \tag{2.36}$$

Comparing the microwave field's z contribution with the large effect of the electron Zeeman interaction, it is negligible. Furthermore, with no loss of generality, the interaction axis can be chosen freely as long as the two candidates x' and y' form a complete basis with z. Thus, without any limitations, the interaction can be chosen to be parallel to one of the two directions of the spin system.
For a MW field with oscillation frequency ω_{mw} and the assumption to have the interaction parallel to the x direction of the spin system, the magnetic field can be written as $\boldsymbol{B}(t) = (B_x \cos(\omega_{mw} t), 0, 0)^T$. This allows to simplify the interaction Hamiltonian to

$$\mathcal{H}_{int}(t) = -\gamma_e B_x \cos(\omega_{mw} t)\, S_x. \tag{2.37}$$

By applying a linearly polarised resonant MW field, a state transition is performed, driving the $m_s = 0 \leftrightarrow m_s = -1$ or $m_s = 0 \leftrightarrow m_s = +1$ transition.

2.4.3 Integration of the Individual Hamiltonian Contributions

In summary, including all individual terms into the NV spin Hamiltonian shown in Eq. 2.20, the full system is described by the total Hamiltonian:

$$\begin{aligned}\mathcal{H} = & DS_z^2 \\ & - \gamma_e B_z S_z \\ & + A_\parallel S_z I_z + A_\perp \left(S_x I_x + S_y I_y\right) + \mathcal{P} I_z^2 \\ & + S_z \sum_i g_i \left\{3r_z \left(r_{i,x} I_{i,x} + r_{i,y} I_{i,y}\right) + \left(3r_{i,z}^2 - 1\right) I_{i,z}\right\} \\ & + S_z \sum_i d_i \left(1 - 3\cos^2 \zeta_i\right) S_i^z - \gamma_e \sum_i B\, S_i^z \\ & - \gamma_e B_x \cos\left(\omega_{mw} t\right) S_x . \end{aligned} \tag{2.38}$$

With Eq. 2.38, not only the time-independent system Hamiltonian is taken into account, but also the time-dependent interaction introduced by a MW field. Therefore, this system representation allows to discuss all encountered phenomena of this work.

2.4.4 Effect of a Driving Field

Spin state manipulations, that is performing quantum gates, is the underlying technique for all sensing experiments. This requires a more precise investigation of the effect of a driving field introduced with Eq. 2.37.

For sake of simplicity, the system Hamiltonian can be transformed into the *rotating frame* by using the transformation $\mathcal{H}_{\text{rot}} = U\mathcal{H}U^\dagger + i\hbar\frac{\partial U}{\partial t}U^\dagger$ (described more closely in chapter 9). The required transformation operator for the here present two-level system with a strong and constant magnetic field in the z-direction is given as $U = e^{-i\frac{\omega_0 t}{2}\sigma_z}$ with $\omega_0 = \frac{E_e - E_g}{\hbar}$. Here, E_e is the energy of the excited states, $|\pm 1\rangle$ and E_g is the ground state energy of $|0\rangle$.

Rewriting the system Hamiltonian in terms of energy and neglecting the weak interaction terms (hyperfine interaction and dipolar couplings) then results in

$$\mathcal{H} = -\frac{\hbar\omega_0}{2}\sigma_z - \gamma_e B_x \cos\left(\omega_{mw} t - \delta_0\right)\sigma_x . \tag{2.39}$$

Herein, an additional phase δ_0 is introduced, which gives information about the switching time of the harmonic radiation (more closely discussed in Sec. 3.1.3).

For a static magnetic field aligned with respect to the NV axis, the only difference compared to the zero-field system is the shift of the transition energy $\hbar\omega_0$. Rewriting the final Hamiltonian in terms of σ_x and σ_y leads to

$$\hat{\mathcal{H}}_{\text{rot}} = -\frac{\gamma_e B_x}{2}\left(\cos\left(\delta_0\right)\sigma_x + \sin\left(\delta_0\right)\sigma_y\right). \tag{2.40}$$

From Eq. 2.40, it becomes evident that is possible to perform rotations around the different axes in the xy-plane by controlling the phase of the interaction.

2.4.5 Vector Magnetometry

For NV sensing experiments it is a crucial tasks to determine the magnetic field alignment with respect to the NV principal axis. This requires an understanding of the effect an applied, static magnetic field has on the respective NV transition frequencies.
Assuming that the magnetic field is interacting strongly with the NV centre, only the zero-field Hamiltonian in combination with the Zeeman interaction Hamiltonian needs to be considered in the calculation, thus neglecting all weakly interacting terms. Yet, it is important to keep the distortion parameter E of the zero-field Hamiltonian from Eq. 2.24. Thus, the spin Hamiltonian can be expressed as

$$\mathcal{H} = D\left(S_z^2 - \frac{S(S+1)}{3}\right) + E\left(S_x^2 - S_y^2\right) + \mu_B g \boldsymbol{B}^{\mathrm{T}} \boldsymbol{S}. \tag{2.41}$$

As depicted in Fig. 2.11, the magnetic field vector $\boldsymbol{B}$ can be determined by three parameters: the B-field amplitude $B = |\boldsymbol{B}|$ and the two angles θ and ϕ.

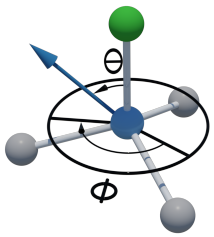

Figure 2.11: The magnetic field vector (blue) and its corresponding angles θ and ϕ with respect to the NV principal axis connecting the nitrogen atom (green) and the vacancy (blue).

According to Balasubramanian et al.[49], those B-field parameters can be determined for the spin levels of equation Eq. 2.41 by the characteristic polynomial

$$x^3 - \left(\frac{D^2}{3} + E^2 + \beta^2\right)x - \frac{\beta^2}{2}\Delta - \frac{D}{6}\left(4E^2 + \beta^2\right) + \frac{2D^3}{27} = 0, \tag{2.42}$$

with the alignment factor $\Delta = D\cos(2\theta) + 2E\cos(2\phi)\sin^2\theta$ and the B-field parameter $\beta = \mu_B g B$. Following their calculation[49], the solution for the magnetic field amplitude and alignment can be determined by the frequencies ν_1 and ν_2 of the $|m_s = 0\rangle \leftrightarrow |m_s = \pm 1\rangle$ transitions. Then the amplitude B is calculated via

$$B = \frac{1}{3\mu_B g}\left(\nu_1^2 + \nu_2^2 - \nu_1\nu_2 - D^2 - 3E^2\right). \tag{2.43}$$

Likewise, the alignment factor can be expressed in terms of frequencies as

$$\Delta = \frac{7D^3 + 2(\nu_1 + \nu_2)\left[2\left(\nu_1^2 + \nu_2^2\right) - 5\nu_1\nu_2 - 9E^2\right] - 3D\left(\nu_1^2 + \nu_2^2 - \nu_1\nu_2 + 9E^2\right)}{9\left(\nu_1^2 + \nu_2^2 - \nu_1\nu_2 - D^2 - 3E^2\right)}. \tag{2.44}$$

A further comparison with the alignment factor from Eq. 2.42 uncovers a relation between the alignment angles and the transition frequencies.
For a NV centre the distortion parameters are usually much smaller than the ZFS. Therefore, the alignment factor can be reduced and the tilt angle is determined by

$$\theta = \frac{1}{2}\arccos\left(\frac{\Delta}{D}\right). \tag{2.45}$$

Summarising, this chapter gives an overview about the material and physical properties of the NV as a sensor for magnetic resonance detection of magnetic fields, nuclear spins, and electron spins with their various interactions. Additionally, by the modelling of the system Hamiltonian, a framework for a more elaborate discussion of the in this work employed measurement methods, as well as the obtained results is build up.

3 Methodology and Spin Dynamics

The measurable quantities in the laboratory are ultimately determined by the basic structure and energy manifold of a NV centre. In the foregoing chapters, the relevant physical model to describe the NV defect in diamond was developed and, subsequently, an introduction to the corresponding measurements and the description of their schemes is required. Therefore, this chapter is dedicated to the methodology of the for this work performed measurements, the individual resulting spin dynamics, and the general interpretation approaches of any obtained outcomes.

As a beginning, the basic methods determining the important preliminary factors for all NV based measurements are explained. Continuing on with that information, more complex schemes for environmental sensing are introduced to conclude the necessary basis for the final section: the measurements combining the NV electron spin interacting with proximal nuclear and electron spins.

3.1 Characterisation of the NV Parameters

For any type of NV-based sensing measurement, it is important to be able to initialise the NV's electron spin state - further also referred to as the *NV state* - in a well-defined and controllable way. This is achieved by laser illumination, transferring the NV's current state into the $m_s = 0$ state. Yet, this process is dependent on the coupling of the lights' electromagnetic field to the NV dipole, consequently, the excitation efficiency is linked to the polarisation of the laser beam.

After the initialisation of the NV electron spin state, the NV would be exposed to all its environmental effects, resulting in a state transition (decay) into its thermal equilibrium. This resulting state is generally described by the superposition of the spin states, with the probability amplitudes dependent on the NV environment.
To allow more complex sensing schemes, the spin state has to be addressed in a more elaborate way. Due to its MW addressability (Sec. 2.4.4) this can be done via resonant electromagnetic field generation applied proximally to the measured NV centre. This requires a determination of the resonance frequency of the spin state transition. Additionally and due to the amplitude dependency of the driving field onto the transition rate, the duration for the different state transition interactions has to be determined as well.

3.1.1 Polarisation Anisotropy

As described in Sec. 2.2.2, the NV centre can occur in four different orientations incorporated into the diamond lattice. Yet, since they are dependent on the directionality of the beam path and the polarisation of the excitation laser, those four orientations are not optically distinguishable. Due to the employed sample type and optical build-up in this work (further described in chapter 4), only the (001) diamond surface orientation and [001] beam path direction are considered. As a result, the four possible NV orientations are projected into the optically accessible two-dimensional xy-plane, depicted in Fig. 3.1. Therein it becomes visible how the four axes are grouped into two subsets of two parallel axes each and the angle between the two remaining optical directions is given by 90°.

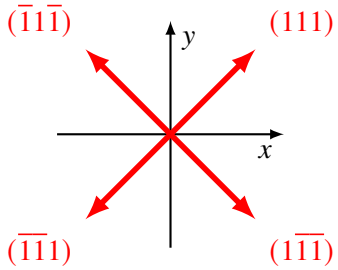

Figure 3.1: Projection of the four NV axes into the optically accessible xy-plane. Due to the experimental build-up and the lattice incorporation of the NV, two orientations are each similarly addressed by the laser light.

Dependent on the type and orientation of the laser polarisation, the overall fluorescence signal of the NV centre varies. For the used linear polarisation, the electric field is confined to a single plane. The relative orientation of this plane can be changed by a half-wave plate in the optical beam path. Hereby, the orientation change depends on the angle α between the polarisation direction of the incident beam and the crystallographic axis of the wave plate. After propagation through the wave plate, the relative orientation is given by $-\alpha$. By varying this relative angle α the laser polarisation can be matched to the actual NV orientation by signal maximisation. The overall signal $I(\alpha)$ is following a sinusoidal behaviour, with

$$I = I_0 \sin\left(\frac{2\pi}{p}\alpha + \alpha_0\right) + \kappa, \tag{3.1}$$

where I_0 is the NV fluorescence difference between parallel and orthogonal polarisation of the incident light, α_0 the angular offset (defined by the NV orientation, the initial laser polarisation direction, and the installation of the half-wave plate), and κ the signal offset (defined by the fluorescence signal of orthogonal light).

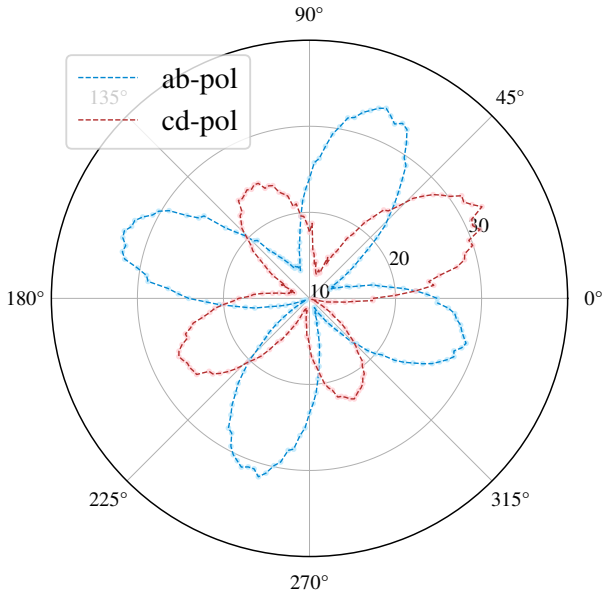

Figure 3.2: Polarisation anisotropy measurement of optically distinguishable NV orientations. Due to the relative orientation between the diamond crystal lattice and the optical beam path, two different NV orientations are coupled similarly to the electromagnetic light field. Those two orientations are henceforth referred to as **ab-pol** (blue) and **cd-pol** (red) NVs.

The exemplary plots for the two optically differentiable NV orientation 2-tuples are shown in Fig. 3.2. Furthermore, NVs are referred to by their orientation as **ab-pol** and **cd-pol** NVs.

3.1.2 Optically Detected Magnetic Resonance (ODMR)

Certainly a very crucial information for NV based measurements is the knowledge of the resonance frequencies for the possible spin state transitions ($|0\rangle \leftrightarrow |\pm 1\rangle$). For this determination, a common measurement technique is the **Optically Detected Magnetic Resonance** (ODMR). Following its name, ODMR generally relies on the optical addressability (described in Sec. 2.2.2), as well as the MW frequency accessibility (Sec. 2.4.4) of the spin state transitions[48].

In ODMR, green laser light is applied to the specimen, making the NV centre detectable by its red fluorescence. Simultaneously, a MW radiation field with variable frequency is generated in the NVs' proximity. Then, by sweeping the frequency of the MW field around the expected transition frequency, a reduction of the red fluorescence signal is observed if the resonance condition $\hbar\omega_{mw} \sim \hbar\omega_0 = \Delta E = E_e - E_g$ is fulfilled.
For the description of this process, the steady-state situation of an equilibrium between the continuous excitation and the different decay processes is assumed. According to Jensen et al.[50], the overall appearance of the signal is dependent on the detuning $\delta = \omega_0 - \omega_{mw}$ of the microwave field and has a Lorentzian lineshape:

$$I(\delta) = I(\infty)\left[1 - \frac{C\gamma^2}{\delta^2 + \gamma^2}\right]. \tag{3.2}$$

Here, $I(\infty)$ is the signal for off-resonant excitation, C is the contrast of the resonance, and 2γ is its **Full Width Half Maximum** (FWHM). In addition, the broadness of the Lorentzian is dependent on the amplitude of the MW field, meaning, a higher field amplitude leads to a broader magnetic resonance signal and vice versa.

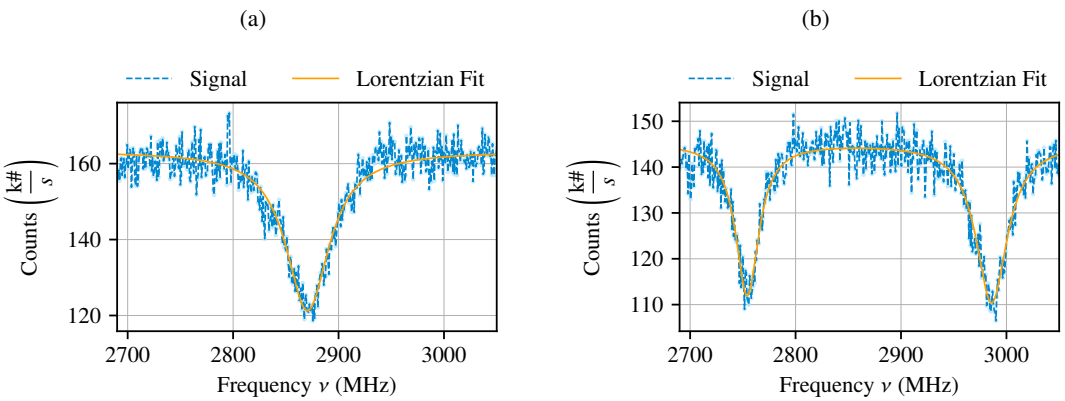

Figure 3.3: ODMR measurements (a) without an external field $B = 0\,\mathrm{G}$ and (b) with external magnetic field $B = (41.5 \pm 1.4)\,\mathrm{G}$. The peak with the lower transition frequency corresponds to the $|0\rangle \leftrightarrow |-1\rangle$ transition. The individual peaks are fitted by single Lorentzian functions.

Dependent on the environment, the single Lorentzian peak shown in Fig. 3.3a can split up into multiple peaks.

A very common effect which leads to a splitting of the ODMR signal is the Zeeman effect (Sec. 2.4.1). Here, a static magnetic field applied to the NV centre lifts the degeneracy of the $|m_s = \pm 1\rangle$ states. This splits the signal into two dips for its transition frequencies ($|0\rangle \leftrightarrow |-1\rangle$ and $|0\rangle \leftrightarrow |+1\rangle$) (Fig. 3.3b).
Another reason for a splitting of the signal are proximal spins coupled strongly to the NV centre. This strong coupling can lead to a multitude of resonance dips as, for example, proximal carbon nuclear spins can result in a splitting into two, three, or up to four dips[51]. The number of visible resonance dips here is dependent on the atomic lattice distance (shell) to the NV centre and their respective coupling strength.

3.1.3 Rabi Oscillations

In order to measure magnetic resonances of other spins and fields, the NV has to be in a state with a non-zero magnetic moment. Yet, after the initialisation, the NV is in the $|0\rangle$ state with zero magnetic moment. To fulfil the requirement, the NV spin has to be transferred into either the $|\pm 1\rangle$ states or a superposition of the different spin states. Such an arbitrary superposition state $\alpha\,|0\rangle + \beta\,|\pm 1\rangle$, can be achieved by applying a MW field resonant to the NV transition frequency ω_{mw}. Hereby, the final state probability amplitudes α and β are dependent on the duration τ_{mw} of the MW interaction, as well as on the initial state of the NV previous to the manipulation. A continuous driving of the MW field results in population oscillations of the spin states, also called *Rabi oscillations*.[19]

In order to measure Rabi oscillations, the measurement sequence as depicted in Fig. 3.4a is performed. In the beginning, the spin state is optically initialised into the $|0\rangle$ state. After this initial state definition and to sample the state population transfer of the system, the MW field is applied for different durations τ_{mw} to the NV. In the end, the concluding state readout is another laser pulse, encoding the NV spin state into the fluorescence signal.
Plotting this fluorescence signal as a function of the pulse duration τ_{mw}, the Rabi frequency and period can be determined (exemplary measurement shown in Fig. 3.4b).

The overall shape of the signal is sinusoidal and can be approximated by

$$I(t) = A \sin(\Omega t + \delta) + I_0, \tag{3.3}$$

with the Rabi frequency Ω_{Rabi}, the phase δ, and the mixed state signal I_0. Therefore, the Rabi period is given by $T_{\text{Rabi}} = \frac{1}{\Omega_{\text{Rabi}}}$.
Dependent on the accurateness of the MW frequency and signal, the oscillation can additionally show an exponential decay, combining effects arising from off-resonant driving. For a MW field with detuning Δ, the resulting oscillation frequency is given as $\Omega_{\text{eff}} = \sqrt{\Omega_{\text{Rabi}}^2 + \Delta^2}$.[52]

As discussed in Sec. 2.4.4, the spin state manipulation can lead to different rotation axes dependent on the relative phase δ_0 with respect to the rotating wave frame of reference (see Eq. 2.40). Hereby, the beginning of the first MW manipulation after the initialisation determines the time $\tau_0 = 0$,

reference for all further MW phases.
The effect of the phase δ_0 can be visualised on the Bloch sphere (Fig. 3.5), where the MW phase determines the rotation axis. In case of a zero phase $\delta_0 = 0$, the rotation axis coincides with the x-direction, leading to a rotation of the state vector in the yz-plane with Rabi frequency $\Omega_{\text{Rabi}} = \gamma_e B$ (Fig. 3.5a). In comparison, if the relative phase of the signal is shifted a quarter period, corresponding to a phase $\delta_0 = \frac{\pi}{2}$, the rotation axis is along the y-axis and the plane of rotation for the state is the xz-plane (Fig. 3.5b).
Accordingly, for measurements with variable relative phases, MW manipulations are going to be denoted with their respective phase in the index. Since the most common techniques employ either a zero- or a $\frac{\pi}{2}$-phase, those are going to be referred to as x- or y-phase.

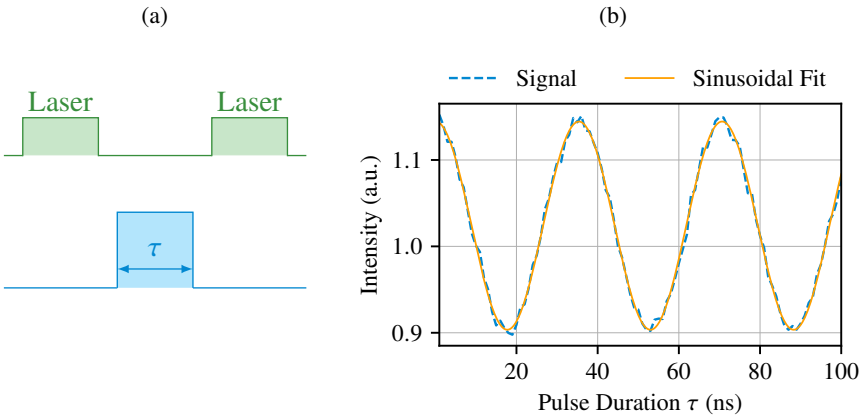

Figure 3.4: (a) Schematic Rabi measurement sequence with an altered microwave pulse duration τ (blue). The initialisation and readout is done optically by laser pulses (green). (b) Exemplary obtained measurement result for the Rabi oscillation with Rabi period $T_{\text{Rabi}} = (35.27 \pm 0.03)$ ns.

The MW interactions of a defined strength and duration are going to be pulses, or spin flips whereof the most commonly used ones are π- and $\frac{\pi}{2}$-flips. In particular, a π-flip is a population inversion depicted by a 180° rotation on the Bloch sphere. In contrast, a $\frac{\pi}{2}$-flip results in a 90° rotation, most commonly used to create a superposition state $|\Psi\rangle = \frac{1}{\sqrt{2}}(|0\rangle + |\pm 1\rangle)$ or a projection into the population states, allowing a readout of the relative phase φ between the states.

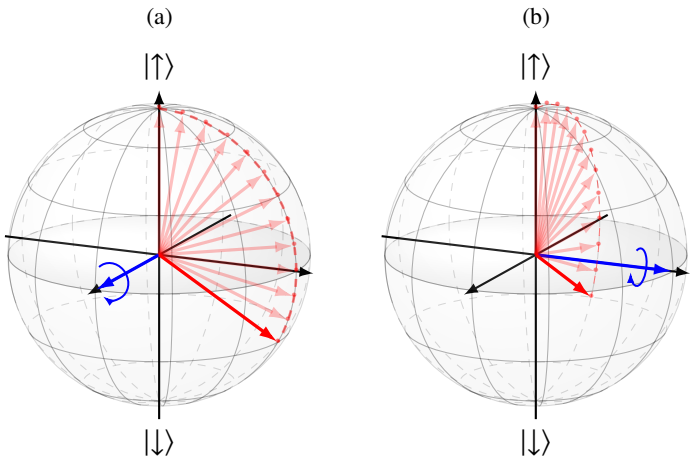

Figure 3.5: Rabi rotation on the Bloch sphere. The rotation axis (blue) for the state rotation (relative phase of superposition state) is dependent on the phase of the microwave field. The examples show (a) a clockwise rotation around the x-axis ($\phi = 0°$) and (b) a clockwise rotation around the y-axis ($\phi = 90°$). The final state is dependent on the duration of the interaction, here chosen to be $\tau = \frac{2\pi}{3\Omega}$ with the Rabi frequency Ω.

3.2 Sensing of the NV Environment

So far, measurements for the determination of NV manipulation parameters have been described and allow now to define more complex schemes for measurements of the NV environment. The environmental sensing schemes, here referred to as sequences, are frequency filter functions, consisting of different MW pulses separated by free evolution times τ. By variation of those times and pulses, the filter functions can be tuned to - or decoupled from - certain frequencies.

In the measurement, the varied quantities, like the free evolution time τ, are repeated consecutively and the total number of time- or frequency-points is denoted by N. Since each repetition has to have the initialisation in the beginning and the readout in the end, those two are combined. In particular, the fluorescence signal during the initialisation contains the state information of the previously measured quantity. Additionally and due to the shot noise limitation of the state readout, each cycle of the N measured points is repeated M times, reducing the noise of the measurement by a factor of $\frac{1}{\sqrt{M}}$, thus increasing the **signal to noise ratio** (SNR) accordingly (discussed in chapter 9).
The highest possible contrast $C_{\max}$ for those NV fluorescence-based measurements is determined by the bright state signal I_0 and the dark state signal I_1 via

$$C_{\max} = \frac{I_0 - I_1}{I_0}. \tag{3.4}$$

3.2.1 Pulsed Optically Detected Magnetic Resonance (pulsedODMR)

The first sensing experiment is dedicated to measure the NV transition frequencies more accurately than common ODMR (Sec. 3.1.2). By decreasing the MW power in continuous ODMR, the linewidth of the signal can be reduced[53]. Nevertheless, since continuous driving results in Rabi oscillations with power dependent Rabi period T_Ω, the effective measured intensity for fulfilling the resonance condition is time averaged. It thus depends on the fraction: *measurement duration t for a single frequency point to the Rabi period T_Ω for the corresponding power*. The time dependent superposition state can thus be approximated by

$$|\Psi\rangle \sim \cos\left(\frac{t}{T_\Omega}\pi\right)|0\rangle + e^{i\phi}\sin\left(\frac{t}{T_\Omega}\pi\right)|\pm1\rangle\,. \tag{3.5}$$

In conclusion, a simplified maximum contrast for continuous ODMR can be given by the intensities of the bright state signal and mixed state signal I_Ψ. Looking at the limits of this estimation, the contrast is given by

$\sim \frac{1}{2}C_{\max}$ for strong driving, and

$\sim C_{\max}$ for observation times matching ($\frac{2k-1}{2}T_\Omega$).

Yet, those estimations rely on an idealised system with no trapping effects due to strong laser intensity and an initial state $|\Psi\rangle = |0\rangle$ in the beginning of the observation.
A more elaborate scheme is to exchange the continuous driving and continuous readout with a pulsed version, the pulsed ODMR. This sequence is depicted in Fig. 3.6a. Due to the laser initialisation, the initial state is guaranteed to be $|\Psi\rangle = |0\rangle$ and with the subsequent π-pulse, a population inversion into the $|\pm1\rangle$ states is achieved. This results in the highest possible contrast $C_{\max}$.

Similar to the ODMR measurement, the lineshape is Lorentzian with a power dependent width. Thus decreasing the MW power with matching Rabi period, the linewidth can be narrowed down until the most proximal environment of the NV can be sensed.
For a linewidth on the order of some 100 kHz, the NVs' own nitrogen atom can be identified. As shown in Fig. 3.6b, the interaction with the ^{14}N nitrogen nucleus leads to a splitting of 2.1 MHz between the three resonance lines. If the linewidth gets reduced even further to roughly 10 kHz – 50 kHz, weakly coupled carbon nuclear spins[51] can be detected as an additional splitting of the dips.

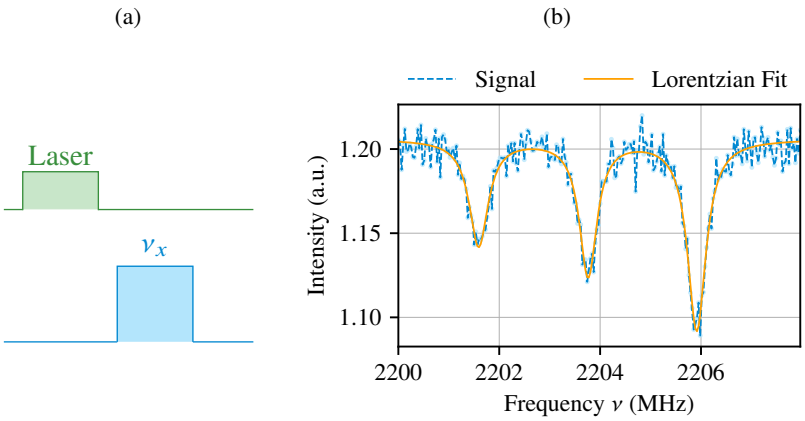

Figure 3.6: (a) Schematic pulsed ODMR measurement sequence where the microwave pulse frequency ν (blue) is altered and the duration is chosen power dependent to match a population inversion. The initialisation and readout are done optically by a laser pulse (green). (b) Exemplary obtained measurement result for the pulsed ODMR measurement with Rabi period $T_{\text{Rabi}} = 1.5\,\mu\text{s}$. The resonance frequency is split due to the ^{14}N of the NV with the three transition frequencies given by $\nu_1 = 2201.59\,\text{MHz}$, $\nu_2 = 2203.76\,\text{MHz}$, and $\nu_3 = 2205.92\,\text{MHz}$.

3.2.2 NV Lifetime Measurements

For NV based sensing experiments, the coherence time or lifetime – the time how long the NV stays in the given initial state – is crucial. During a free evolution time, the NV accumulates a phase due to the interaction with internal and external fields. This signal is given by a relative phase φ of the electron spin state and therefore a dephasing, or also called *decoherence* of the system.

As the sensed frequency ν is indirectly proportional to the duration τ between the pulses of the sequence, a lower bound for detectable frequencies can be estimated by the lifetime of the measured NV centre.

This lifetime is a parameter dependent on the environment of the individual NV centre and thus, it is crucial to determine it for each NV itself. Furthermore, since the diamonds' internal environment is mostly constant in time, those parameters have to be specified only once per site.

Thermal Relaxation

The longest lifetime of a NV is the thermal relaxation time or also called spin-lattice relaxation time. According to its name, this T_1-time is the time the NV spin state takes to decay back into its thermal equilibrium via phononic interaction with the diamond lattice.[54] These phononic interactions are strongly temperature-dependent, thus, the T_1-time can be prolonged even further using low-temperature measurements.

For the measurement of the $m_s = 0$ T_1-time, the free evolution time of the NV between the initialisation and the readout laser pulse is varied. If, in comparison the relaxation time of the $m_s = \pm 1$ state is measured, an additional π-pulse right after the initialisation is added (Fig. 3.7a).

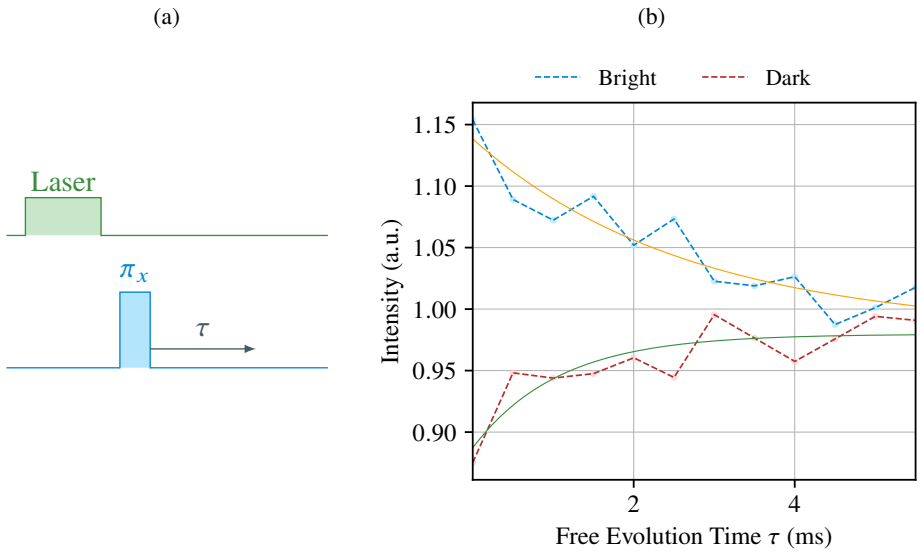

Figure 3.7: (a) Schematic thermal relaxation time measurement sequence where the free evolution time τ is altered. The π-pulse after the laser initialisation is optional if the T_1-time for the $m_s = \pm 1$ state is measured. Otherwise the T_1-time of the NV in the $m_s = 0$ state is measured. (b) Obtained measurement result for the T_1-time with $T_1 > 1$ ms.

In order to obtain the T_1-time, an exponential decay

$$I(\tau) \propto e^{-\tau/T_1} \tag{3.6}$$

is used as fit-function. Therefore, the T_1-time is the information about the duration it takes for the fluorescence signal to decay to $\frac{1}{e}$-th of its initial value.

Ramsey (FID)

The **Free Induction Decay** (FID) or T_2^* dephasing time can be measured by the *Ramsey pulse sequence* (Fig. 3.9a).[55] After the initialisation, a $\frac{\pi}{2}$-pulse creates a superposition state $|\Psi\rangle = \frac{1}{\sqrt{2}}\left(|0\rangle + e^{i\varphi_0}|-1\rangle\right)$. During the following free evolution time τ, the NV is exposed to its environment. The combination of all interactions during this evolution time can be summarised to an effective magnetic field B^*. The influence of this effective field causes an accumulation of the relative phase $\varphi(\tau)$ with

$$\varphi(\tau) = 2\pi\gamma_e \int_0^\tau B^*(t)\,\mathrm{d}t. \tag{3.7}$$

The final state after the free evolution can consequently be summarised by

$$|\Psi\rangle = \frac{1}{\sqrt{2}}\left(|0\rangle + e^{i(\varphi_0+\varphi(\tau))}|-1\rangle\right). \tag{3.8}$$

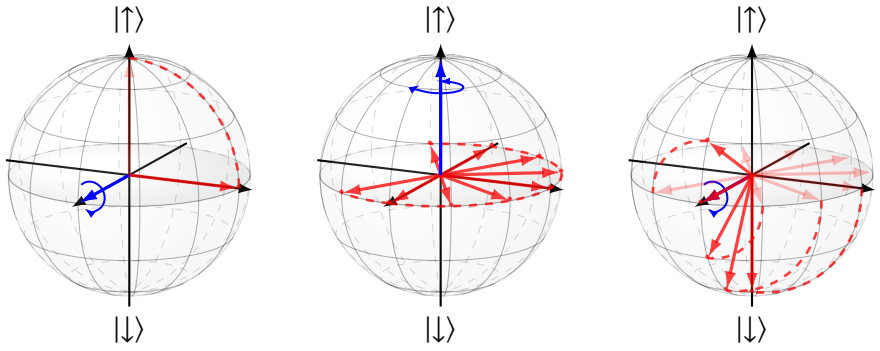

Figure 3.8: Effect of the Ramsey measurement onto the NV spin state depicted on the Bloch sphere. The rotation axis and direction is blue, the state before (faded) and after (solid) the individual interactions is a red vector, and the trajectories are red and dashed lines. For the sake of visibility of the second $\pi/2$-pulse plot, the trajectory of the population projection and the final states are only shown for states on the positive half-sphere ($x > 0$).
The first $\frac{\pi}{2}$-pulse rotates the state around the x-axis and creates a superposition state $|\Psi\rangle = \frac{1}{\sqrt{2}}\left(|0\rangle + e^{i\varphi_0}|-1\rangle\right)$. During the free evolution time τ, the effective field B^* leads to the accumulation of an additional phase $\varphi(\tau)$. The second $\frac{\pi}{2}$-pulse projects the resulting state into the population plane for the following readout.

Concluding the sequence, a second $\frac{\pi}{2}$-pulse maps the gained phase of the spin into the population states $|0\rangle$ or $|-1\rangle$.
The state change during the free evolution time of the FID sequence can be visualised on the Bloch sphere by a rotation of the state vector in the xy-plane around the z-axis (see Fig. 3.8). In the case of an unperturbed two-level system, this would lead to a sinusoidal oscillation, but due to the surrounding spins and the thus possible excitation transfer, a beating and decay of the signal can be observed.

From the measured FID signal, the T_2^* time can be inferred as the decay time of the envelope of the damped oscillations (Fig. 3.9b). The signal can be described by the convolution of sinusoidal functions with an exponential decay:

$$I(\tau) \propto \sum_i \cos\left(\omega_i \tau + \phi_i\right) e^{-\left(\tau/T_2^*\right)^p}. \tag{3.9}$$

Here, the parameter p is dependent on the type of noise in the systems environment, but usually set to $p = 2$. In summary: the T_2^* time gives information about the inverse linewidth of the magnetic field gradients[56](magnetic field inhomogeneity) affecting the NV spin state.

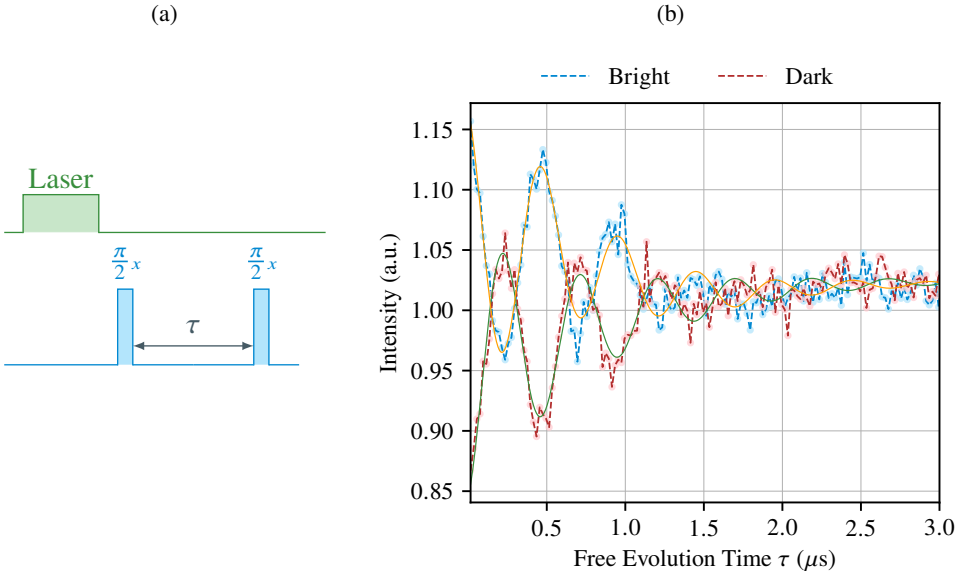

Figure 3.9: (a) Schematic FID measurement sequence where the free evolution time duration τ is altered. (b) Obtained measurement result for the T_2^* dephasing time where the oscillations originate from static noise of the NV environment, here $T_2^* = 740\,\text{ns}$ with two oscillation frequencies $\omega_1 = 2.03\,\text{MHz}$ and $\omega_2 = 240\,\text{kHz}$.

Hahn-Echo

A more advanced approach compared to the Ramsey measurement can be achieved by supplementing the Ramsey sequence (Fig. 3.9a) with an additional π-pulse during the free evolution time τ. The resulting sequence is the *Hahn-echo*[57,58] and is shown in Fig. 3.10a with a symmetric sequential arrangement.

If the free evolution times τ' and τ'' are equal, the π-pulse acts as a decoupling-pulse. This inverts the NVs' gained phase of both evolutions and thus decouples the NV from certain types of environmental noise. Following the mathematical description of Eq. 3.7, the decoupling effect can be introduced by an additional time-dependent function $f(t)$ describing the interaction-sign of the NV:

$$\begin{aligned}\varphi(\tau) &= 2\pi\gamma_e \int_0^{\tau} f(t)\, B^*(t)\, \mathrm{d}t \\ &= 2\pi\gamma_e \left[\int_0^{\tau/2} B^*(t)\, \mathrm{d}t - \int_{\tau/2}^{\tau} B^*(t)\, \mathrm{d}t\right]. \end{aligned} \tag{3.10}$$

It is striking that both contributions in Eq. 3.10 cancel each other out for static noise (with $B^*(t) = B^*$) or if the measurement duration τ is long compared to fluctuations of the environment (with $B^*(0) \simeq B^*(\tau/2) \simeq B^*(\tau)$). Therefore, the π-pulse can also be seen as a refocusing-pulse, leading to a refocus of the spin echo (also called *revival*) after the second free evolution. This effect is depicted in Fig. 3.11 where after the second free evolution time the initial state is recovered.

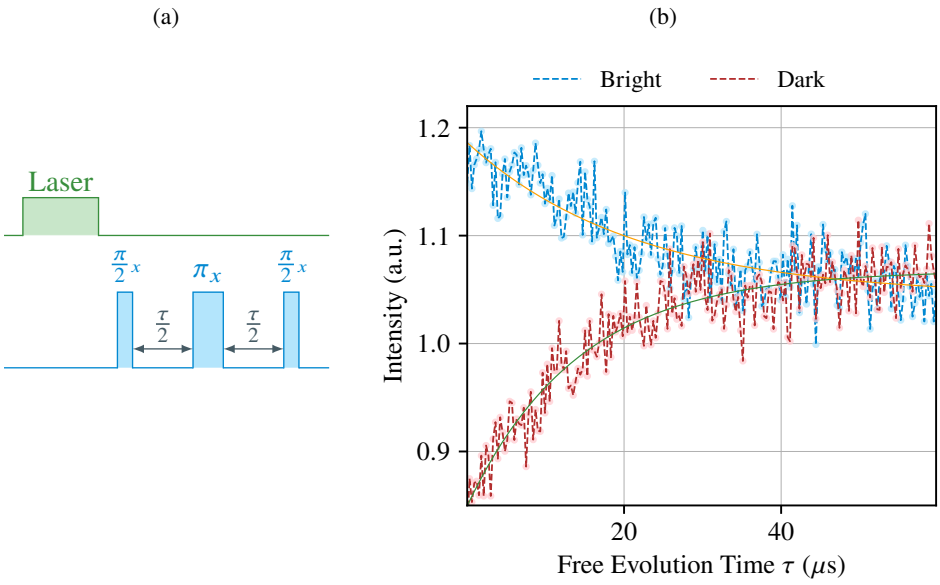

Figure 3.10: (a) Schematic Hahn-echo measurement sequence where the free evolution time durations $\frac{\tau}{2}$ are altered. (b) Obtained measurement result for the T_2 coherence time with $T_2 = (19.4 \pm 1.2)\ \mu$s.

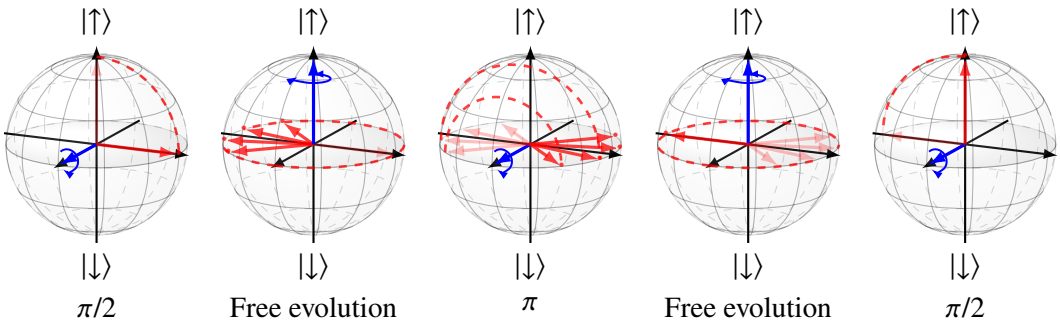

Figure 3.11: Effect of the Hahn-echo onto the NV spin state depicted on the Bloch sphere. The rotation axis and direction is blue, the state before (faded) and after (solid) the individual interactions are red vectors, and the trajectories are dashed red lines. For the sake of visibility of the π-pulse plot, the trajectory of the population projection are only shown for states on the positive half-sphere ($x > 0$). As a first step, a $\frac{\pi}{2}$-pulse rotates the state around the x-axis and creates a superposition state $|\Psi\rangle = \frac{1}{\sqrt{2}}\left(|0\rangle + e^{i\varphi_0}|-1\rangle\right)$. During the second step, the free evolution time τ, the effective field B^* leads to the accumulation of an additional phase $\varphi(\tau)$. In the third step, the π-pulse inverts the phase and therefore leads to a cancelling out effect of the previously gained phase in the forth step. The second $\frac{\pi}{2}$-pulse is the last step and projects the resulting state into the population plane for the following readout.

During the first free evolution time, the state gains a phase dependent on the environment, as depicted for four exemplary state vectors in the second step of Fig. 3.11. Due to the π-pulse, the phase is inverted, which then leads to a cancelling out effect of the previously gained phase during

the second free evolution and thus a recovery of the state after the population projection with the second $\pi/2$-pulse. This happens for all environmental noises which do not vary over the time of the measurement. If the rotation axis would additionally be tilted with respect to the z-axis, the state vector would leave the xy-plane in the first free evolution. Yet, after the π-pulse and the second free evolution, this static effect would also cancel out and the initial state could be recovered.
Overall, the Hahn-echo allows to suppress the prominent sinusoidal dephasing of the Ramsey measurement (Eq. 3.9) and is therefore given by merely the exponential decay

$$I(\tau) \propto e^{-(\tau/T_2)^p}. \tag{3.11}$$

The decay time of this measurement gives information about the state information loss due to the effect of coupled spins and is therefore called *spin-spin relaxation* time or T_2-time. It depends on the dephasing due to coupled spins and noise parallel to the z-axis. Comparing the T_2^*-time to the T_2-time, the latter is prolonged due to the decoupling from the inhomogeneity effects of the magnetic field and thus, only the homogeneous part of the magnetic field is taken into account.

As discussed, the T_1-time, the T_2-time, and the T_2^*-time are intrinsic parameters to the NV, they are further referred to as *lifetime of the NV*. Whereas, the term coherence time, even so describing the same effect of decoherence, is used more globally. Therefore, also the 'prolonging of the time' a state can be reconstructed due to more complex sensing schemes is accounted for.

3.2.3 Dynamical Decoupling of the NV Dynamics

After the discovery of spin echoes like the Hahn-echo[57], many different schemes to suppress the undesired dephasing effects in sensing experiments have been developed. Those schemes rely on the time-dependent control and modulation of sequences to dynamically decouple the sensor from decoherence effects, thus, giving this category of measurements its name **Dynamical Decoupling** (DD). It is important to note, that DD sequences are based on open-loop control and are consequently independent of system feedback. In addition to their ability to increase the coherence time of NV centres, they also allow the detection of resonance signals of nuclear spins and electron spins, measured using **Nuclear Magnetic Resonance** (NMR) and EPR experiments. This is done by resonant tuning of the free evolution times to match certain frequencies.
In contrast to common NMR, sensing experiments with NV centres are based on two-state quantum systems (**Quantum Bit** (QuBit)s), nevertheless, many approved NMR schemes can be adapted and used similar for decoherence suppression in NV measurements.[59]

XY Sequence

As a first improvement of the Hahn-echo, it is evident to replace the single π-pulse during the free evolution time by N consecutive π-pulses, equidistant in time, leading to the *CPMG sequence*, named after the inventors **C**arr, **P**urcell, **M**eiboom, and **G**ill.[60,61] The resulting sequence allows

to decouple the NV even better from environmental effects and, thus, leads to an increase of the coherence time.

Yet, all π-pulses have the same phase in the rotating frame of reference, which results in a decoupling of noise solely from the orthogonal plane with respect to the rotation axis. If additionally to the increased number of π-pulses, their respective phase is altered, one arrives at the *XY-N* or *XY8* sequence.[62] Furthermore, the XY8-block which consists of the eight π-pulses and the total eight free evolution times (see Fig. 3.12) can be repeated N-times, with the number of repetitions also referred to as *order* of the XY sequence. Thus, the total free evolution time is given as $T = N_{\text{tot}}\tau = 8N\tau$.

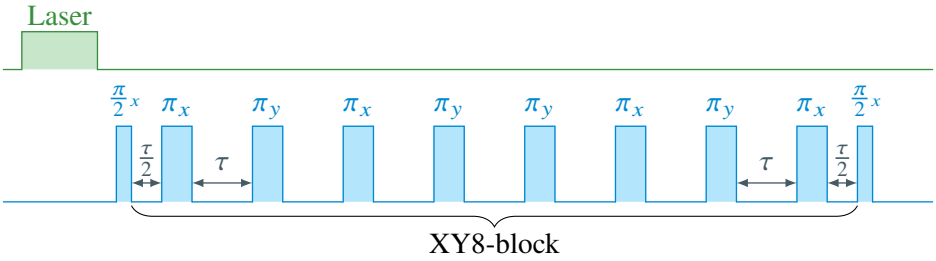

Figure 3.12: Schematic XY-N sequence with eight π-pulses arranged with alternating phase leading to a noise decoupling along both, the x- and y-axis. To increase the order, the XY8-block in-between can be repeated N times. The whole XY-N sequence is enfolded by two $\frac{\pi}{2}$-pulses, the laser initialisation, and the readout.

In general, such sequences lead to a noise cancellation of high frequent environmental noise. But, if the free evolution time is resonant with the frequency ν of the noise, it leads to an accumulation of the signal. This effect can be understood by consideration of a signal with period $T = \frac{1}{\nu}$. If the period of this signal coincides with a single sensing block ($\tau - \pi - \tau$) of the DD sequence, the gained phase during both free evolution times add up. Therefore, the coherence of the NV gets lost and a signal at $\tau = \frac{T}{2} = \frac{1}{2\nu}$ can be observed. This signal arises consequently due to the coupling between the spins and allows to gather information about their interaction.

Since also higher harmonics of the signal can superpose with this resonance condition, signals at higher frequencies $k\nu$, with k even, can be measured.[63] Taking those higher harmonics into account, a more general resonance condition can be formulated:[64]

$$\tau_k = \frac{2k-1}{2\nu}, \quad \text{with } k \in \mathbb{N}, \tag{3.12}$$

As also nuclear spins in a magnetic field produce small **alternating current** (ac) fields, those signals can be detected by the NV centre. By use of the specific Larmor frequency ω_{Larmor} and the parallel component of the hyperfine interaction $A_\parallel$, the resonance condition for such NMR spectroscopy measurements can be formulated more precise:

$$\tau_k = \frac{(2k-1)\pi}{\omega_{\text{Larmor}} + A_\parallel}, \quad \text{with } k \in \mathbb{N}. \tag{3.13}$$

Here, the hyperfine interaction has to be taken into account due to the shift of the effectively sensed Larmor frequency.[65]
For DD measurements, the totally gathered phase is dependent on the strength of the resonant signal, though for a higher order N, weak signals can be amplified due to the increased number of repetitions and the such resulting summation of the phase. Additionally, due to the filter function, which is given by the DD sequence, and the higher number of repetitions, a more narrow-banded signal detection can be achieved. Being more precise, the spectral resolution of the detected frequency ν is limited in the linewidth by $\Delta\nu \propto \frac{1}{8N\tau}$.

AXY Sequence

Another DD protocol tailored further towards not only the suppressing of noise, but the detection of spins coupled to the NV centre is the adaptive XY-N (AXY-N) sequence.[66] In comparison to the XY-N sequence, it is based on a more elaborate way of designing the filter function with non-equally-spaced decoupling pulses[67]. Thus, it is more precise and tunable to the signal of proximal nuclear and electron spins.
By varying the phases and the spacing between the individual pulses, this sequence can be adjusted to different type of signals. The here employed version consists of eight pulse blocks and two variable free evolution times τ_c and τ_d. Similar to the XY-N sequence, the eight pulse blocks can be seen as each four effective X- and Y-blocks (see Fig. 3.13a).
Comparably to the XY-N sequence, the detectable frequencies are dependent on the sensing duration τ_{DD} between the different π-pulse. For the AXY-N sequence, τ_{DD} is composed of the free evolution times τ_c between the five π-pulses of one X (Fig. 3.13b) and one Y-block (Fig. 3.13c) and the free evolution time connecting those two blocks. This leads to the sensing time

$$\tau_{DD} = 8\tau_c + 4\tau_d, \tag{3.14}$$

and, thus, the detected frequencies

$$\nu = \frac{1}{\tau_{DD}} = \frac{1}{8\tau_c + 4\tau_d}. \tag{3.15}$$

For the linewidth, the entire measurement duration has to be taken into account and by increase of the order, a better frequency resolution can be achieved:

$$\Delta\nu \propto \frac{1}{4N\tau_{DD}}. \tag{3.16}$$

Since the signal strength of the AXY-N measurement is dependent on different parameters, a variety of related AXY measurements is necessary to determine the optimal settings for the best signal detection.
Hereof, the main parameters influencing the detection of the signal are the AXY order and total duration (conditional parameters), the dipolar coupling strength (fixed/wanted parameter), and the Fourier amplitude.

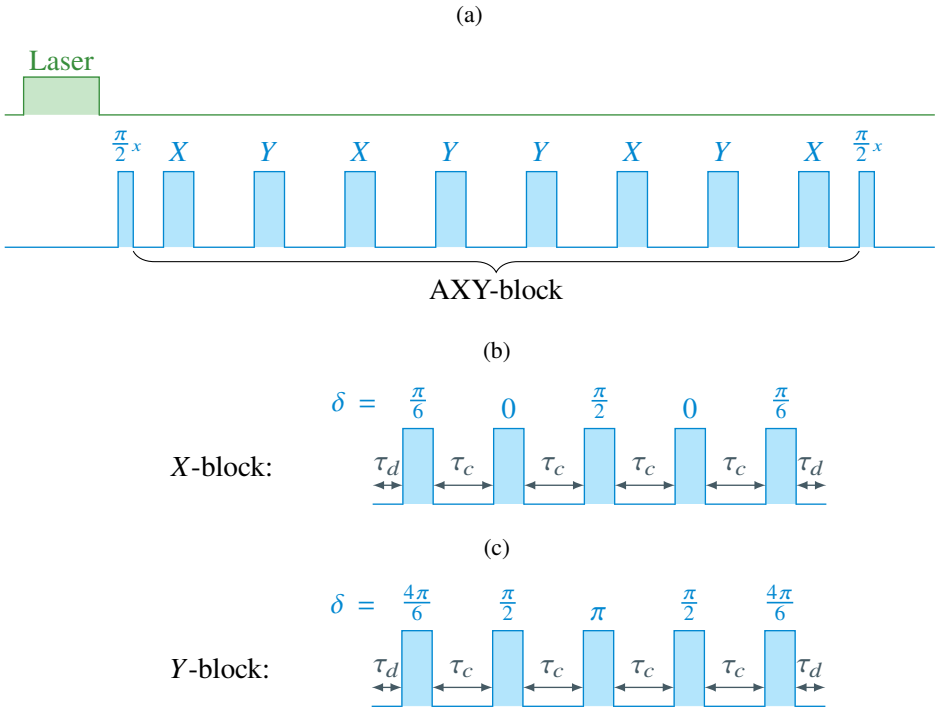

Figure 3.13: (a) Schematic AXY-N sequence with four times two effective pulse blocks. The whole AXY-N sequence is enfolded by two $\frac{\pi}{2}$-pulses, the laser initialisation, and the readout. The effective pulse blocks are denoted by (b) X and (c) Y, where each block itself consists of five π-pulses with individual phase δ in the rotating frame of reference. The free evolution time between the π-pulses is τ_c, whereas the first and last free evolution time of one block is given by τ_d. To increase the order of the AXY sequence, the entire AXY-block can be repeated N-times.

The *Fourier amplitude* A is a parameter, which determines the signal strength dependent on the ratio of the free evolution times τ_c and τ_d. It is given by

$$\pi A = 2 + 4\cos\left(\frac{\pi\tau_c}{2\tau_c + \tau_d}\right) - 4\cos\left(\frac{\pi\tau_c}{4\tau_c + 2\tau_d}\right). \tag{3.17}$$

As shown in Fig. 3.14, its maximum value (~ 0.63) is reached for very short times τ_c, compared to τ_d. Yet, if for higher order measurements the signal strength is to strong and leads to a signal overshoot, it allows to tune down the signal strength with simultaneously keeping the high frequency resolution.

To determine the Fourier amplitude of a resonance, the sensing duration τ_{DD} for the specific signal is kept constant and the ratio τ_c/τ_d is varied. The resulting signal follows a sinusoidal behaviour

$$T(f_1) \propto \cos(0.25 f_1 A_x T) = \cos(0.25 f_1 A_x N \tau_{DD}), \tag{3.18}$$

with f_1 the first harmonic of the Fourier amplitude and A_x the x-part of the spin-coupling.

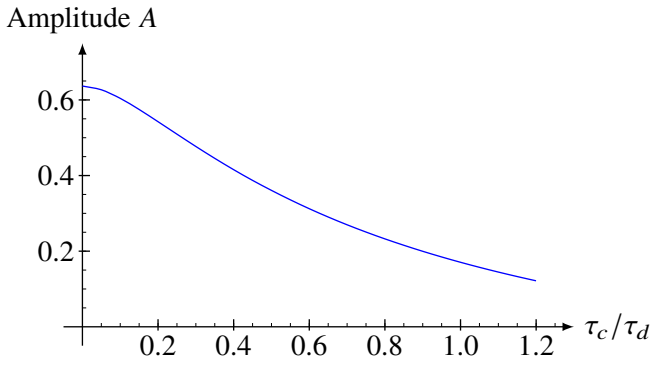

Figure 3.14: Fourier amplitude of the AXY-N sequence. Its maximum value ~ 0.63 is reached for very short times τ_c, compared to τ_d, and it converges asymptotically to zero for very long times τ_c. Overall, the Fourier amplitude is an adjustment parameter for signal detection.

Another way to determine the Fourier amplitude is by variation of the AXY order (*order sweep*). To do so, the sensing duration τ_{DD} for the specific signal is kept constant and the order N is increased. Due to the reduction of the signal linewidth for higher orders, it is important to ensure the position of the resonance precisely. As for the free evolution time ratio, the signal follows the sinusoidal behaviour of Eq. 3.18.
Additionally to the Fourier amplitude, the order sweep gives information about the order dependency of the signal. Thus, two parameters of the signal strength can be determined using this measurement. Nevertheless, due to the required accuracy of the resonance position, it is much more feasible to use the ratio as variable than the order (more closely discussed in Sec. 5.3.2).

Randomisation of Pulse Phases

Up to now, perfect delta-peak shaped pulses with no phase errors have been assumed. However, due to finite time for the state transition and also the arising imperfections in signal manipulation, this is experimentally not achievable.
The first modification of the used pulse schemes is done for each measurement which relies on free evolution times τ. Due to the finite driving strength via the MW field, the duration of the individual gates is on the order of 10 ns – 100 ns. This would lead to a biased measurement outcome, shifted by the proportionate effect of the gate durations. To prevent this error, the free evolution times are adjusted to the time from the middle of one pulse to the middle of the subsequent pulse.

Another modification is suggested by Wang et al.[68]. Their method not only reduces the impact of the finite pulse lengths, but also corrects the measurement outcome towards effects introduced by imperfections of the applied gates. Therefore, spurious signals as the higher order peaks of nuclear spins can be removed reliable.
The crucial point of this optimisation is to add a random phase ϕ_i to each pulse of a building

block of the DD sequence (see Fig. 3.15). It is important to note that each random phase has to be independent. This allows a reduction of the false signal accumulation effect. To further increase the effectiveness of the phase randomisation, the random phases of the building blocks can be refreshed after each run-through.

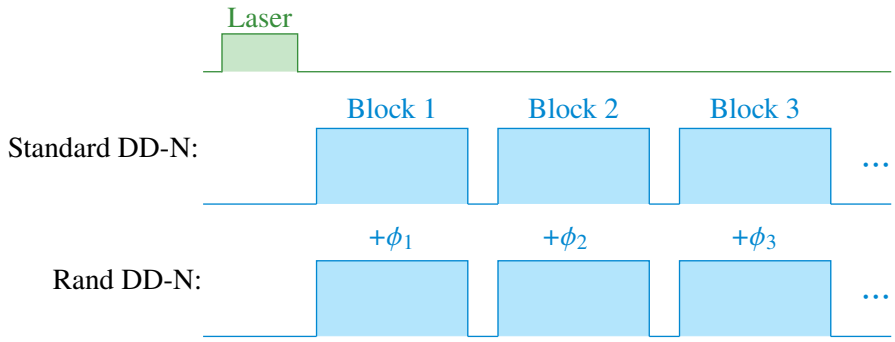

Figure 3.15: Comparison of a standard DD and a randomised phase DD sequence. Each of the N individual DD-blocks gets a random phase ϕ_i added to each pulse of the specific block.

3.3 Coherent Control of External Electron Spins

In the course of this chapter, a variety of experimental protocols to measure signals of spins in the proximity of the NV centre have been developed. Yet, all those protocols solely focus on the manipulation of the NV centre, allowing to decouple it from certain type of noise and detect specific resonant signals. As discussed in Sec. 3.2.2, this decoupling leads to a cancellation of spin signals as the shown effect of the oscillation suppression due to the refocus pulse in the Hahn-echo against the prominent oscillations in the Ramsey measurement (comparison of Fig. 3.9b and Fig. 3.10b).

In contrast to the advantage of increasing the coherence time by those DD sequences, the suppression of spin signals like the resonance of proximal electron spins is a significant downside for EPR measurements. To overcome this obstacle, an additional manipulation of the addressed, none-NV electron spin state can be done and, thus, the signal of those spins can be recovered selectively.

In this work, the electron spin of the NV is always assumed to be part of the system and is going to be called the *NV spin*. In contrast, when speaking about electron spins, only additional or external spins are considered.

3.3.1 Double Electron-Electron Resonance (DEER)

An overall grouping of measurements which contain the manipulation of more than a single electron spin and their interaction happens under the synonymous used names **Double Electron-Electron Resonance** (DEER) and **Pulsed ELectron-electron DOuble Resonance** (PELDOR). To be able to work with electron spins, it is important to perform preliminary measurements to determine the manipulation parameters similar to those, performed on the NV spin. Yet, since

those additional electron spins are not optically addressable, the readout of the effect of their manipulation is done with the help of the NV centre. This can be done due to the coupling of both spins. If for example the electron spin state is flipped simultaneously to the NV spin in the Hahn-echo sequence (Fig. 3.10a), the effect of the phase cancellation of the NV centre during the second free evolution time holds still true for all effects constant in time, except the signal of the flipped electron spin [69].

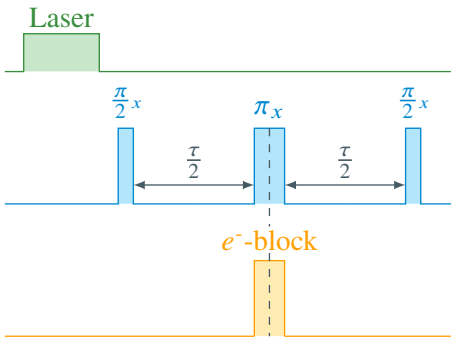

Figure 3.16: Schematic DEER measurement sequence. The NV manipulation (blue) is similar to the Hahn-echo, but the free evolution times $\frac{\tau}{2}$ are kept constant and chosen to be resonant to the coupling strength of the addressed electron spin. The second manipulation scheme (orange) is addressing the additional electron spins and is timed such that its symmetrically in the middle of the Hahn-echo.

In the general measurement scheme, as shown in Fig. 3.16, the microwave manipulation of the electron spin is simultaneous to the π-gate on the NV spin. This is done to achieve two equivalent (symmetrical) sensing durations with the NV centre. Thus, for a resonant pulse on the electron spin, the coherence of the NV gets lost and the effect of the electron spin manipulation can be determined from the fluorescence signal of the NV centre.
Following the phase calculation of Eq. 3.10, a π-flip of the electron spin state would lead to an additional sign-change of the interaction and thus,

$$\varphi(\tau) = 2\pi\gamma_e \left[\int_0^{\tau/2} B_{e^-}(t)\,\mathrm{d}t + \int_{\tau/2}^{\tau} B_{e^-}(t)\,\mathrm{d}t \right]. \tag{3.19}$$

According to the direction selectivity of the Hahn-echo (S^z interaction component), the field $B_{e^-}(t)$ acting on the NV spin can be approximated by the coupling of the electron spin to the NV (Eq. 2.34). This also holds true due to the big energy difference of the ZFS and Zeeman effect to the dipolar coupling between the spins. This leads to the effective field $B = A\ S^z$, with the abbreviation $A = d\left(1 - 3\cos^2\zeta\right)$.
Finally, the gathered phase of the NV centre after the DEER measurement is given by

$$\varphi(\tau) = 2\pi\gamma_e A\ S^z \tau. \tag{3.20}$$

Electron Spin Resonance

In order to perform electron spin manipulations, the first step is to determine the electron spin resonance frequency ν_{e^-}. Therefore, the DEER sequence is applied for a range of frequencies

(orange pulse line in Fig. 3.16) around the expected resonance frequency. To do so, there are three parameters which have to be estimated preliminary: the resonance frequency, the gate duration, and the free evolution time of the Hahn-echo.
The first estimation has to be done for the resonance frequency. As described in Sec. 2.3.2, the level splitting of a spin-$\frac{1}{2}$ system is given by $E = g_e \mu_B B_0$ (Eq. 2.14). Thus, the frequency is expected around $\nu_{e^-} = 2.8 \frac{\mathrm{MHz}}{\mathrm{G}} B_0$.
For the second estimation, the gate duration for the maximal contrast, the Rabi period of the electron spin has to be approximated. Therefore, the type of those spins plays a crucial role. If the addressed spin is a $S = 1$ system, the Rabi period is on the same order as the NV Rabi period. But for electron spins, which are $S = 1/2$ systems, this does not hold true. A common method to determine the spin quantum number in EPR measurements, is to compare the Rabi periods for known and unknown systems[70]. Even so that the NV is a $S = 1$ system, and thus, with three energy levels described in a 3×3 space, the high energy mismatch of the transitions leads to a treatment in an effective 2×2 subspaces. Those subspaces are spanned by either the $m_s = 0$ and $m_s = -1$, or the $m_s = 0$ and $m_s = +1$ states. Due to the normalisation, the transition matrix elements for the NV have a magnitude of $1/\sqrt{2}$, whereas the proximal electron spins as $S = 1/2$ systems have a magnitude of $1/2$. Therefore, the Rabi period of the electron spins can be calculated from a known NV Rabi period as

$$\Omega_{e^-} = \frac{\Omega_{\mathrm{NV}}}{\sqrt{2}}. \tag{3.21}$$

It is important to note, that the same driving strength has to be assumed for both manipulations, but due to the experimental imperfections in signal generation, amplification, and transmission, only an approximation can be guaranteed.
The last estimation is about the free evolution time of the Hahn-echo. This parameter is dependent on the dipolar coupling of the spins and due to the unknown distance and orientation only a vague guess is possible. For a coupling of around some hundreds of kHz, the interaction time should be on the order of some µs. Yet, as long as the interaction time is long enough to ensure the ability to transfer energy and not to long to still see contrast in the NV measurement, this parameter is not so crucial.

Similar to the ODMR and pulsed ODMR measurement (Sec. 3.1.2 and Sec. 3.2.1), a Lorentzian lineshape (Eq. 3.2) is expected with the resonance frequency as expectation value and the linewidth dependent on the power-broadening effect (see measurement Sec. 5.2.1).

Electron Spin Rabi Frequency

After the determination of the resonance frequency, the Rabi period Ω_{e^-} of the electron spins can be determined precisely. As already discussed, Eq. 3.21 gives an estimation for an idealised system, but mainly due to the non-linear frequency-dependent amplification of the amplifier and the imperfect antenna for the microwave guidance (see chapter 4), the Rabi period can deviate

from the expected value.
To measure the Rabi period, the DEER sequence is used with the proper resonance frequency and a variation of the pulse duration of the electron spin manipulation (orange pulse line in Fig. 3.16, measurement shown in Sec. 5.2.2).
The outcome is similar to the Rabi oscillations discussed in Sec. 3.1.3. As an effect of the symmetric sequence and the resulting acquired phase, the measurement is independent on the initial state of the electron spin and the Rabi period can be calculated by using Eq. 3.3.

DEER Lifetime

To determine the exact impact of a precise electron spin flip onto the NV spin state, the DEER sequence as shown in Fig. 3.17 is measured.

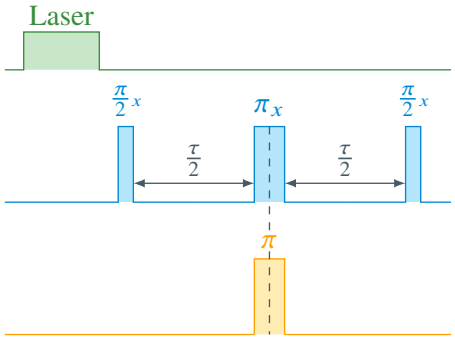

Figure 3.17: Schematic DEER measurement sequence. The NV manipulation (blue) is similar to the Hahn-echo with a variation of the free evolution times $\frac{\tau}{2}$. The second manipulation scheme (orange) is addressing the additional electron spins with a π-pulse on their respective frequency.

If a single electron spin is addressed by the π-pulse, the expected result would be an exponential decay with a single modulation frequency corresponding to the dipolar coupling (Eq. 3.20) of the NV to the electron. For more than one spin coupled to the NV and addressed by the microwave manipulation, the created field of the n electron spins is of the form

$$B = \sum_n A_n \, S_n^z, \tag{3.22}$$

and, thus, the dipolar coupling can not be inferred by a single measurement. To be able to reconstruct the individual couplings for more than one electron spin, a multitude of DEER measurements has to be performed. Hereof, each DEER measurement has to be performed with a different orientation of the magnetic field and, consequently, a variation of the n dipolar coupling factors A_i, with $i \in (1, ..., n)$.

There exist many different approaches based on Hahn-echo like DEER measurements with a simultaneous electron-spin π-pulse[69,71,72], a variation of the electron-spin π-pulse timing[73–75], and also an increasing number of π-pulses in the Hahn-echo of the NV centre manipulation[76,77].

Those DEER lifetime measurements can also be pushed to the point of performing XY-N[17] or AXY-N type sequences with simultaneous π-pulses on the electron spin frequency for each individual pulse of the NV sequence.
All those DEER measurements are constructed to be more selective in the measured interaction and to have a higher frequency resolution for the couplings compared to the normal Hahn-DEER. Since all those sequences rely on the same decoupling mechanisms, they are limited in their maximal sensing duration and, thus, their frequency detection range. This limitation is given by the T_2-time of the utilised NV centre, which is usually on the order of 5 µs − 70 µs.

3.3.2 Correlation DEER protocol

Another DEER approach is based on a sensing scheme with a limitation by the T_1-time of the NV, thus, increasing the maximal free evolution time of the sensing blocks by up to two orders of magnitude. Compared to the up to now discussed DEER measurements, this allows to work also with shallow NVs as sensors, regardless of their truncated T_2 time due to the surface induced noise.
The NV sequence part is based on two Hahn-echo like blocks separated by an additional free evolution time τ' (blue pulse line in Fig. 3.18)[78]. With this sequence, the phase accumulation of the two bordering pulse blocks can be compared, thus allowing to detect variations in the signals the NV is exposed to during the free evolution time τ'.
Nevertheless, to detect the signal of electron spins, the sequence has to be complemented by an additional manipulation of the proximal electron spins (orange pulse line in Fig. 3.18)[16].

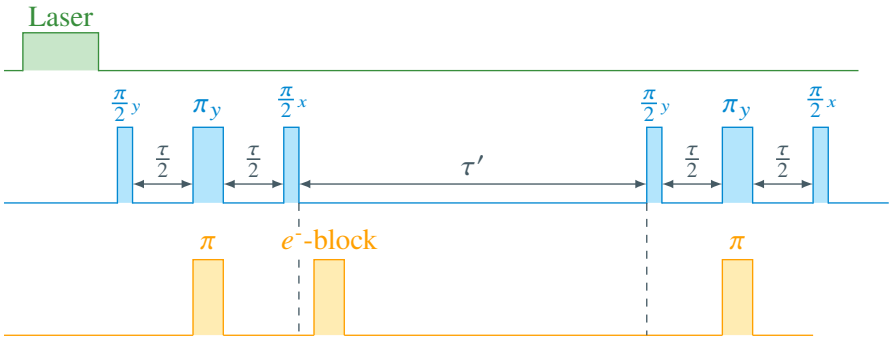

Figure 3.18: Schematic correlation DEER measurement sequence. The NV manipulation (blue) consists of two Hahn-echo like pulse blocks, separated by a free evolution time τ'. The second manipulation scheme (orange) is addressing the additional electron spins with π-pulses simultaneous to the NV π-pulses and with different sequences in between the free evolution time τ'.

The MW manipulation block of the proximal electron spins during the free evolution time τ' can be any presented sequence for electron spin manipulation as the Rabi oscillations (Sec. 3.1.3) or the coherence-time measurements (Sec. 3.2.2).
The free evolution times of the two NV manipulation blocks is working as a selection rule for the coupling strength of the measured electron spin signal[16] with the strength indirectly proportional to the probe times $\tau = \tau/2 + \tau/2$.

4 Experimental Setup

With the previous chapters introducing the physical model, the measurement theory, and the general result interpretation, this chapter is dedicated to the necessary setup used in the performed sensing experiments.
The entire setup consists of many individual parts, which can be grouped into two higher-level assemblies:
First of all is the confocal microscope, used for the all-optical excitation and readout of the NV spin state. Secondly, there is the wiring and control of the components used for the MW generation and MW control, the peripheral devices, and the temperature control of the sample chamber.

4.1 Confocal Microscope for NV Sensing Experiments

The first assembly is the confocal microscope which is placed on an air-damped optical table to reduce mechanical vibrations. The schematics of the home-build confocal microscope setup is shown in Fig. 4.1. A detailed part list, containing information about the specifications and manufacturers is provided in chapter 9.

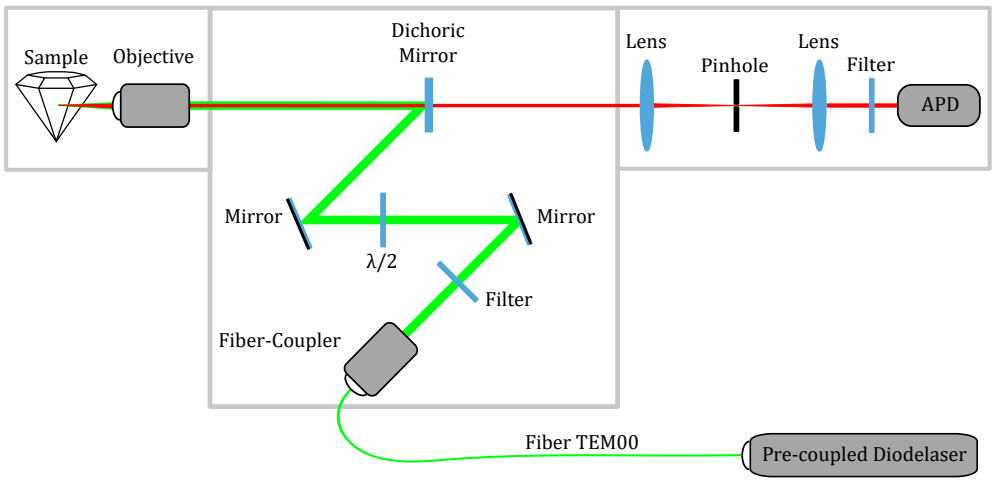

Figure 4.1: Schematic build up of the home-build, room temperature confocal microscope. All the optical parts are placed on an air-damped optical table to decouple from mechanical vibrations. The optical pathway is placed in three separate optical cardboard housings to reduce temperature oscillations, dust deposition, and interfering light.

Laser

As laser source, a pre-coupled laser-diode system '*iBeam Smart*' from *Toptica Photonics* with a wavelength of $\lambda = 519\,\text{nm}$ is used.
This laser-diode can be directly operated in pulsed mode, with an external **Transistor–Transistor Logic** (TTL) signal as trigger. The switching between the lasing states is done via its '*digital in*' port and allows to switch with a frequency of up to 250 MHz and a rise- and fall-time of below 1.5 ns. Additionally to its internal stabilisation and to ensure its temperature stability even further, the laser-diode is placed on a passive heat-sink, which is attached to the optical table to increase the energy flow. The location of the laser on the optical table is chosen such, that it is well separated from the sample, thus reducing unwanted heat transfer.
From there on, the laser is guided by the single-mode optical fibre into the first housing of the setup. Additionally to the guidance, the optical fibre guarantees a 'cleaning' of the laser mode due to the Gaussian TEM_{00} mode being the only transmitted mode.

Excitation Module

In the first housing part, the preparation of the laser light for the optical excitation is done.
First of all, a bandpass filter with central wavelength $\lambda_{\text{central}} = 520\,\text{nm}$ and FWHM $\Delta\lambda = 40\,\text{nm}$

cleans up unwanted fibre fluorescence and reduces the interfering light, not emitted by the laser-diode. As a second component, a $\lambda/2$-plate is placed on a home-build, remote controlled rotational stage. As described in Sec. 3.1.1, the waveplate is used to rotate the laser light polarisation to match the NV axis and, hence, maximise the excitation rate. To be able to rotate the laser polarisation and match the four possible NV lattice orientations automatically, an *Arduino* controlled rotation stage, driven by a *stepper motor* is implemented (further details about the rotation stage are given in chapter 9). Two additional mirrors are placed in the beam path to guide the laser beam onto a dichroic mirror, which is coated to transmit the red fluorescence signal of the NV into the detection path and to reflect the green laser light into the sample chamber.
Instead of the dichroic mirror, a beam-sampler was used in the beginning of the performed experiments. Despite its lower index of reflection of the green laser light, as well as its lower index of transmission of the red fluorescence signal, the beam-sampler was advantageous due to the strong back-reflex signal. The back-reflex image of the sample surface allows to visually focus the objective onto the desired area of the sample. Yet, due to the cleaner wavefront after the reflection and transmission and the higher corresponding indices, the beam-sampler got exchanged by a dichoric-mirror. This increased the counting signal and at the same time allowed to decrease the used laser power by one order of magnitude.

Sample Module

In the sample chamber, a 100× immersion-oil objective from *Nikon* with a numerical aperture of $NA = 1.45$ is focusing the laser light onto the diamond to excite the NV. The same objective is also used to collimate the emitted red fluorescence of the measured NV centre. As depicted in Fig. 4.2, the diamond is placed on top of a cover glass and the objective focuses the laser beam through both, the cover glass and the diamond, onto the NVs, which are located close to the upper surface of the diamond sample. For this reason, *00*-type cover glasses are used, which means that they are 60 µm − 80 µm thin. Therefore, the objectives working distance of 130 µm allows a diamond thickness of up to 50 µm.

Detection Module

The last part of the beam path is the detection path. From the objective on, the emitted red fluorescence is transmitted through the dichroic mirror into the housing of the detection setup. This housing is used to decrease the stray light and background light and hereby reduces the background signal to the dark count rate of the detector. In the housing, a $2f$ lens setup is used to focus the fluorescence signal through a 25 µm pinhole and an additional longpass filter onto the **Avalanche Photo-Diode** (APD). Here, the pinhole removes all signals not aligned with the focal plane and the 650 nm longpass filter reduces the false-transmitted laser light by the dirchoic mirror even further. The here used APD is a single photon counting device from *Excelitas Technologies* with an efficiency of 80 %, a short dead time of typically 22 ns, and a dark count rate of less than 80 photons per second.

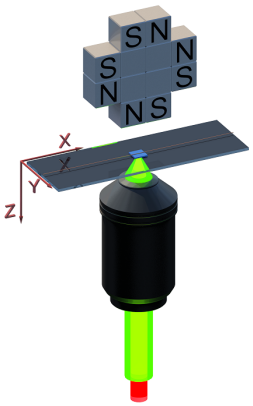

Figure 4.2: Schematic, illustrating the experimental geometry of the confocal head of the microscope. The diamond is placed on top of a cover-slide (or sample holder). The objective focuses the laser beam (green beam) through both, the cover glass and the diamond, onto the upper surface, where the NVs are located. The same path is used for the fluorescence detection (red beam). Above the optical part, an assembly of neodymium magnets is used to apply a magnetic field to the sample. Image taken from Weggler et al.[79]

4.2 Control of the Experimental Setup

As control of the entire experiment, a computer is the central device, operating all setup components. For the control of the setup, the processing of the measurement data, and the entire visualisation the modular python software *QuDi*[80] is used. This software allows to control all measurement parts and makes running the experiment due to its intuitive user interface straight forward.
The wiring diagram schematising the interconnections of the setup, as shown in Fig. 4.3 and can be subdivided into three parts:
As a first part, there is the combination of the MW sources and the MW control. This part is also responsible for the timing of the experiment. The second part contains the whole peripheral devices, used for the preparation, initialisation, and readout of the experiment. The temperature control is the third and final part, ensuring a stable environment of the sample during the measurement.

4.2.1 Microwave Source and Control for the MW-Field Generation

For the MW generation, different devices can be used. The first MW source is the *SMIQ*, a vector signal generator from *Rohde & Schwarz*. This device is used for the continuous ODMR measurements (Sec. 3.1.2), where the internal frequency switching triggers the time intervals for the signal summation of the fluorescence signal counting. Therefore, a defined frequency range is ramped through with a defined frequency step size, and time continuous signal summation.
The second MW source is an **Arbitrary Waveform Generator** (AWG) from *Tektronix*, which is used for all other, pulse-based measurements. Due to its high time-resolution of up to 50 G Samples/s with an amplitude resolution of up to 10 Bit and the large memory, it allows to output the entire pulse sequences as a single waveform file, thus, ensuring the rotating frame of

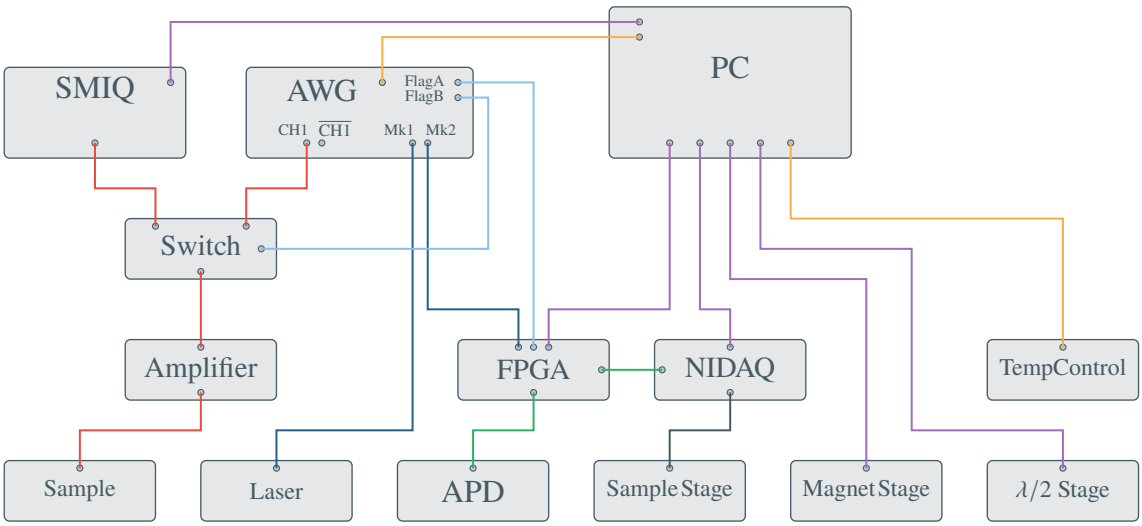

Figure 4.3: Schematic wiring diagram of the experimental setup. The type of connection is color-coded, where: red is the MW path, dark blue are the *Markers* (logical level 1.4 V), light blue are the *Flags* (used like Markers as logical level), green is the counter-signal, purple are the **Universal Serial Bus** (USB)-connections for the control, and orange are Ethernet connections for the communication.

reference during the measurement with a high vertical resolution.

Besides its function as a MW generator, the AWG is also used for switching and timing of the experiment. Therefore, the two markers *Mk1* and *Mk2*, as well as the additional Flags *FlagA* and *FlagB* are used as digital triggers, allowing to control the external devices timed with respect to the waveform. The first marker is used for the digital switching of the laser diode and the second marker synchronises the gated counting of the APD signal with respect to the NV response and laser signal. The first Flag outputs a pulse of ~ 40 ns to signal the end of one sequence run-through and thus, the start of another repetition. Due to this reason, it is called the *sequence trigger*. To switch the MW-switch between the two inputs, the second Flag is set to logical low (through-put of SMIQ signal) or logical high (through-put of AWG signal).
To reach the required MW power, the signal is amplified with an external amplifier from *Amplifier Research (ar)* and afterwards routed to the sample holder. The sample holder is depicted in Fig. 4.4 and is home-build from a circuit board to approximately match the wire impedance of 50 Ω.

A 25 μm thin copper wire is used as MW antenna and is stretched between the two contacts of the circuit board across the surface of the diamond sample. To reduce reflections of the MW signal behind the sample, the final termination is done by a MW sink, attenuating the MW signal.

4.2.2 Peripheral Devices of the Setup Control

The second part of the wiring diagram of the experimental setup, the peripheral devices, are used to prepare the necessary parameters, and initialise and readout the NV.

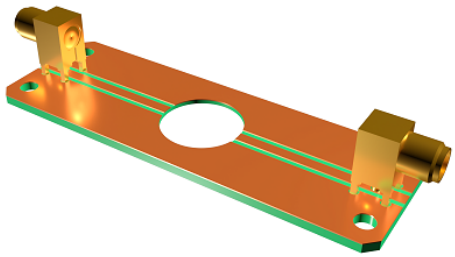

Figure 4.4: Top-view of the home-build sample holder, build from a circuit board with the impedance matching approximately the wire impedance of 50 Ω. The diamond sample is placed onto a cover glass overlapping the circular opening in the middle, which is framed by a larger opening from the bottom, allowing the objective to be moved across (from below) the sample surface.

Signal Counting

For the readout of the fluorescence signal, the APD is used as counting device. Since two different types of readout are required in the experiment, the count signal from the APD is copied by the **Field-Programmable Gate Array** (FPGA) and then looped through to the *NI-DAQ*, a data acquisition and I/O module from *National Instruments*.
The copied count signal is used for continuous counting with the NI-DAQ. It is called *slow counting* and is used for the non-time-critical counting, employed in the *Counter* of QuDi, showing the direct response of the APD, the scanning of the fluorescence image, and the ODMR measurement.
Besides the copying of the signal, the FPGA is also used for the *fast counting*. This fast counting is used for the time-critical readout of the pulsed measurement sequences, where the counting of the fluorescence signal detected by the APD is timed with respect to the laser initialisation of the NV centre and the delay timing introduced by the interconnection paths.
Additional to the fast counting, the FPGA measures a time-trace of the signal and generates a histogram of the count data with respect to the measurement sequence. This gated counting is triggered by the sequence trigger and the count signal is transferred to the computer afterwards.

Sample Positioning

To be able to remotely adjust the scanning position for the measurement all over the diamond sample and at the same time allow a precise positioning of the NVs in the confocal volume of the objective, the sample holder is mounted onto two translational stages (from *Physical Instruments*) which are stacked on top of each other.
For a coarse positioning of the sample, a piezo linear-motor stage with a range of 25 mm × 25 mm is used. This stage is connected via its controller directly to the computer and steered by the provided *PI MikroMove* software.

For the fine positioning, a XYZ-stage with a range of 70 µm × 70 µm × 50 µm is build into the setup. The analogue driving of the stage is achieved by the digital-to-analogue I/O module of the NI-DAQ and the control is done by QuDi and used for the confocal scanning and tracking of the individual NVs. Accordingly, high resolution confocal images of the sample in the X-Y plane (Fig. 4.5a) and the X-Z (or Y-Z) plane (Fig. 4.5b) can be recorded.

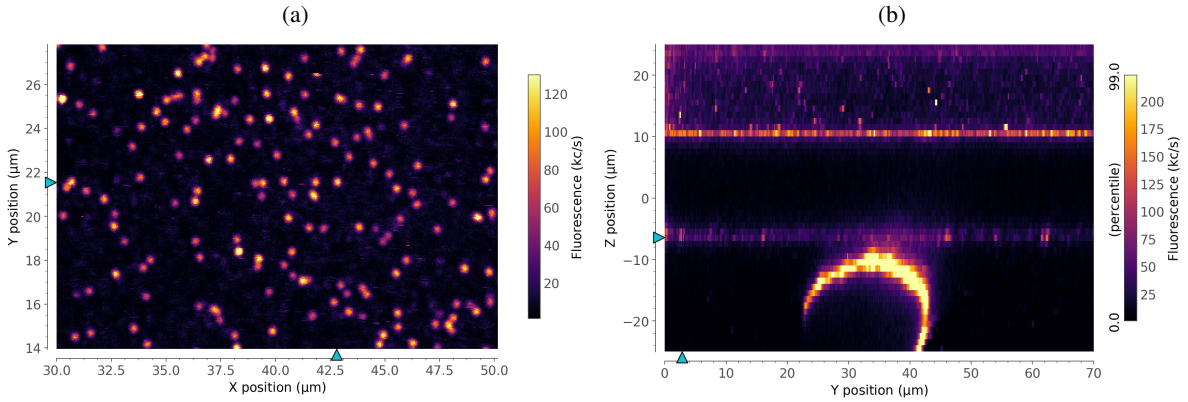

Figure 4.5: Exemplary high resolution confocal images of the sample showing NVs in the diffraction-limit of the confocal microscope. The yellow spots are NVs and the background is shown in purple. (a) X-Y plane of the diamond sample. (b) X-Z plane displayed upside down. The area below the NVs (below ~ −6 µm) is the immersion oil with small particles scattering the light and above the NVs is the diamond without implantation sites. Due to the height of the diamond plate (~ 35 µm), the cover slide and the used fixation (above ~ 10 µm) can be seen as well as the used MW wire.

Magnetic Field Generation

For the magnetic field application, a cross-shaped assembly build out of 12 neodymium permanent magnets, as depicted in Fig. 4.2, is used. This magnet configuration allows to create a magnetic field of more than 1500 G at the diamond surface.

As the orientational alignment and amplitude adjust-ability of the applied magnetic field are two of the most crucial capabilities for the experimental setup, the motorised stages for the magnet positioning are chosen accordingly. The exact positioning is achieved by a combination of three translational stages (*PI LS110*) with a resolution of 0.2 µm and one rotational stage (*PI PRS110*) with a resolution of 0.002° from *Physical Instruments*. Additionally and due to the high repeatability of $< \pm 1$ µm for the translational stages and $< \pm 0.01°$ for the rotational stage, it is also guaranteed to be able to reapply a previously determined field with a very high accuracy.

The control of the magnet stages can be done automatically via the QuDi software or manually by the provided PI MikroMove software.

Laser Light Preparation

For the control of the laser pulses, the marker of the AWG is connected to the '*digital in*' port of the laser-diode, thus allowing an exact timing of the switching between the lasing states of the diode (more closely described in Sec. 4.1). Additionally, the laser is connected to the computer via a serial communication port to be able to control the output power of the laser-diode and to enable the communication with the device via console commands.
For the $\lambda/2$ stage control, the Arduino is connected via USB to the computer. This allows a direct communication via a console. For the sake of simplicity, a python hardware module for this rotational stage is added to the QuDi software. But since no graphical user interface is added yet, the communication has to be done via the QuDi console.

4.2.3 Temperature Control of the Sample Chamber

Due to the temperature dependency of the NVs' energy levels[81], already small fluctuations of the ambient temperature can lead to a detectable shift of the transition frequencies of the NV centre. Combining this effect with the thermal elongation of the used materials in the sample chamber (sample holder circuit board, cover-slide subsurface below the diamond), temperature instabilities would decrease the signal contrast during longer measurements drastically. Yet, by refocusing the position of the NV in the confocal volume and re-determination of the transition frequency, those effects could be corrected for. This would still lead to a prolonging of the actual measurement duration due to the sequence regeneration and upload without increasing the SNR.
To preserve the setup against such thermal instabilities, the sample chamber which contains the positioning stages of the sample, as well as the positioning stages of the magnets, is placed in an insulated box. To increase the thermal stability, a **Proportional-Integral-Derivative** (PID) controller in combination with two 155 W thermoelectric coolers is used for a feedback-loop control of the temperature in the sample chamber.
With this controlled environment, a temperature of (292.15 ± 0.05) K is achieved. With this stability, stable measurements continuing over many hours can be performed with almost no loss of signal contrast.

5 Towards EPR Measurements - Characterisation of Interaction Effects

Combining the theory, the measurement protocol, and the experimental build-up, the previous chapters give a general map of the measurements employed for the performed EPR experiments. These basic modules are used as a foundation for the determination of dipolar couplings between spins. In more detail: those spins shall ultimately be electron spin labels attached to specific sites of biological molecules to determine the conformation and conformational changes of the molecule via the performed EPR experiments.

In the following, the utilised diamond samples with their implanted NV centres and their specific characteristics are presented. To reveal the resonance and the interaction of proximal electron spins different EPR measurements are performed, proving the existence of electron spins coupled to the measured NVs. To rule out the misinterpretation of those obtained resonances the depth of the NV-containing layer, their interaction with nuclear spins, and the dipolar couplings are investigated as well.

All measurements are performed as N-times repeated read-outs of the NV spin states ($N \sim 10^6 ... 10^7$), averaging the effect of the performed gates and the sensed interactions. The number of repetitions N is here dependent on the signal strength and contrast relative to the NV signal. In order to qualitatively compare similar measurements, N is kept constant in these cases.

5.1 Sample Classification

As presented in Sec. 4.1, an objective focuses the laser through a cover glass and through the diamond onto the NVs, located on the top surface of the diamond. This setup-order ensures a clean diamond surface as an environment for biomolecules and their optimal buffer solution in later experiments. Additionally, a surface treatment and cleaning is enabled without performing the whole preparation anew.
In order to create NVs suitable for electron spin dipolar coupling measurements, the diamond creation and modification, as well as the nitrogen implantation has to be performed in a specific manner ensuring the necessary parameters for the performed measurements. Therefore, this section gives an overview of the employed diamond samples and preparation steps required previous to the experiment. Since the intrinsic *lifetime* parameter of NVs can be used as a reference of their environmental interactions, it is used in the final part of this section to measure the modification impact of the applied diamond preparation.

5.1.1 Nitrogen Vacancy Implantation Parameters

Due to the long optical pathway through the cover glass and the diamond, in combination with the finite working distance of the objective, the diamond itself has to be a very thin slice. Therefore, the used diamond samples are laser-cut and polished to a thickness of 35 µm – 50 µm. This allows to move the objectives' focus along the optical z direction into different depths close to the diamond surface.
For the NV creation, the ion-beam implantation technique (Sec. 2.2.1) was chosen and circular spots with a diameter of roughly 100 µm are implanted. With this technique it is possible to offer a range of different environments within the same sample, thus, establishing a big variety of NV parameters to choose from for all further sensing experiments.

The experiment requires different coherence times of the NVs with the required duration dependent on the distance between the electron spins in the NV detection volume. Being more precise, a lower bound for the required NV coherence time can be calculated using Eq. 3.15: For electron spins with a dipolar interaction of 500 kHz, a coherence time of only around 2 µs is necessary, while for a electron spin coupling of 100 kHz, the coherence time has to exceed already 10 µs. This can be offered by using various implantation depths, determined by the utilised implantation energy during the ion-beam implantation. To enable a proficient coherence time tuning, NVs were implanted at three depth ranges using three different implantation energies: [82]

- 1.5 keV for very shallow NVs (less than 7 nm),
- 2.5 keV for NVs with a depth of less than 10 nm, and
- 5 keV for deeper NVs (up to 20 nm).

As a downside, the depth does not only influence the coherence time, but also the interaction strength between NVs and spins located on the diamond surface. This makes the choice of depth

a trade-off between optimal sensing duration and dipolar coupling strengths strong enough to be detectable. Yet, for both samples, only the spots with an implantation energy of 2.5 keV are characterised in this work. Thus, all values here can be compared independently of their expected implantation depth.
Another parameter of the implantation is the dose of nitrogen ions used, which defines the number of created NVs per implantation area. For the here performed measurements, it is the goal to measure with well separated specimen, but at the same time sense signals on as much area on the surface above the NV layer as possible. To achieve both, a variation of implantation doses ranging from $10^9 \frac{N^+}{cm^2}$ up to $10^{12} \frac{N^+}{cm^2}$ is used.

5.1.2 Diamond Sample Identification

The first experiments are performed with sample *T001-1*, a 35 µm thin diamond slice with nine different implantation spots, where each spot has a specific density and depth, as shown in the sample map (Fig. 5.1a).

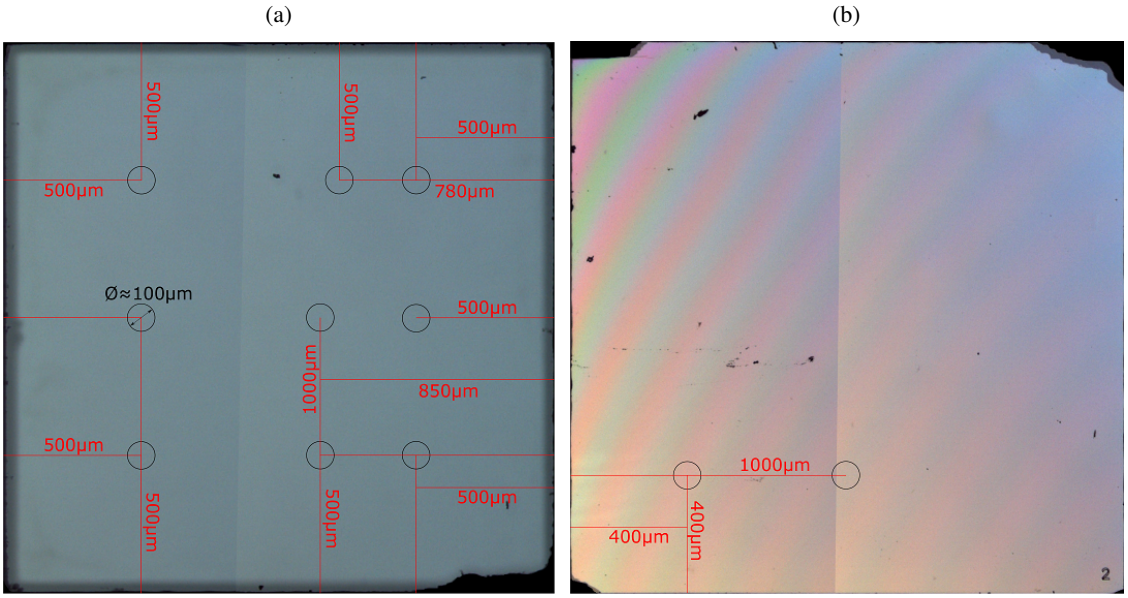

Figure 5.1: Images of the 2 mm × 2 mm diamond samples, recorded using a light-optical microscope with 10× magnification. The implantation spots are marked with a grid. (a) Sample T001-1 with NVs implanted into the diamond with natural abundance of ^{13}C. (b) Sample T002-2 with the NVs implanted into a roughly 100 nm thick layer of highly purified ^{12}C. The implantations were done by *Johannes Lang* and the overgrowth was done by *Christian Osterkamp*, both from the *Institute of Quantum Optics from Ulm University*.

During the measurement of various NMR experiments with sample T001-1, it got evident how the natural abundance of ^{13}C and the thus arising nuclear spin signal disturbed the signals of interest. Therefore, a second sample, *T002-2* with the same height and two implantation spots was prepared (Fig. 5.1b). The main difference between those two samples is the additional overgrowth

on sample T002-2 with a 100 nm thick layer of enriched ^{12}C atoms, done before the implantation step. This nuclear spin-free layer is isolating the subsequently implanted NVs from the nuclear spins of the seed diamond plate and serves as a calm environment, decreasing interfering signals from the surrounding area.
To be able to select from a number of known NVs, the areas in the implantations spots have been characterised and defined in maps, allowing to measure the same sites repeatedly. For both samples up to 50 different NVs have been measured and named by their sample, their implantation spot, the measurement map, and the number of measured site. After the implementation of the $\lambda/2$-rotation stage, the polarisation axis was incorporated in the nomenclature as well.

5.1.3 Diamond Surface Preparation

Prior to the actual measurements and in order to remove dirt accumulations from the diamond surface, the diamond samples have be cleaned thoroughly. For this surface cleaning, the diamond sample is boiled at 130 °C in a three-acid mixture with equal volumes of concentrated sulphuric acid (H_2SO_4), nitric acid (HNO_3), and perchloric acid ($HClO_4$) for three hours. The oxidising effect of the acid cleaning also leads to the binding of oxygen radicals to the open bonds of the diamond surface, thus, introducing free electron spins in the proximity of the NVs, required in some of the performed measurements.
To verify that the measured interactions result from spins attached to the diamond surface, the same acid cleaning can be used to reset the locations of the surface radicals. After such a reset, signals from surface radicals would not show the same distance-dependent interactions twice in a row, whereas signals from electron spins located in the diamond lattice would still be the same.

5.1.4 Coherence Time Measurements

In both samples, only NVs containing ^{14}N as their own nuclear spin were measured. For these, the transition frequencies of the $I_n = 0$ dips have been used exclusively for the NV manipulation and magnetic field determination (as described in the vector magnetometry Sec. 2.4.5 and field vector reconstruction in chapter 6).
In all performed Ramsey measurements (Sec. 3.2.2) the interaction with proximal ^{13}C nuclear spins are visible. Those measurements also show the shell-dependent coupling strength, as mentioned in the ODMR introduction in Sec. 3.1.2 and as documented by Dréau et al.[51]. Nevertheless, only a single NV was measured with a ^{13}C-interaction strong enough to be effecting the ODMR measurement directly (discussed in more detail in Sec. 5.3.2).
Overall, the enriched layer of ^{12}C atop of sample T002-2 led to a lower degree of this effect, due to the reduced number of carbon nuclear spins in the NV layer. Yet, this also proofs the fact, that no ^{13}C-free layer was achieved by the overgrowth.

As it serves as a frequency limit for the electron spin sensing experiments, the T_2-time measured by the Hahn-echo (Sec. 3.2.2) is more important for the performed DEER experiments. To compare the effect of the overgrowth on the second sample, we subdivided the T_2-time into three categories:

- $T_2 < 10\,\mu s$ as short,
- $T_2 = 10\,\mu s - 30\,\mu s$ as normal, and
- $T_2 > 30\,\mu s$ as long coherence time.

A sample comparison of the T_2-time regime fractions, depicted in Tab. 5.1, shows a clear prolonging effect for the overgrown sample T002-2. The resulting overall higher amount of NVs with a normal or long T_2-time of sample T002-2 offers a bigger selection for all further sensing experiments of weak dipolar couplings.

Table 5.1: T_2-time subdivision into three categories. There were 24 different NVs measured for sample T001-1 and 22 NVs for sample T002-2. Only values for comparable magnetic field amplitudes were taken into consideration.

	T001-1	T002-2
short	~ 33%	~ 9%
normal	~ 46%	~ 55%
long	~ 21%	~ 36%

Out of the specimen with a long T_2-time, almost one third of the measured NVs in sample T002-2 showed a coherence time of more than 50 µs, corresponding to detectable frequencies of down to a few kHz. Hereof, the most prolonged coherence time is $T_2 = (79.8 \pm 3.4)\,\mu s$.
Therefore, the overgrown sample T002-2 offers a high number of possible sites for EPR measurements with a large range of detectable frequencies and thus serves as a suitable sample for this work.

5.2 DEER Experiments

After the discussion of the parameters influencing the performed sensing measurements, as for instance the depth and lifetime of a NV centre in the used samples, the detection of electron spins using different EPR measurements has to be done.

A first and fast proof of the existence of electron spins coupled to the NV centre are the DEER experiments, as described in the spin dynamics section (Sec. 3.3.1). They directly indicate resonances of proximal electron spins, yet, they do not indicate the individual source type of the measured signal. This means that either electron spins in the diamond lattice or atop of the diamond surface can be the origin of the measured signal. Here, the signal from atop of the

diamond sample would be generated by spin radicals, or for more advanced measurements spin labels attached to biomolecules or ionised atoms of the biomolecule additionally deposited atop of the diamond surface. On the contrary, the internal electron spin signals are most likely to be generated by *P1* centres: isolated nitrogen atoms, substituting single carbon atoms of the diamond lattice, or other NV-like impurities embedded into the diamond.
Nevertheless, there are various methods to distinguish between the different sources of signals. Firstly, to determine whether the signal origin is internal or external, the diamond can be acid-cleaned after the measurements to reset the external electron spin positions and, thus, only lead to a variation of the induced signal from external electron spins. Secondly, to differ between the remaining signals of the internal sources, the optical spectra of the measured confocal spot can be investigated. This leads to an accurate determination of the vacancy specimen or leaves only the P1 centre as source of the signal.
With all methods for the differentiation of the signal origin available, the next step is to investigate the manipulation and interaction of electron spins coupled to a NV centre. Therefore, the following section discusses the performed DEER resonance-, Rabi-, and coupling-measurements in more detail.

5.2.1 DEER Transition Frequency

Proving the existence of proximal electron spins and at the same time identifying the proper resonance – or transition – frequency for all further manipulations, the electron spin resonance measurements are performed (described in Sec. 3.3.1).

An exemplary result measured at $B = (466.4 \pm 0.5)\,\mathrm{G}$ is shown in Fig. 5.2, where both measurements were performed following the pulse sequence depicted in Fig. 3.16. Yet, for the first measurement, the pp amplitude of the electron spin manipulation π-pulse is set to $V_{\mathrm{pp}} = 0\,\mathrm{mV}$, whereas the second part is measured with the amplitude set to $V_{\mathrm{pp}} = 125\,\mathrm{mV}$. For the applied magnetic field, the resonance frequency of a spin-$\frac{1}{2}$ system is expected to be around $\nu_{\mathrm{expect}} = (1306.2 \pm 1.4)\,\mathrm{MHz}$.
As the measurements show, this signal is detectable only with a non-zero pulse amplitude and around the expected transition frequency. The overall lineshape can be described by a Lorentzian function, similar to the effect for the NV (Sec. 3.1.2), and shows a power dependent width, narrowing with decreasing MW amplitude as determined in Tab. 5.2. For the lowest values of the amplitude a convergence of the peak width to a lower bound is identifiable. This lower bound can arise due to the shorter lifetime of the additional electron spins compared to the long lifetime of the measured NV centres.
Another way to review the source of the signal is the determination of the gyromagnetic ratio by variation of the applied magnetic field amplitude. In Fig. 5.3, the resonance frequencies show a linear dependency corresponding to Eq. 2.14 with the expected gyromagnetic ratio $\gamma_e = g_e \mu_b = 2.8\,\frac{\mathrm{MHz}}{\mathrm{G}}$ for free electron spins.

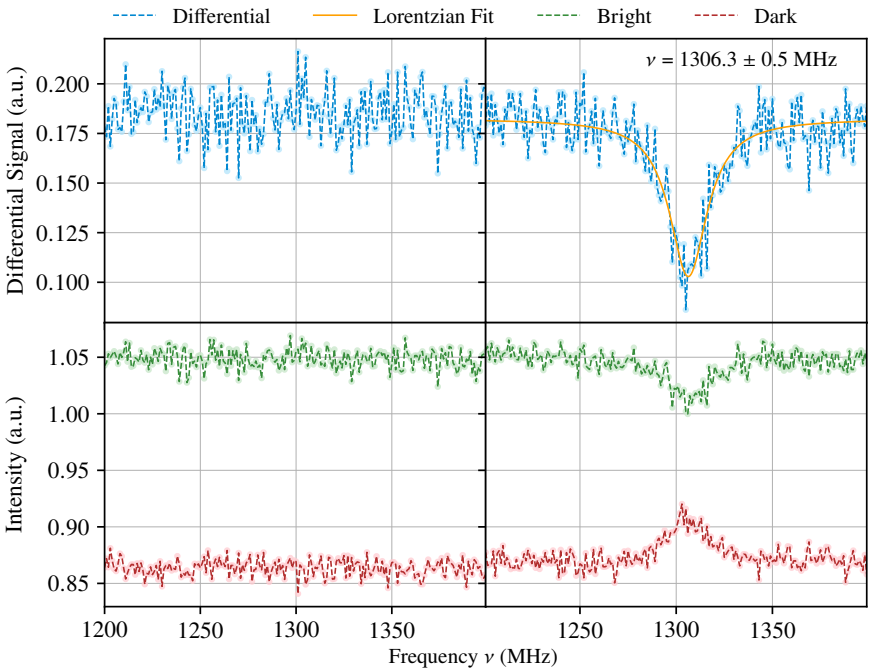

Figure 5.2: Measurement of the DEER resonance transition frequency for the determination of the external electron spin signal. The readout of the NV spin state is performed for the bright (green) and dark (red) state spin projection at the end of the measurement. For the evaluation with a Lorentzian fit function (orange), the differential signal (blue) is used, calculated as the difference between both readouts (bright and dark state signals). These measurements on *T001-1 Spot9 Map03 NV04* were performed at $B = (466.4 \pm 0.5)\,\mathrm{G}$ with **Peak-to-Peak** (pp) signal amplitudes $V_{\mathrm{pp}} = 0\,\mathrm{mV}$ (left) and $V_{\mathrm{pp}} = 125\,\mathrm{mV}$ (right) at the AWG. The MW-pulse duration for the electron spin manipulation was set to $\tau_{e^-} = 65\,\mathrm{ns}$.

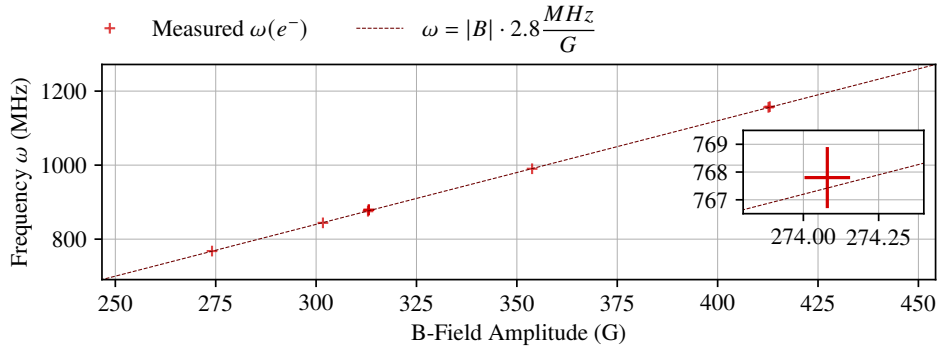

Figure 5.3: Measurement of the external electron spin resonance frequency. The theoretical frequency (dashed dark red) for the spin-$\frac{1}{2}$ transition is calculated according to Eq. 2.14. Due to its negligible magnitude compared to the frequency range, the error of the calculated point is shown exemplary for the first point in the magnified section of the graph and waived in the overall view.

Table 5.2: Resonance frequencies determined by the DEER resonance detection of the spin-$\frac{1}{2}$ system including the power-dependent peak width. These measurements on *T002-2 Spot2 Map01 NV03* are performed at $B \sim 242\,\mathrm{G}$. Due to the frequency range of the amplifier used in this experiment, the resonance peak width measured at this magnetic field amplitude exceeds the linearity specifications, allowing no exact statement about the resonance position and FWHM measured with 125 mV.

V_{pp} in mV	ν in MHz	FWHM in MHz
125		> 100
62.5	676.8 ± 0.8	76.0 ± 6.0
31.25	675.6 ± 0.6	34.0 ± 4.0
15.6	676.3 ± 0.7	25.9 ± 2.7
7.8	676.9 ± 0.5	16.6 ± 1.7
4.0	677.5 ± 0.5	14.0 ± 1.4
2.0	677.3 ± 0.5	15.6 ± 1.9

5.2.2 DEER Rabi

Up to this point, the duration of the MW-pulse is only a rough estimation and therefore, the next measurement is the determination of the electron spin Rabi-period. This allows to measure using time-wise matching pulses on the additional electron spins, increasing the contrast to its maximum. This measurement also follows the sequence shown in Fig. 3.16, however, in contrast to the DEER resonance, the frequency is kept constant while the duration of the MW-pulse is varied.
The results in Fig. 5.4 show the electron spin Rabi oscillations for four different MW amplitudes. With an increasing MW amplitude a proportional increase of the Rabi-frequency Ω is observed, where the overall proportion of the frequency-to-power dependency in this measurement is given by 0.9813 ± 0.0005.

According to Sec. 3.3.1 and Schweiger and Jeschke[70], the relation between the Rabi-period of a spin-1 and a spin-$\frac{1}{2}$ system should differ by a factor of $\frac{1}{\sqrt{2}} \sim 0.707$. This estimation is done for ideal systems without a frequency-dependent signal generation and amplification. For the here performed experiments the imperfection of the amplifier flatness and signal transmission is visible in all measurements. For example, shown in Fig. 5.4, the Rabi-period ratio of the two systems is given by ~ 0.937 and thus higher than expected.

Overall, by combination of the DEER preliminary measurements, it got evident that the transition frequency can be directly calculated from the applied magnetic field amplitude. However, the Rabi-period needs to be determined for each amplitude and field anew to correct for technical imperfections.

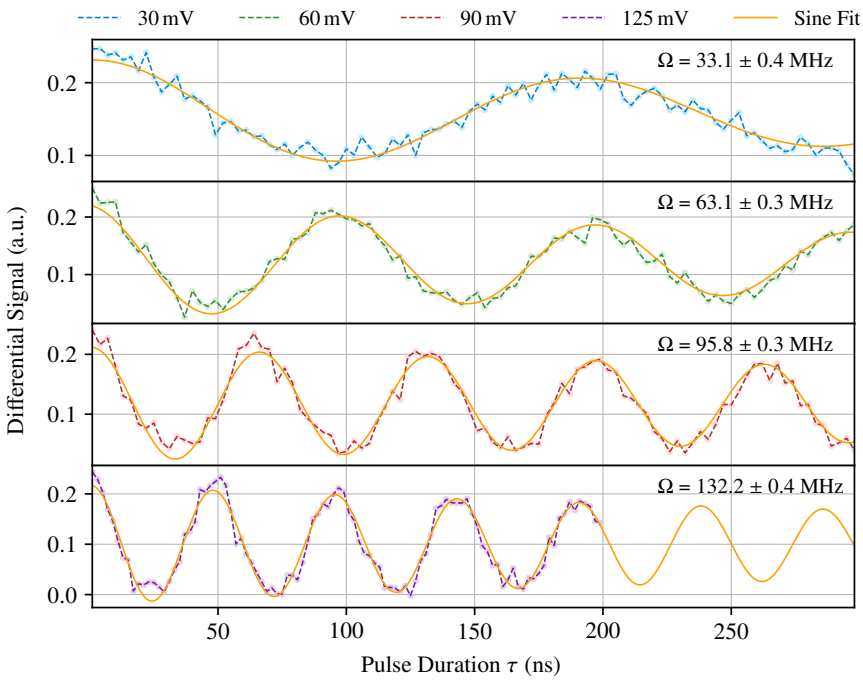

Figure 5.4: Four DEER Rabi measurements with different AWG pp amplitudes for the determination of the electron spin response. Changing the AWG pp amplitude shows a direct proportionality between the driving strength and the Rabi period Ω. These measurements were performed on *T001-1 Spot9 Map04 NV04* at $B = (441.0 \pm 0.5)$ G with the NV parameters $(V_{\mathrm{pp}}, T_{\mathrm{Rabi}}) = (125\,\mathrm{mV},\ 50.8\,\mathrm{ns})$.

5.2.3 DEER Coupling

After the determination of the proper parameters for the electron spin resonance frequency π-pulse, DEER measurements can be performed as described in the spin dynamic and methodology chapter (Sec. 3.3.1).

In Fig. 5.5, the additional MW-pulse in the DEER measurement leads to a distinct variation of the originally obtained Hahn-echo signal. The first and striking change of this example is the appearance of one pre-eminent oscillation, and secondly, a reduction of the NV spin coherence time. Nevertheless, the reconstruction of the decay required at least two frequencies to describe the variation of the signal entirely. Following the description of the dipolar coupling in Eq. 3.22, this behaviour can be explained by one strongly coupled electron spin in close proximity to the NV centre and a spin bath farther apart and, thus, the superposition of many slightly varied frequencies.

Those two effects are apparent for all performed DEER measurements, yet most of the measured NVs show a faster decay more prominently than a strongly pronounced oscillation frequency. This can be explained by the statistical distribution of the radicals on the diamond surface. As stated by Sushkov et al.[16], they measured a lower limit of approximately 5 nm as spacing between surface spins for a diamond similarly treated as the here measured sample. Thus, for an expected NV-depth of roughly 5 nm, only radicals straight above the NV centre itself can be suspected to show such a strong coupling. Already a lateral shift of 1 nm of the surface electrons leads to

a bisection of the expected distance difference between the NV and the most proximal surface electrons.
As another result of the DEER and the Hahn-echo signal comparison, the free evolution time τ of the maximally measured contrast can be obtained. This parameter is used in further DEER measurements to maximise and normalise the overall contrast, as for example used in the power dependent linewidth measurements shown in Tab. 5.2.

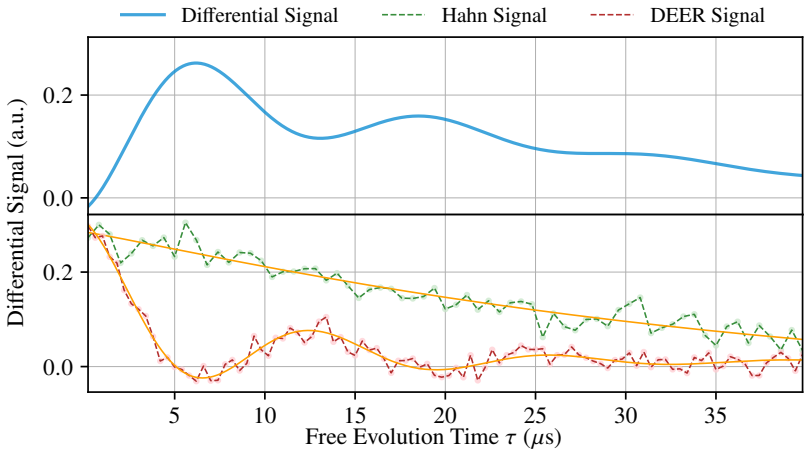

Figure 5.5: Comparison between the Hahn-echo and DEER measurement on *T001-1 Spot9 Map04 NV04* at $B \approx 440\,\mathrm{G}$. The free evolution time for the maximum contrast in the differential signal of both measurements is used for the highest contrast in following DEER measurements ($\tau = 6.2\,\mu\mathrm{s}$ for this measurement). It is visible that the lifetime of the NV is reduced by the second π-pulse (without additional pulse $T_2 = 26.11\,\mu\mathrm{s}$). Additionally, an oscillation with $\omega = (76 \pm 2)\,\mathrm{kHz}$ appears, most likely introduced by a single and strongly coupled electron spin, proximal to the NV.

According to the theory of the *position reconstruction of the quantum spin reporters*[16], a variation of the magnetic field leads to a variation of the dipolar-coupling between the NV and the surface radicals. This can be understood by reconsideration of the dipolar-coupling Hamiltonian between electron spins (Eq. 2.15 and Eq. 2.34). Here, the interaction of the spins i and j is dependent on two parameters: first, the inter-spin distance $\left|\boldsymbol{r_{ij}}\right|$ and, secondly, the angle θ_{ij} between the spin-connection vector $\boldsymbol{r_{ij}}$ and the magnetic field orientation. While the former parameter is a constant for bound surface radicals, the latter parameter can be controlled by an alteration of the magnetic field orientation.

In Fig. 5.6, a magnetic field orientation variation measurement for *T001-1 Spot9 Map05 NV02* is presented. The four different magnetic field orientations at $B \approx 441\,\mathrm{G}$ are calculated according to Balasubramanian et al.[49] and their effect on the NV coherence time is observed. For this specific site, the Hahn-echo yielded a spin-spin relaxation time of $T_2 = (15.1 \pm 1.8)\,\mu\mathrm{s}$ and by application of the additional electron spin flip, this value got reduced. For small misalignments of up to 8°, the coherence time got shortened by a factor of roughly 2.5, whereas for the highest misalignment of 11.8°, it even got reduced by a factor of almost 5.

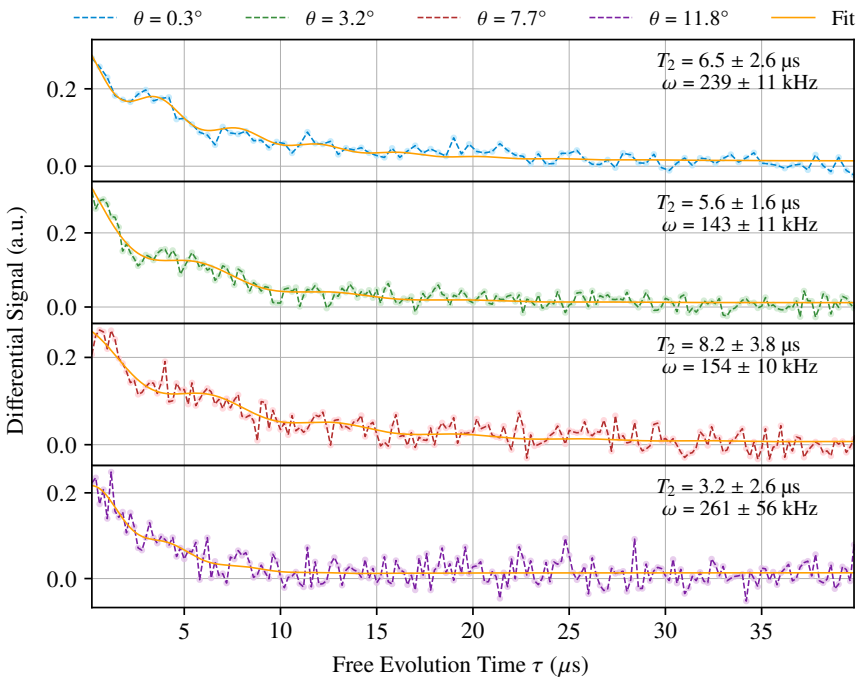

Figure 5.6: The DEER coupling measurement performed for four different magnetic field alignments with respect to the NV axis. Without the manipulation on the second frequency, the overall NV lifetime is (15.1 ± 1.8) µs. These results were measured on *T001-1 Spot9 Map05 NV02* at $B \approx 441$ G. The variation of the lifetime due to the additionally introduced interaction is visible in all four measurements. Furthermore, they show a slight variation in the visible coupling frequency.

In addition to the effect on the overall coherence time, different oscillation frequencies got visible. For the measurements with 3.2° and 7.7°, the oscillation frequencies are approximately 150 kHz while for the measurements with 0.3° and 11.8° misalignment, the prominent oscillation frequency is around 240 kHz.

Yet, a more detailed reconstruction for this set of data was impracticable. This got evident by a closer analysis of the magnetic field orientation and the resulting lack of information. The calculated angles θ of the misalignment between the NV principal axis and the magnetic field orientations are defined by the scalar product between the two directions. Under consideration of direction independence of those two vectors, the scalar product function is explicit only in two dimensions. However, the real space is three-dimensional, this results in a cone of possible magnetic field orientations around the NV axis (described and analysed in more detail in chapter 6). Concluding these measurements, the lack of information could be overcome by more measurements with different magnetic field misalignments or by a more detailed knowledge about the magnetic field orientation in the laboratory frame. Nevertheless, the former solution only holds true if the electron spins are located on a defined distance with respect to the diamond sample surface, as for example the depth of the NV for surface spins [16]. For the case of entirely unknown spatial coordinates of the electron spins, as it is present for biomolecules with attached spin labels

or radicalised internal atoms, only the knowledge about the three-dimensional magnetic field orientation allows to reconstruct the inter-spin distances.

5.2.4 DEER Correlation Measurements

As a proof of principle, the DEER correlation measurement is performed to measure Rabi oscillations on external electron spins. The result in Fig. 5.7a shows the possibility to coherently manipulate the electron spins in the free evolution time between the two sensing blocks of the sequence shown in Fig. 3.18.
In order to compare both electron spin Rabi measurements, they are performed on *T001-1 Spot9 MapX NV04* using the same MW amplitude of 50 mV for the electron spin manipulation (Fig. 5.7). Here, the two measurements are in good agreement and yielded a Rabi period of (35.2 ± 0.6) ns and (35.1 ± 0.4) ns respectively.

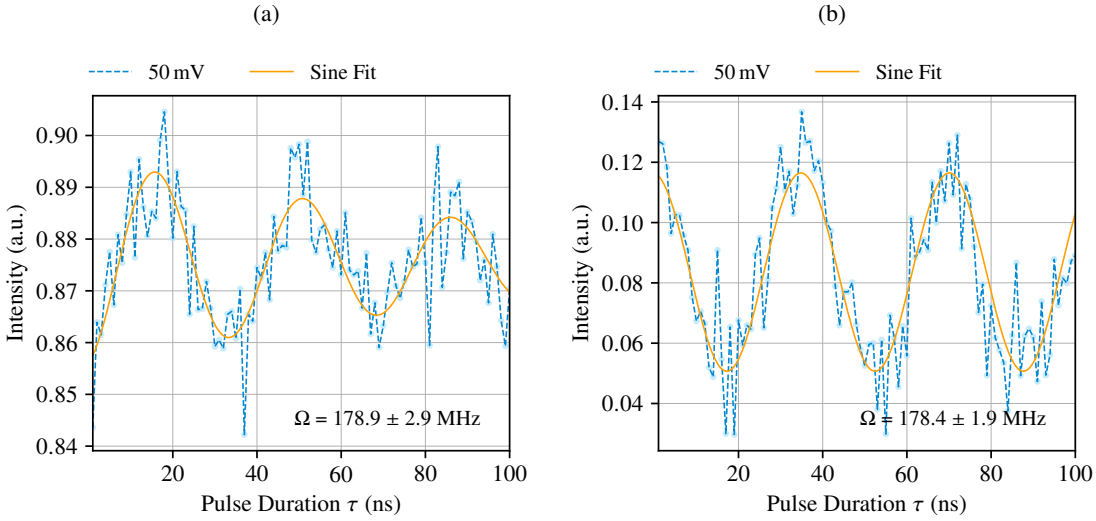

Figure 5.7: Rabi oscillations measured on the external electron spins with the (a) DEER correlation measurement and (b) the normal DEER Rabi measurement. These results were measured on *T001-1 Spot9 MapX NV04* at $B \approx 303$ G with a MW amplitude of 50 mV for the electron spin manipulation. The measured Rabi periods are in good agreement with (35.2 ± 0.6) ns and (35.1 ± 0.4) ns respectively.

This readout and manipulation scheme allows to overcome the T_2 limitation of the DEER measurement by keeping the NV in a pure state, limited by its T_1-time. Additionally, this sequence enables more complex sensing schemes than the DEER measurement. Due to the electron spin interaction block among the two Hahn-like sensing blocks, also schemes like Ramsey or Hahn-echos applied to the external electron spins are feasible. Therefore, not only the coupling of the NV with the additional electron spins, but also their individual couplings can be investigated.

5.3 Sensing of the NV Environment

Up to now, all presented DEER measurements ultimately rely on the manipulation of the external electron spins as mechanism for the signal detection. But as already presented in the section about the DD of the NV (Sec. 3.2.3), it is possible to sense proximal fields by the controlled modulation of the free evolution times of such DD sequences.
This alternative technique also allows to detect the dipolar coupling between identical external electron spins, even so their resonance frequencies are the same. Yet, not only signals originating from electron spins, but also signals due to nuclear spins can be detected. It is therefore necessary to be able to distinguish the type of spin, responsible for the obtained signal.
Here, the detectable signals are induced by the Larmor precession or the dipolar coupling of spins. As explained in the derivation of the spin dynamics (Sec. 2.3), those frequencies are dependent on the magnetic field, the inter-spin distance, and the spin types of the interaction.
For nuclear spins, the Larmor frequency is roughly three orders of magnitude smaller than for electron spins (comparison of the magnetic moments Eq. 2.13 and Eq. 2.16) and dependent on the amplitude of the magnetic field. In contrast, the dipolar interaction is dependent on the distance between the spins and the orientation of the magnetic field. As an estimation, those values can be calculated for typical parameters of the performed experiments. If the applied magnetic field amplitude is on the order of 200 G − 300 G, the Larmor frequencies for common nuclear spin species are on the order of a few hundred kHz up to some MHz (see also Tab. 2.2). At the same time, the dipolar interaction of electron spins, calculated according to Eq. 2.15 as

$$\begin{aligned} \nu_{\mathrm{dd}} &= g_e^2 \mu_{\mathrm{B}}^2 \frac{1}{4\pi\mu_0 h} \frac{3\cos^2\zeta - 1}{|r|^3} \\ &= 52.04\,\mathrm{GHz\AA}^3 \frac{f(\zeta)}{|r|^3}, \end{aligned} \tag{5.1}$$

is on the same range of frequencies (a few hundred kHz) for an electron inter-spin distance of 5 nm. Yet, by comparing measurements performed for a variation of the magnetic field amplitude while preserving a fixed orientation with measurements of a fixed magnetic field amplitude but a variation of the field orientation, the change of the signals clearly indicate their spin specie and interaction origin.

5.3.1 Depth Determination using DD Protocols

As a first prediction parameter and to estimate the coupling between the external electron spins and the NV, the depth of the NV can be determined. This parameter can also be used as a upper bound for their expected coupling strength.
According to Pham et al.[83], the depth of a shallow NV can be determined by its interaction with hydrogen nuclear spins contained in the immersion oil tipped atop of the diamond surface. They describe a technique, where the sensing volume dependent field created by the statistical

distribution of those nuclear spins gets analysed, and thus, the depth of the sensor can be determined.
In order to do so, the XY-N sequence (Sec. 3.2.3) with the sensing windows timed around the expected Larmor frequency of hydrogen nuclear spins, as well as the entire decay for the used order N has to be measured. With those two sets of data, the differential signal contrasts

$$F = \frac{I_{\text{bright}} - I_{\text{dark}}}{I_{\text{bright}} + I_{\text{dark}}}, \tag{5.2}$$

of both measurements can be determined, allowing to correct for noise arising from laser fluctuations. Afterwards, the signal of the interaction dip has to be normalised by dividing the data set by the decay of the whole measurement. The resulting dip in the normalised signal contrast $C(\tau)$ can be described by the magnetic field fluctuations B_{RMS} of the nuclear spins detected by the employed XY-N sequence and thus created filter function $K(N\tau)$:[83]

$$C(\tau) \approx \exp\left\{-\frac{2}{\pi^2}\gamma_e^2 B_{\text{RMS}}^2 K(N\tau)\right\}. \tag{5.3}$$

In Eq. 5.3, the NV depth dependency of the signal is included by the multiplier $B_{\text{RMS}}^2(d_{\text{NV}})$, describing the magnetic field fluctuations as

$$B_{\text{RMS}}^2 = \rho\left(\frac{\mu_0\hbar\gamma_n}{4\pi}\right)^2\left(\frac{5\pi}{96 d_{\text{NV}}^3}\right), \tag{5.4}$$

with ρ the particle density of the sensed immersion oil.
In the signal contrast function, the position and shape of the dip is mainly dependent on the hydrogen spin Larmor frequency ω_L and XY order N, entering the DD filter function

$$K(N\tau) \approx (N\tau)^2 \text{sinc}^2\left[\frac{N\tau}{2}\left(\omega_L - \frac{\pi}{\tau}\right)\right]. \tag{5.5}$$

If the finite lifetime T_2^* of the diffusing hydrogen nuclear spins is taken into account, Eq. 5.5 has to be varied and the assumed delta-like nuclear spin response has to be substituted by a Lorentzian shaped function (derivation and filter function given in Pham et al.[83]).
Nevertheless, this method and evaluation holds true only for a disturbance free system. For the in this work used diamond samples, proximal ^{13}C nuclear spins are detected at each measured site. Therefore, the randomisation of the pulse phases, as described in Sec. 3.2.3, has to be used to get rid of the overlapping signal and at the same time employ the presented method for the NV depth determination.
As shown in the depth measurement performed on *T001-1 Spot9 MapX1 NV03* at (315.9 ± 0.7) G (Fig. 5.8), the depth of the exemplary measured NV for an implantation energy of 2.5 keV was determined to be $d_{\text{NV}} = (5.5 \pm 0.1)$ nm. Yet, in the measurement of the entire decay, also the dip of carbon nuclear spins was visible at the expected Larmor frequency with the corresponding free evolution time of $\tau = 1.48\,\mu$s. In order to still be able to reconstruct the NV depth following Eq. 5.3, the carbon signal can either be subtracted by a signal deconvolution, or circumvented

by a proper measurement sequence definition sparing the time-steps around the carbon nuclear response, while later was done for this measurement.

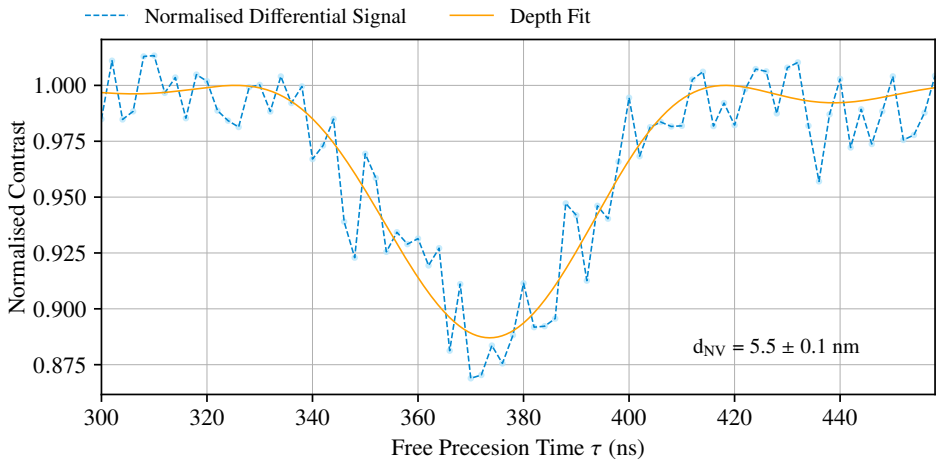

Figure 5.8: Depth determination measurement result for *T001-1 Spot9 MapX1 NV03* using the randomisation of the XY-N sequence with $N = 2$. The measurement was performed at (315.9 ± 0.7) G and yielded a depth of $d_{\mathrm{NV}} = (5.5 \pm 0.1)$ nm for this specific NV. The implantation energy used for *Spot9* was 2.5 keV.

Therefore, we are able to determine the depth of individual NV centres, independent of their coupling to secondary nuclear spin species, and hereby express a upper bound for the coupling strength to external electron spins.

5.3.2 Effects of Strongly Coupled Nuclear Spins

Since all diamond samples used in the here performed experiments contain carbon nuclear spins, it is necessary to investigate the effect of such spins onto the detection schemes employed for electron spin dipolar couplings. Out of these nuclear spins, strongly coupled ones can be used as an exemplary system, allowing to cross-correlate the various measurement methods and reconstruct the interaction redundantly.
In order to understand and extract these effects of a strongly coupled ^{13}C nuclear spin, measurements of *T002-2 Spot2 Map01 NV08* showing these effects are discussed in more detail.
For this NV, already the pulsed ODMR measurement, shown in Fig. 5.9a, contained an additional splitting of the three NV-^{14}N lines. This splitting is approximately 0.65 MHz and indicates a strongly coupled nuclear spin. While the spin-spin relaxation time is as long as $T_2 = (40.2 \pm 1.2)$ µs, the Ramsey measurement showed a multitude of different oscillation frequencies and a lifetime of $T_2^* = (1.97 \pm 0.10)$ µs (Fig. 5.9b).

In order to describe the system, the Hamiltonian containing the interaction of the NV with the nuclear spin has to be analysed. Following Eq. 2.32 for a single nuclear spin and according to Taminiau et al.[65], the system can be described using

$$\mathcal{H} = \omega_h \left(\cos\xi \, S_z I_z + \sin\xi \, S_z I_x\right) + \omega_{\mathrm{Larmor}} I_z, \tag{5.6}$$

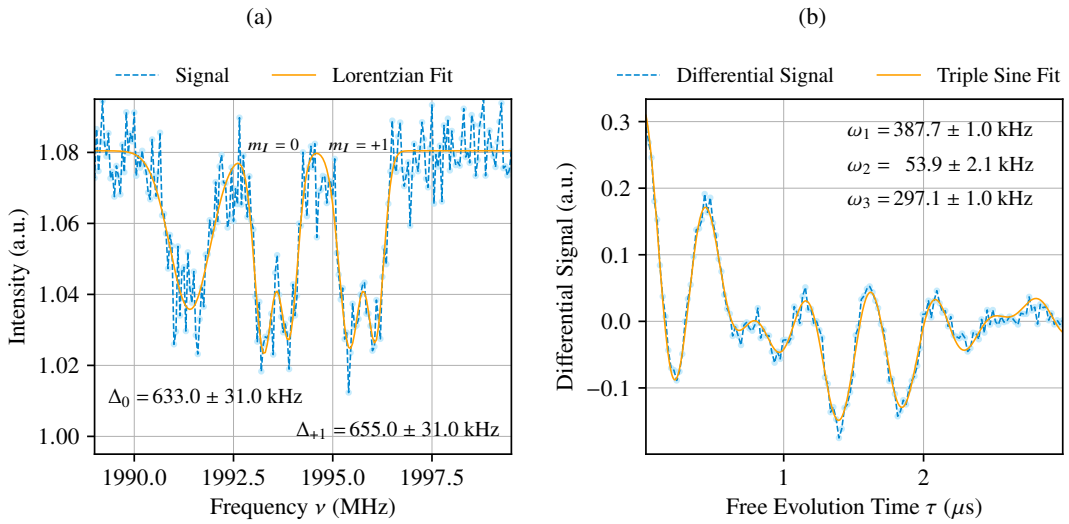

Figure 5.9: First measurements on *T002-2 Spot2 Map01 NV08* at $B \approx 310$ G. (a) Three NV resonance dips measured via pulsed ODMR with an additional splitting of roughly 0.65 MHz. (b) Ramsey measurement with at least three sine-functions required for a fit convergence. Both measurements indicate the strong coupling of a ^{13}C nuclear spin, located very close to the NV.

with the hyperfine coupling ω_h and the angle ξ between the two components, depicted in Fig. 5.10. Overall, the first part in Eq. 5.6 describes the interaction of the NV spin with the nuclear spin, whereas the second part arises due to the nuclear Zeeman effect only. This leads to an interaction, dependent on the $m_s = 0, \pm 1$ electron spin state of the NV.

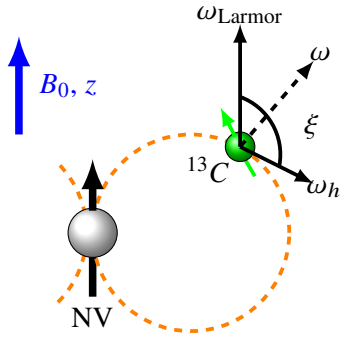

Figure 5.10: Schematic of the hyperfine coupling between the NV (grey) and a single ^{13}C nuclear spin (green). The effective precession ω is tilted away from the Larmor precession due to the effect of the proximal NV and the such arising hyperfine coupling. Based on Taminiau et al.[65].

As a next step and verification of the signal source, the AXY-N measurement was repeated for different magnetic field amplitudes and the magnetic field orientation aligned with respect to the NV axis.

As shown in Fig. 5.11, each measurement contains a signal at the expected Larmor frequency of a nuclear carbon spin $\omega_{^{13}C} = 1.0708\,|B|$ and a second peak with an additional offset. Yet, for a

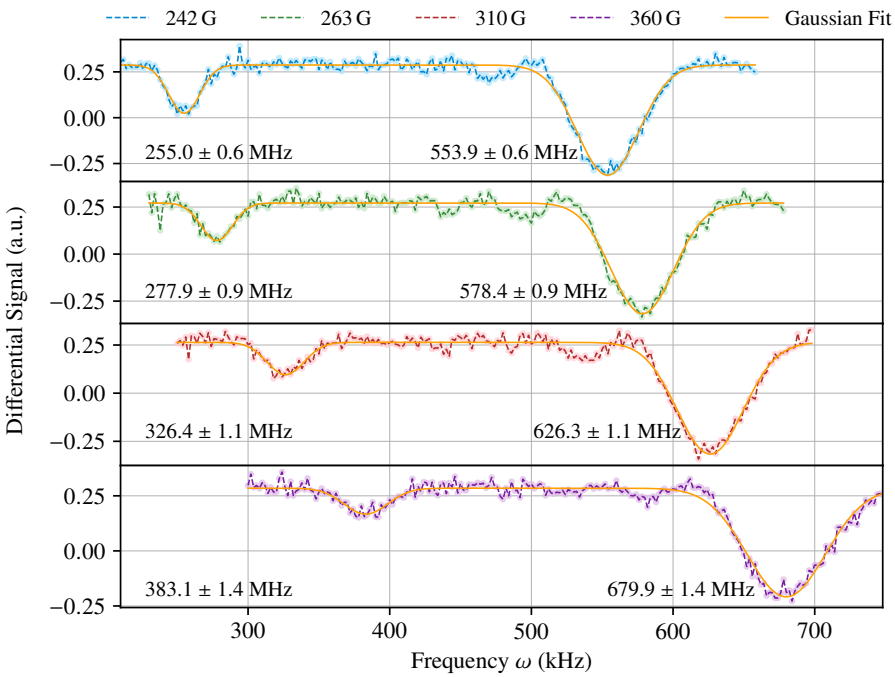

Figure 5.11: Measurement of the AXY-2 sequence on *T002-2 Spot2 Map01 NV08*: 1^{st} measurement at (241.6 ± 0.3) G, 2^{nd} measurement at (263.0 ± 0.3) G, 3^{rd} measurement at (310.2 ± 0.2) G, and 4^{th} measurement at (359.7 ± 0.2) G. The peaks at lower frequencies correspond to the Larmor frequency of a ^{13}C nuclear spin and the peaks at higher frequencies contain the parallel component of the hyperfine coupling between the nuclear spin and the NV.

variation of the magnetic field, this second peak shifts similarly as the Larmor frequency and can be explained by the additional I_z part of the Hamiltonian (Eq. 5.6). This signal follows

$$\widetilde{\omega} = \omega_{\text{Larmor}} \pm 0.5 A_z, \tag{5.7}$$

with the parallel hyperfine coupling component $A_z = \omega_h \cos\xi$ and the sign dependent on the sign of the NV electron spin state. According to Eq. 5.7, the first part of the hyperfine coupling between the proximal ^{13}C nuclear spin and the NV is given as $A_z = (589.0 \pm 1.6)$ kHz.
Following the description of the AXY-N measurement in Sec. 3.2.3, the perpendicular component of the hyperfine interaction can be measured using the order sweep, as well as the Fourier-amplitude sweep. The two results in Fig. 5.13 show the outcome for the resonance of the nuclear spin and both measurements are in good agreement with each other where the order sweep yields $A_x = (214.0 \pm 0.5)$ kHz and the Fourier-amplitude sweep yields $A_x = (221.9 \pm 1.6)$ kHz. Thus, the hyperfine coupling and the tilt angle ξ can be calculated according to

$$\frac{A_z}{\cos\xi} = \omega_h = \frac{A_x}{\sin\xi}, \tag{5.8}$$

as $\xi = ((20.64 \pm 0.20)°, (19.97 \pm 0.10)°)$ and, thus, $\omega_h = (628.1 \pm 1.5)$ kHz. This result is also consistent with the results obtained by the pODMR measurement, shown in Fig. 5.9a.

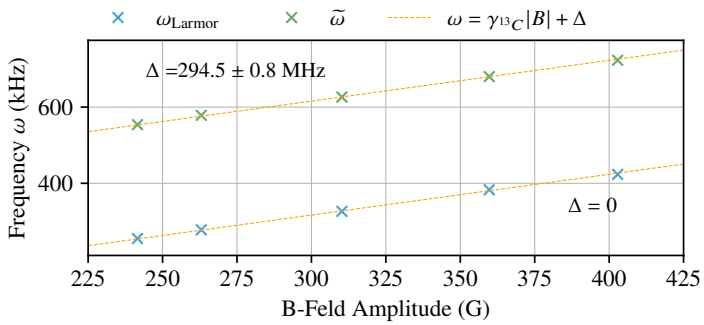

Figure 5.12: Analysis of the AXY-2 signals, shown in Fig. 5.11. One peak follows the nuclear Zeeman effect $\omega_{\text{Larmor}} = \gamma_{^{13}C}\,|B|$ and the second one is shifted due to the I_z-part of the hyperfine interaction as $\widetilde{\omega} = \omega_{\text{Larmor}} \pm \frac{A_z}{2}$.

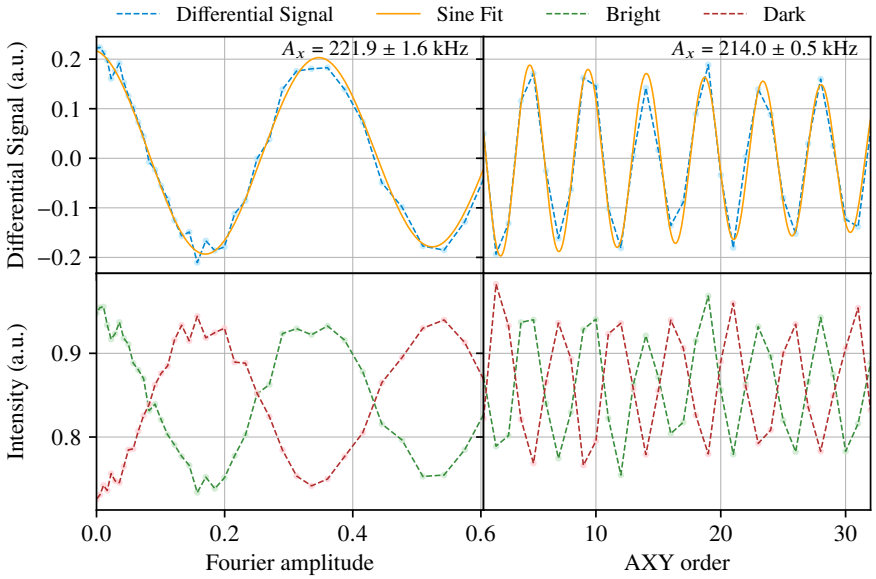

Figure 5.13: Fourier sweep (left) and order sweep (right) measurement result for *T002-2 Spot2 Map01 NV08* at ($|B| = (312.9 \pm 0.3)$ G, $\theta = (7.2 \pm 0.3)°$). The directional coupling component corresponding to Eq. 3.18 is determined as $A_x = (221.9 \pm 1.6)$ kHz (Fourier sweep) and $A_x = (214.0 \pm 0.5)$ kHz (order sweep). This interaction is introduced by a strongly coupled ^{13}C nuclear spin, only a few Å apart from the NV.

The here calculated hyperfine interaction of the nuclear spin hints a location in either the *M* or *N* shell of the ^{13}C families, introduced by Dréau et al.[51]. The offset from the here expected hyperfine coupling (N-shell: 560 kHz, M-shell: 700 kHz) can possibly be explained by an additional spin, coupled to the system. This would also explain the number of different frequencies in the Ramsey measurement. Overall, this result is corresponding to a inter-spin distance of the ^{13}C nuclear spin and NV spin of less than 0.6 nm.

Concluding, this section allows to differ between the various signals of nuclear spins and electron spins measured using DD sequences. Thus, the next step is the determination of electron spin couplings using the AXY measurement.

5.3.3 Electron Spin Dipolar Coupling Measurements

In Fig. 5.14, an exemplary AXY-N measurement of *T002-2 Spot2 Map01 NV17* at roughly 315 G is shown. For this site, the measurements have been performed for four different magnetic field alignments with respect to the NV centre principal axis. The misalignment angles θ are given between 4° and 7°. Since this particular NV shows no interaction with a proximal carbon nuclear spin with the expected Larmor frequency around $\omega_{\text{Larmor}} \sim 335\,\text{kHz}$, it is chosen for the further investigation of the AXY-N signal.

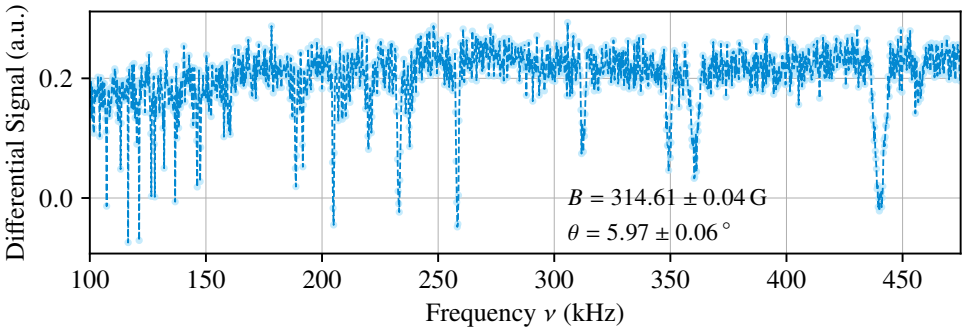

Figure 5.14: AXY-N measurement of *T002-2 Spot2 Map01 NV17*. This exemplary measurement at roughly 315 G is performed for frequencies from 100 kHz up to 475 kHz and using the order $N = 2$. Shown is the differential signal of the bright and dark state read-out. Multiple dips are visible, yet no variation of their positions was detected for a changed magnetic field alignment.

The measurement in Fig. 5.14 shows multiple sharp and narrow dips for lower frequencies (< 225 kHz) and some broader dips for higher frequencies (> 225 kHz). Nevertheless, no peak coincides with Larmor frequencies of nuclear spin species usually found in the diamond lattice. According to Eq. 2.7, a variation of the magnetic field amplitude would result in a change of the nuclear spin Larmor frequency. Yet, for the performed variation of the magnetic field amplitude, the measured signals stayed constant and, therefore, the resonances are supposed to be connected to electron spins in the diamond lattice or atop of the diamond surface. The multitude of narrow dips at low frequencies could possibly arise due to interference of many electron spin interactions and the used AXY-N sequence.

Although a variation of the signal is expected for electron spin dipolar couplings conducted by the magnetic field orientation, this effect was not visible for the four performed misalignment measurements.
As depicted in Fig. 5.15, the small change of less than 1° in the alignment for the individual AXY-N measurement results for most angles ζ in a variation of around 1 % (angular part of Eq. 5.1). This value translates for an expected inter-electron spin distance $|\boldsymbol{r}| \approx 5\,\text{nm}$ into a change of the dipolar coupling of roughly 4 kHz at the maxima. Only around the two zero-crossings of the dipolar coupling, a higher percentage variation is expected. Yet, the dipolar coupling of this

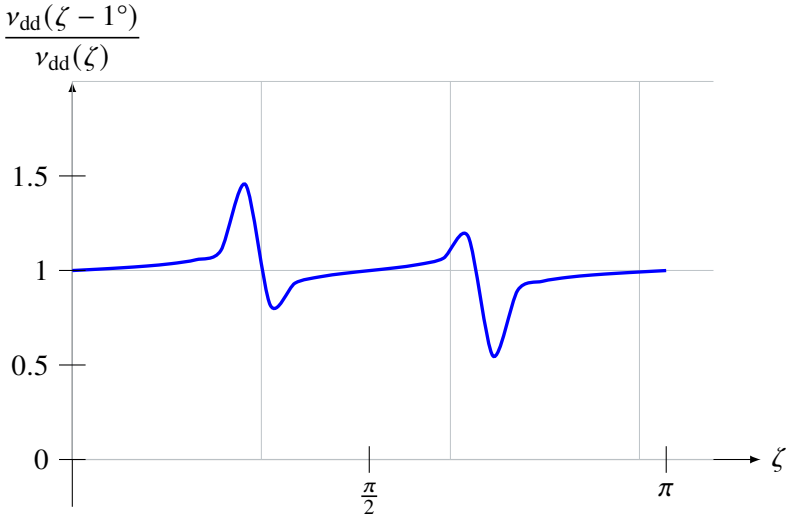

Figure 5.15: Variation of the dipolar coupling dependent on the angle ζ and an alignment change of 1° between the magnetic field orientation and the spin connecting vector. Only around the zero-crossing at $\zeta = 54.75°$ and $\zeta = 125.3°$, a big variation can be determined.

regime is well below 100 kHz and, thus, part of the many narrow dips shown in Fig. 5.14.

In summary, this chapter proofs that a manipulation of electron spins and differentiation between the participating spin species proximal to the measured NV is possible. Nevertheless, to be able to discuss the inter-spin distance of electron spins in more detail and, subsequently, determine the relative spatial distribution of those spins, a more elaborate knowledge of the applied magnetic field is absolutely essential.

6 Magnetic Field Vector Reconstruction

Up to now, the required theory and experiments for NV based EPR measurements of the dipolar coupling between electron spins attached to the diamond surface in the vicinity of the NV have been described and performed. Yet, it got evident that during the performed measurements, a crucial information for the reconstruction of the spin position and spin network distances is missing. Due to the nature of the electron spin interaction described by Eq. 5.1, the coupling strength of two electron spins is dependent on two factors. On the one hand, on their distance, and, on the other hand, strongly dependent on the angle between the connection vector of the spins and the orientation of the magnetic field. The latter one can also be used as a parameter to tune the dipolar coupling strength by variation of the magnetic field orientation.
In order to achieve this, it is important to be able to reconstruct the magnetic field vector $\boldsymbol{B}$ in the general applicable laboratory frame decoupled from the individual NV axis. However, there already exist different approaches for the full determination of the B-field orientation. Hereof, exemplary methods are based on NV ensembles containing all four NV orientations in close proximity[84], ensemble based measurements with continuous wave readout and frequency multiplexing[85], or a strongly coupled carbon nuclear spin in close proximity[86]. Yet, those methods rely on special prerequisites which have to be fulfilled in order to determine the magnetic field orientation.
In the following chapter, a more general method without specific attributes of the NV centres is going to be presented. The description follows Weggler et al.[79] in a more detailed fashion.

6.1 Theoretical Description of the Model

Based on the previously presented B-field misalignment determination (Sec. 2.4.5), the polar angle as well as the B-field amplitude can been determined. Nevertheless, due to the $C_{3\nu}$ symmetry of the NV, the azimuthal angle cannot be defined by this method. In order to break this symmetry, a set of NVs with different orientations but exposed to the same magnetic field can be used.
The main idea is to contract the four orientations shown in Fig. 2.2 into one spot with the vacancy in the centre and the nitrogen atoms in a tetrahedral conformation around the centre position, as it is shown in Fig. 6.1.

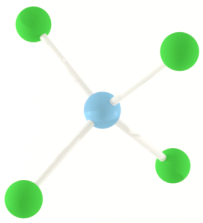

Figure 6.1: Contraction of the four possible NV orientations in diamond (nitrogen green; vacancy blue). Due to symmetry, the four principal axes connecting the nitrogen atoms and the vacancy are along the four crystallographic axes $[\bar{1}\bar{1}1]$, $[1\bar{1}\bar{1}]$, $[111]$, and $[\bar{1}1\bar{1}]$. (Image taken and adapted from Weggler et al.[79].)

This can be done as long as the sample, here the individual NV centres, is moved into the confocal volume and, thus, the magnetic field is identical during all measurements. Hereupon performing ODMR measurements and misalignment calculations according to Balasubramanian et al.[49](Sec. 2.4.5) for at least three of the four NV orientations, a triangulation can be performed where only one possible magnetic field orientation responsible for the individual level shifts can be determined.
For one single NV orientation, the thus determined angle θ ($\theta \overset{!}{\neq} 0°$) results in a cone like shape of infinite possible magnetic field orientations with the NV principal axis as rotation axis for the mapping.
If the knowledge of two different measured NV orientations is combined, this indefiniteness can be reduced to only four possible orientations, containing a factor of 2 due to the directionality of the magnetic field vector (point symmetry with respect to the centre of the tetrahedron if only two axes are considered).
If a third NV orientation is included, this set can be further reduced down to maximally two possible magnetic field orientations (still containing the factor of 2 due to the point symmetry). Yet, due to the direction independence of the scalar product and, thus, the direction independence of the interactions, this leads to a well defined solution in the diamond frame of reference. To additionally define the magnetic field vector in the laboratory frame, the polarisation anisotropy measurement (Sec. 3.1.1) has to be extended to be able to differ between the two similarly reacting NV orientations. This can be achieved by introduction of a second objective atop of the diamond sample, tilted with respect to the optical beam path (modification shown in Fig. 6.2).

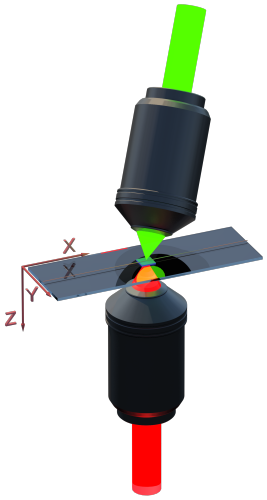

Figure 6.2: Schematic, illustrating the alternative experimental geometry with both objectives focused onto the same spot. The excitation is done via the second, rotatable mounted objective (green optical pathway), which replaces the magnets, while the detection is still performed with the lower objective (red optical pathway). (Image taken from Weggler et al.[79].)

The configuration shown in Fig. 6.2 allows to differ between the two NV orientations by intensity comparison of the fluorescence signal of both axes. If the laser light polarisation is optimised along one of the two axes, the second axis shows a decreased signal and vice versa.

6.2 Mathematical Description

In order to determine the axis orientation of the magnetic field vector, a mathematical description of the problem is necessary. Since only the angular components of the magnetic field are determined, each vector is considered as a unit vector, neglecting its amplitude (length) in all calculations.

6.2.1 Intersecting Cone Model

Here, the first method is the **Intersecting-Cone-Model** (ICM), following the vectorial nature of the underlying physics. After the contraction of the four NV orientations, the cones describing the misalignment angles θ_i for each measured NV axis $\boldsymbol{NV}_i$ are defined by an axis tilted with respect to the individual $\boldsymbol{NV}_i$. Subsequently, this exemplary magnetic field vector can be rotated around $\boldsymbol{NV}_i$, creating a cone of possible field orientations, as shown in Fig. 6.3.
It is important to note, that geometrically those cones do not intersect. As shown in Fig. 6.4, the measurement, as well as the scalar product return the smaller angles for both axes and, thus, the

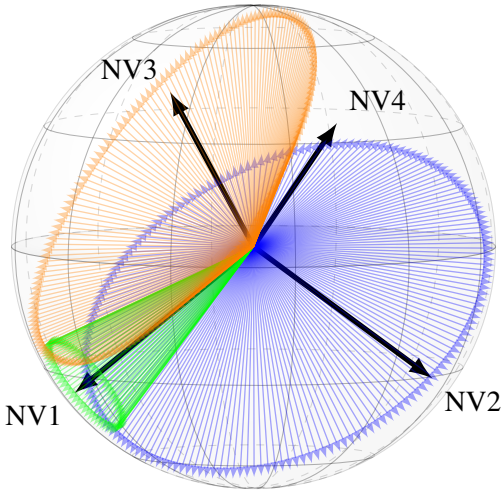

Figure 6.3: Geometric interpretation of the intersecting cone model. The four NV axes are shown in black with three exemplary cones for NV1: $[1\bar{1}\bar{1}]$(green), NV2: $[\bar{1}1\bar{1}]$(orange), and NV3: $[\bar{1}\bar{1}1]$(blue). The cones intersect in one axis, the magnetic field orientation vector responsible for the individual levels determined for the three measured NVs.

sum of two angles result in $\theta_i + \theta_j < 109.47°$ and is therefore smaller than the angle between two NV axes. In order to obtain the intersection of the cones, the possible magnetic field orientations have to be point mirrored with respect to the origin if the misalignment angle fulfils $\theta_\mathrm{i} > 54.735°$.

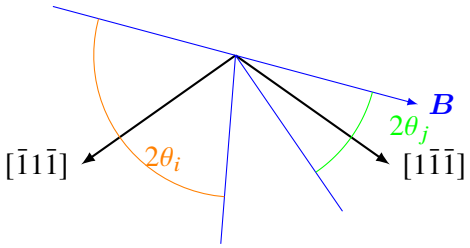

Figure 6.4: 2D interpretation of the intersection of cones of the magnetic field vector for two NV axes. The cones do not intersect due to the direction independence of the scalar product.

After the definition of the cones, the maximum of the scalar product for all possible magnetic field orientations has to be searched. However, since the scalar product is independent of the direction of the used vectors, the point mirroring is only necessary for the pictorial representation of the intersecting cone model. Without this step, the minimum of the scalar product (anti-parallel configuration) is the solution of the magnetic field vector.

For the error calculation, the individual cones have to be defined by the normally distributed angles $\theta_i' \in [\theta_i \pm \Delta\theta_i]$, leading to a rhombus-like shaped surface area of the unit sphere as angular error interval.

A major drawback of this method is the required computing time of the reconstruction which follows a $T \propto n^3$ behaviour, with n the number of individual cone vectors. For the sake of simplicity of this approximation, n is assumed to be equal for the three cones, nevertheless,

it should be chosen proportional to the cone angle θ. Due to the strong dependency of the reconstruction accuracy on the cone granularities, a multitude of scalar products are necessary to achieve an error of less than 2°. Yet, a speed-up can be achieved by a *ranged divide and conquer* method, reducing the number of calculations by a factor of 2^m, with m the number of steps necessary for the algorithms convergence. Therefore, a rougher resolution is used for the first step and then, the resolution is stepwise increased in a range around the possible intersections, with the range dependent on the previous granularity.

6.2.2 Intersection of Spheres

In order to reduce the runtime complexity and increase the calculation accuracy, a varied description of the formalism can be used. Therefore, the magnetic field cones are cut with the unit sphere encircling the four NV axes. This cut can mathematically be described by the intersection of the unit sphere and spheres around the endpoints of the (normalised) NV axes. The radii of those endpoint spheres are defined by the opening angles of the magnetic field cones as shown in Fig. 6.5.

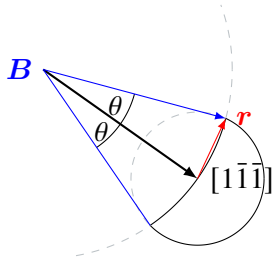

Figure 6.5: Utilisation of the law of cosine for the determination of the radii for the endpoint spheres, exemplary shown for the NV axis $[1\bar{1}\bar{1}]$, the magnetic field $\boldsymbol{B}$, and the respective cone angle θ.

Those radii $\boldsymbol{r}_i$, can be determined by the law of cosine for non-rectangular triangles

$$a^2 = b^2 + c^2 - 2bc\cos(\alpha), \tag{6.1}$$

with the angles opposite to the side labelled with the corresponding Greek letters. Since the magnetic field vector and the NV axes are taken as normalised vectors, the individual radii are calculated as

$$r_i = \sqrt{2 - 2\cos(\theta_i)}. \tag{6.2}$$

Followingly, the endpoint spheres are determined by

$$(x - \mathrm{sgn}(NV_{i,x})1)^2 + (y - \mathrm{sgn}(NV_{i,y})1)^2 + (z - \mathrm{sgn}(NV_{i,z})1)^2 = r_i^2, \tag{6.3}$$

with the signum function extracting each particular axis direction (sign) of the NV axes. The intersection of two spheres in three dimensions results in a plane equation, describing the plane which contains the intersection circle of the spheres (intersection of spheres essential). Therefore,

the final planar equation containing the circle with all possible magnetic field orientations for the i-th NV axis is given as

$$\mathrm{sgn}(NV_{i,x})x + \mathrm{sgn}(NV_{i,y})y + \mathrm{sgn}(NV_{i,z})z = \sqrt{3}\cos(\theta_\mathrm{i})\,. \tag{6.4}$$

In comparison to the intersection of cone model with a direction independent scalar product, this calculation relies on a real point of intersection for the magnetic field vector determination. Therefore, it is important to perform the point mirroring and, thus, the mirrored angles $\theta_i' = 180° - \theta_i$ are used in Eq. 6.4 if the individual misalignment is larger than 54.735°.
In order to determine the final solution vector describing the magnetic field vector, a set of three equations (Eq. 6.4) has to be used. As long as those three planes are linearly independent (not parallel), they intersect in exactly one point for an error-free problem or have a single smallest distance point if the misalignment angles are defective.

6.2.3 Error Calculation

If a set of three plane-equations (Eq. 6.4) for three different NV axes is solved at once, the individual errors are combined and only the mean value is taken into account. This is visible in a non-unit length of the solution magnetic field vector. If for instance one misalignment angle is more defective than the others, this would lead to an averaging in the solving of the set of equations and, thus, a neglect of the distorted character of the measurement. The error would mainly contribute to the length of the solution vector $|\boldsymbol{B}|$, a not considerable parameter due to the restriction of a normalised problem.
A possible solution for this purpose is the additional information about the length of the solution vector

$$|\boldsymbol{B}| = B_x^2 + B_y^2 + B_z^2 \equiv 1. \tag{6.5}$$

The condition of Eq. 6.5 allows to obtain three sets of each time three equations. Hereof, each individual set of three equations consists of twice Eq. 6.4, the permutations of two NV orientations i, j taken out of the four possible orientations (for example NV1 with θ_1 and NV2 with θ_2), and once the normalisation condition of Eq. 6.5. In Fig. 6.6, a 2D projection into the angular components of the resulting solution vectors is shown. In order to combine the results of the three solutions, a covariant distribution, emphasising the distorted character of the measurement can be used.
For the particular solutions shown in Fig. 6.6, each time one million samples are taken from the normally distributed angles $\theta_{i,j} \pm \Delta\theta_{i,j}$ and solved individually. For the final magnetic field vector, the expectation value $\boldsymbol{\mu}$ and its standard deviation $\boldsymbol{\Sigma}$ are defined as the centre and covariance matrix describing the smallest enclosing ellipse, which contains 95.5 % of all simulated points.
Due to the interest in the angular components of the magnetic field vector, a bivariate normal distribution with $\boldsymbol{B}, \boldsymbol{x} \in \mathcal{R}^2$ and $\boldsymbol{\Sigma} \in \mathcal{R}^{2x2}$ and the probability density function

$$p(\boldsymbol{x}; \boldsymbol{B}, \boldsymbol{\Sigma}) = \frac{1}{2\pi\,|\boldsymbol{\Sigma}|^{1/2}} \exp\left\{-\frac{1}{2}(\boldsymbol{x} - \boldsymbol{B})^T \boldsymbol{\Sigma}^{-1}(\boldsymbol{x} - \boldsymbol{B})\right\} \tag{6.6}$$

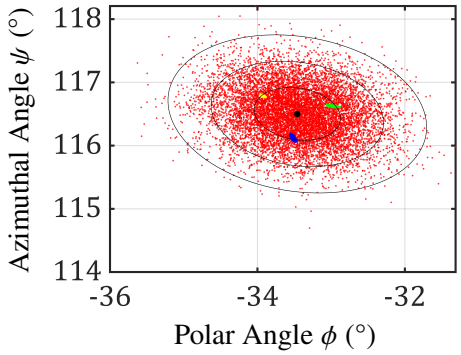

Figure 6.6: Angular distribution (ϕ and ψ) for a B-field orientation vector reconstruction. The expectation value $\boldsymbol{\mu}$ and its standard deviation $\boldsymbol{\Sigma}$ are shown in black with the standard deviation intervals Σ, 2Σ, and 3Σ. They describe a smallest enclosing ellipse, containing 68.2 %, 95.5 %, and 99.7 % of all simulated points. The three distributions shown in yellow, green, and blue represent the solutions of the three individual sets combining two different NV axes at one.

is used for the calculation.

6.3 Measurements and B-Field Vector Reconstruction

As proof of principle, a variety of magnetic field reconstructions have been performed. For this purpose, the first measurement is aimed towards the determination of an achievable error margin and, thus, high resolution pODMR measurements with minimised linewidth are required. The second measurement series is performed to monitor the reproducibility and accuracy of the determination for a known magnetic field change. At the same time, a time consumption estimation allows to classify the usability of this method.
Therefore, the following section describes the sequence of measurements to determine the 3D magnetic field vector in more detail.

6.3.1 Fluorescence Anisotropy

The first necessary measurement for the magnetic field reconstruction is the fluorescence anisotropy measurement (Sec. 3.1.1). This allows a first differentiation between the possible NV orientations into two 2-tuples containing NVs of the ab-pol (marked grey in Fig. 6.7) and the cd-pol (marked white in Fig. 6.7).
As shown in Fig. 6.7, this defined map allows to measure with various NVs of the same polarisation orientation without a further extensive search. Therefore, two confocal images with the laser polarisation rotated accordingly are recorded and the fluorescence signals are compared. For more closely characterised sites, also the specific fluorescence anisotropy measurement as shown in Fig. 3.2 is performed.

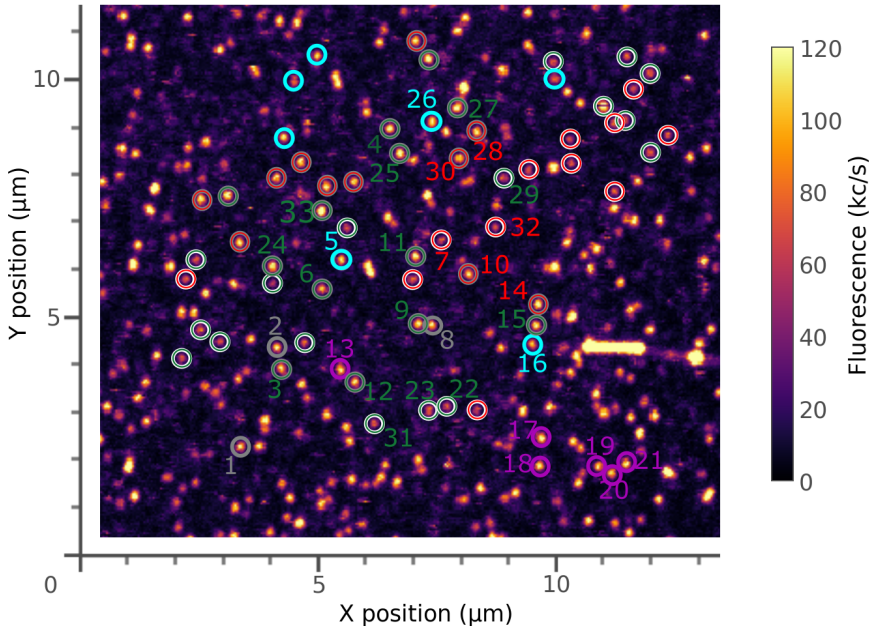

Figure 6.7: Fluorescence scan of the used sample area. This scan shows a part of *T001 Spot2 Map01* with the tagged NVs used for the measurements. The colour coding is dependent on the fluorescence anisotropy, magnetic field parallelism, and measure-ability: Marked with a grey background are NVs of the ab-bol while the white background is used for those NVs of the cd-pol (see Sec. 3.1.1). The red and green shows the differentiation between the magnetic field effect on the NVs of one polarisation direction. Additionally marked are uncharacterised sites in magenta and blinking sites in cyan.

6.3.2 Straining Effect of a Misaligned Magnetic Field

As the fluorescence anisotropy measurement only yields a partial differentiation, another way to further distinguish between the NV orientations is needed. Therefore the influence of a specifically oriented magnetic field onto the different NVs can be employed.
If the magnetic field is aligned parallel to one of the two NV orientations of one polarisation direction, the misalignment angle for the second axis is roughly 70°. Thus, the fluorescence signal of the NVs of the misaligned axis is strongly decreased compared to the ones with an aligned field. This allows to differ between the final two orientations shown in green and red in Fig. 6.7. Additionally and according to Eq. 2.28, the resonance frequencies are dependent on the field orientation angle θ. Thus, already for a weak magnetic field of around 20 G, a clear shift of the ODMR resonance dips can be detected, allowing to verify the assignment even more sufficient. Putting those measurements into a nutshell, it is possible to distinguish between the four possible NV orientations already using simple confocal measurements. This selection allows to define sets of NVs to perform the magnetic field reconstruction measurements.

In Fig. 6.8, the pODMR measurements of a set of three different NV orientations performed at the same magnetic field is shown. Here, the orientation dependent transition frequency positions are clearly visible.

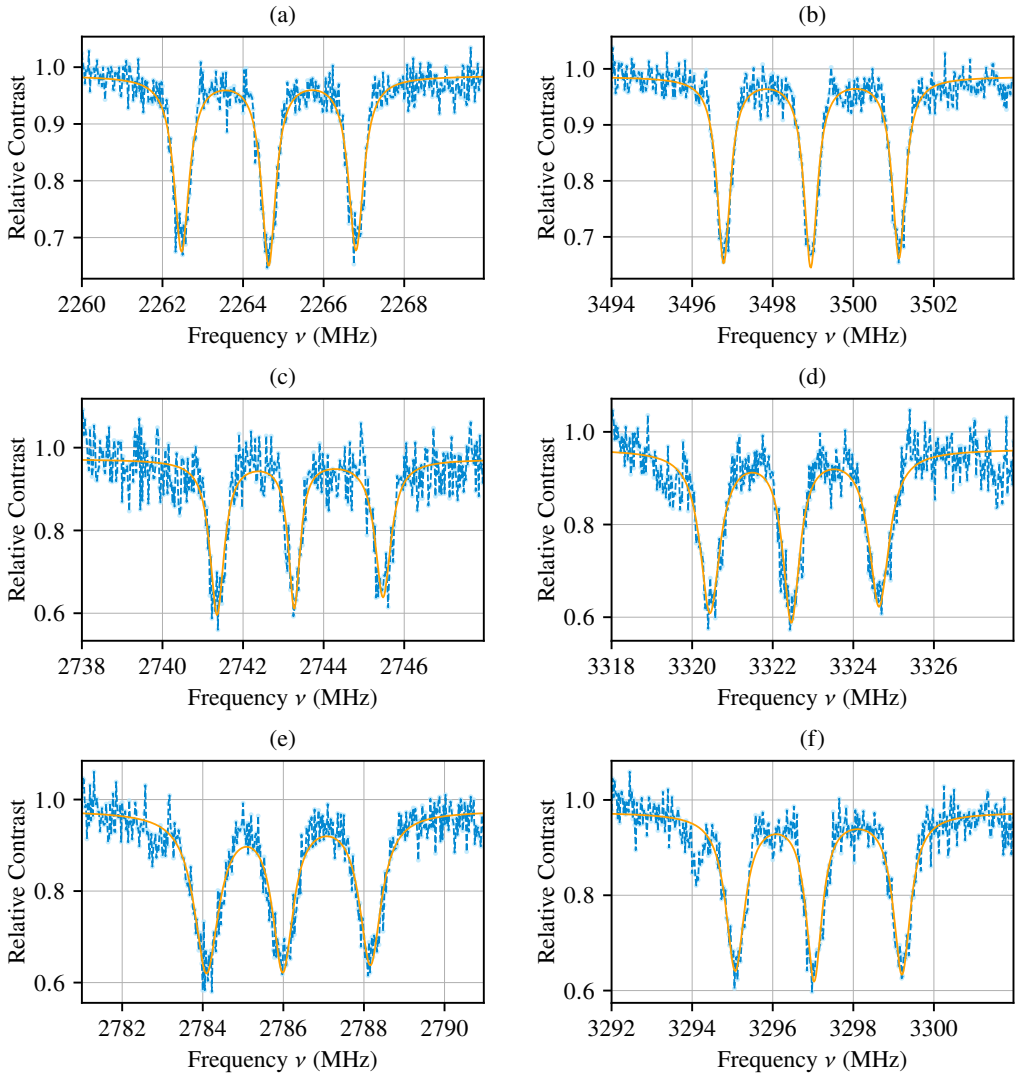

Figure 6.8: Pulsed ODMR measurement results for three different NV orientations, normalised to the individual maximum Rabi contrast. The relative contrast of the fluorescence signal is shown in blue with the Lorentzian fit drawn in orange. For NV1, the transition frequencies $|0\rangle \rightarrow |-1\rangle$ (a) and $|0\rangle \rightarrow |+1\rangle$ (b) with angle $\theta_1 = 13.42°$. For NV2, the transition frequencies $|0\rangle \rightarrow |-1\rangle$ (c) and $|0\rangle \rightarrow |+1\rangle$ (d) with angle $\theta_2 = 62.89°$. For NV3, the transition frequencies $|0\rangle \rightarrow |-1\rangle$ (e) and $|0\rangle \rightarrow |+1\rangle$ (f) with angle $\theta_3 = 66.61°$. To obtain a comparable linewidth, all measurements are performed with a Rabi period of $\Omega \approx 1.58\,\mu s$ while subject to a B-field with $|B| \approx 230\,\text{Gauss}$.

Also striking is the asymmetric shift of the nuclear spin dependent resonance splitting. Here, the energy shift between $I_n = -1$ and $I_n = 0$ for the $m_s = -1$ transitions and between $I_n = +1$ and $I_n = 0$ for the $m_s = +1$ transitions gets smaller compared to the individual second splitting.

In order to investigate this behaviour in more detail, a single NV centre (*T002-2 Spot2 Map01 NV46*) is measured at roughly 230 G for different magnetic field orientations ranging from almost 0° misalignment up to 60° misalignment. In Fig. 6.9, the four frequency differences are shown. For both electron spin transitions, the splitting to the lower frequency dip gets reduced, while the splitting to the higher frequency dip gets increased.

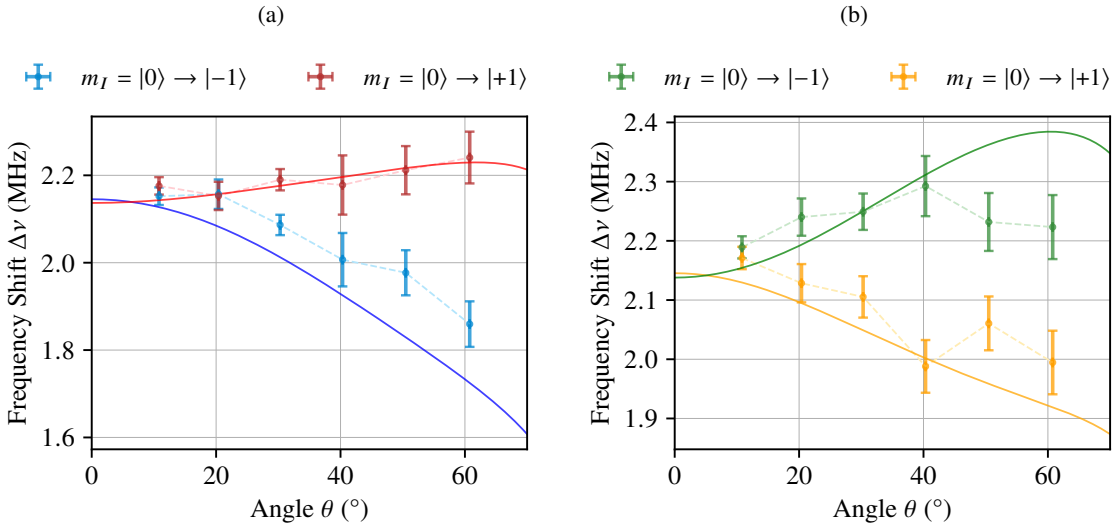

Figure 6.9: Asymmetric shift of the NV transition frequencies due to the ^{14}N nuclear spin interaction. The measurements (dashed lines and points) are performed for both NV electron spin transitions: (a) $m_s = |0\rangle \rightarrow |-1\rangle$, and (b) $m_s = |0\rangle \rightarrow |+1\rangle$ on *T002-2 Spot2 Map01 NV46*. Additionally, the corresponding theory curves are shown as solid lines.

This effect can be seen by a closer investigation of the effecting transition Hamiltonian. Therefore, the NV contributions of the ZFS Hamiltonian (Eq. 2.25) and electron Zeeman Hamiltonian (Eq. 2.28), as well as the nuclear spin contribution of the hyperfine splitting Hamiltonian (Eq. 2.31) have to be considered. Additionally, the Larmor frequency term of the nuclear spin, similar to the electron Zeeman effect has to be taken into account via

$$\mathcal{H} = \omega_{14N} \left(\cos\theta \; I_z + \sin\theta \; I_x\right). \tag{6.7}$$

Solving this eigenvalue problem numerically, a misalignment dependent level splitting can be observed. The corresponding theory curves are also shown in Fig. 6.9, standing in qualitative agreement with the obtained asymmetry.

6.3.3 Reconstruction of the Magnetic Field Orientation

If the magnetic field reconstruction is applied to the measurement data of the first set of measurements shown in Fig. 6.8, a single solution magnetic field vector is obtained. The result shown in Fig. 6.10 contains the B-field vector, the covariance distribution of the error, and the four NV axes.
The simulation yields as solution B-field vector angles

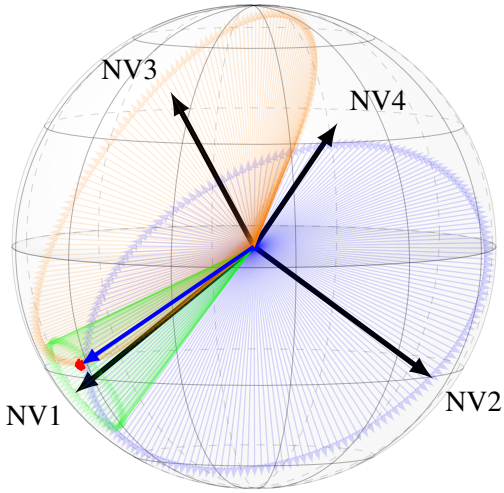

Figure 6.10: Result for the reconstruction of the B-field vector(solid blue) using the data from Fig. 6.8. For the simulation, the axes $[1\bar{1}\bar{1}]$, $[\bar{1}1\bar{1}]$, and $[\bar{1}\bar{1}1]$ are used with the red area representing the angular covariance distribution of the result (500 random points shown from the 10^7 points of the calculated distribution).

$$\boldsymbol{B}_{123}(\phi,\psi) = \begin{pmatrix} -33.46^\circ \\ 116.50^\circ \end{pmatrix} \tag{6.8}$$

with the corresponding covariance matrix

$$\boldsymbol{\Sigma}_{123} = \begin{pmatrix} 0.35^\circ & -0.05^\circ \\ -0.05^\circ & 0.16^\circ \end{pmatrix}. \tag{6.9}$$

These results show an error of less than 0.4° in both components with a small ellipticity (small off-diagonal elements), thus a good agreement of the three measured axes. If for instance the pODMR result of one of the NV axes is replaced by the measurement of the fourth axis, the same result should be obtained. Yet, due to the huge misalignment of $\theta_4 = (83.21 \pm 0.13)^\circ$ measured for the $[111]$ axis, the pODMR measurement shows a very low contrast and, thus, also an imprecise fit result for the actual resonance frequency (measurement shown in Fig. 6.11).

If the simulation is performed for a combination of the first, second, and fourth NV axes, the solution B-field vector angles are

$$\boldsymbol{B}_{124}(\phi,\psi) = \begin{pmatrix} -34.42^\circ \\ 115.86^\circ \end{pmatrix} \tag{6.10}$$

with the corresponding covariance matrix

$$\boldsymbol{\Sigma}_{124} = \begin{pmatrix} 3.8^\circ & 2.4^\circ \\ 2.4^\circ & 1.6^\circ \end{pmatrix}. \tag{6.11}$$

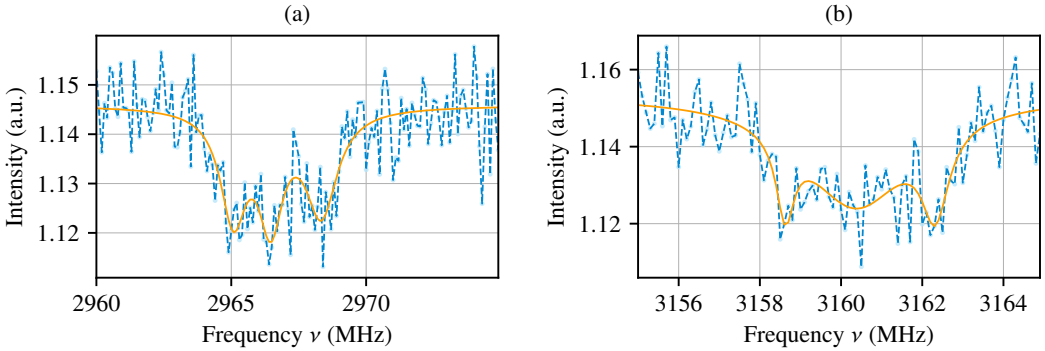

Figure 6.11: pODMR measurement for the [111] NV axis. The fluorescence signal is shown in blue with the Lorentzian fit drawn in orange. The transition frequencies (a) $|0\rangle \rightarrow |-1\rangle$ and (b) $|0\rangle \rightarrow |+1\rangle$ with the resulting misalignment angle $\theta_4 = 83.21°$.

Overall, a good agreement between the two results is obtained. Yet, the larger uncertainty due to the noisy measurement of NV4 in the second combination leads to a larger error with a pronounced ellipticity, confirming the poor angle determination in the case of a large misalignment.

In the second set of measurements, the linear magnet positions (x, y, and z) have been kept constant. However, the rotation stage of the magnet was rotated in 10° steps, starting from a NV axis misalignment of roughly 12° and ranging up to 32°. In order to minimise the measurement duration, only common ODMR measurements are performed.

Table 6.1: Magnet position and resulting magnetic field vector simulation for the stepwise rotation of the magnet stage. These measurements are performed on a set of four NVs: *T002-2 Spot2 Map01 NV09, NV10, NV31, NV32*. The linear axes of the magnet stage are kept constant at $x = 69.90\,\text{mm}$, $y = 93.20\,\text{mm}$, and $z = 272.75\,\text{mm}$. The given B-field values are taken for NV1.

Magnet angle	B-field amplitude and misalignment	B-field vector angles	Covariance matrix
98.8°	251.1 ± 0.2 12.3 ± 0.2	$\begin{pmatrix} -36.65° \\ 115.58° \end{pmatrix}$	$\begin{pmatrix} 0.53° & -0.05° \\ -0.05° & 0.22° \end{pmatrix}$
108.8°	246.1 ± 0.1 22.42 ± 0.07	$\begin{pmatrix} -30.67° \\ 106.81° \end{pmatrix}$	$\begin{pmatrix} 0.12° & -0.16° \\ -0.16° & 0.22° \end{pmatrix}$
118.8°	240.2 ± 0.2 32.49 ± 0.07	$\begin{pmatrix} -25.56° \\ 98.17° \end{pmatrix}$	$\begin{pmatrix} 0.23° & -0.33° \\ -0.33° & 0.48° \end{pmatrix}$

As the results in Tab. 6.1 show, the obtained errors are still on the order of maximally 0.53° and thus comparable to the error obtained for the case of pODMR measurements, resolving the exact transition frequencies. Comparing the resulting three B-field vector solutions, the first rotation led to a variation of the B-field vector of 10.39°, the second rotation yielded another change of

9.98°, and the overall difference between the first and the third rotation angle is 20.37°. As it is also visible in Fig. 6.12, the stepwise rotation of the magnet stage led to a continuous rotation of the reconstructed magnetic field vector confined to a single plain. Additionally, the obtained angle change superposes with the applied rearrangement of the magnet stage, confirming the reproducibility, as well as the accuracy of the developed method.

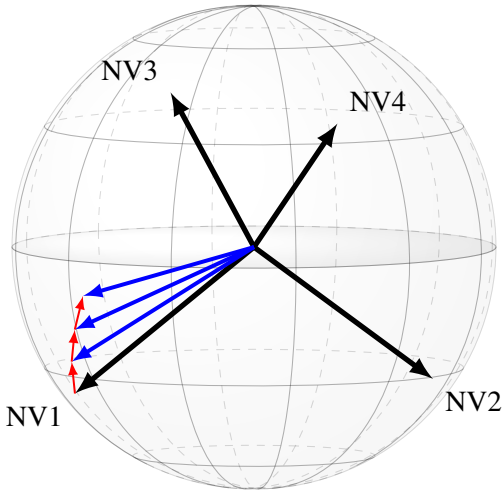

Figure 6.12: Reconstruction of the stepwise change of the magnetic field vector alignment. The three solution magnetic field vectors are drawn in blue with the 10° steps (red) of the rotation confined into a single plane. For the sake of visibility, the covariance error distributions are not shown.

In terms of required measurement time, the measurements for a single magnetic field vector reconstruction can be reduced to four measurements. These are two measurements to determine the B-field amplitude and the misalignment with respect to the first NV axis, and two measurements of either the $m_s = |0\rangle$ to $m_s = |-1\rangle$ or $m_s = |0\rangle$ to $m_s = |+1\rangle$ transition for the two additionally required axes. With those values, the missing two transition frequencies can be calculated, solving the eigenvalue problem as described in Sec. 6.3.2. Therefore, the measurements for one magnetic field vector reconstruction are in the range of 30 min – 60 min. For the simulation, the calculation of a single point is on the order of a few µs, thus not contributing to the overall duration.

Concludingly, the here presented method gives the ability to determine precise information about all three components of the magnetic field. This allows to furthermore determine the angular difference of various magnetic field vectors applied to a NV centre, or a network of interacting electron spins.
Combining this knowledge with the performed EPR measurements presented in chapter 5, it is possible to gather the information, necessary for the reconstruction of the dipolar interaction between electron spins.

7 Electron Spin Distance Reconstruction

In order to gather all prerequisites necessary for the determination of the inter-electron-spin-distance, all previous chapters are dedicated to the comprehension of the sensor (chapter 2), the applied measurement schemes (chapter 3), and the underlying mechanisms as dipolar coupling and the magnetic field reconstruction (chapter 5 and chapter 6). However, no explicit reconstruction of the distance or position of the electron spins has been presented yet.
In the following chapter, a framework for a possible method to simulate the spin network and the distance between those spins is introduced. This method is based on the data obtained by DEER (Sec. 3.3.1) and AXY-N (Sec. 3.2.3) measurements and methodologically related to the ICM (Sec. 6.2.1). To understand the connection, an inversion of the ICM has to be considered: Similar to the reconstruction of the magnetic field vector, the orientation of a NV can be reconstructed by ODMR measurements, however, for the inverted method three know magnetic field vectors are used and the ODMR measurements for each field are performed on a single NV. In this case, the intersection of the three cones around the magnetic field orientations is achieved only in the underlying NV axis.
In the following chapter, a similar principle is used for the reconstruction of the underlying electron-spin distance of a measured set of dipolar interactions.

7.1 Intersecting Cone Model Revisited

Comparable to the ICM, the principle of the electron spin distance reconstruction is as single underlying vector contained in all cones around the magnetic field vectors passed to the simulation. Once again, only the orientation of this vector is of importance, neither the length, nor the spatial location directly contribute to the model.
In order to reconstruct this vector, first, the distance space $\left[\left|\boldsymbol{r}_{\mathrm{ee,min}}\right|, \left|\boldsymbol{r}_{\mathrm{ee,max}}\right|\right]$ is sampled in steps, with the step size and distance interval being free parameters strongly influencing the time consumption and accuracy of the simulation. For each element of this distance space, the simulation is done once, calculating the most-likely solutions responsible for the passed dipolar couplings.
In the second step, the distance samples r_i and the dipolar couplings $\nu_{dd,j}$, where j denotes each element of the set of measured dipolar couplings, are used to calculate an array of possible angles responsible for the individual dipolar couplings $\nu_{dd,j}$. Due to the underlying angle dependent function of the dipolar interaction, k can range from zero up to four, therefore, up to four angles ζ_k ($k \in [0,4]$) can be responsible for a sole dipolar coupling strength. Considering only the angle dependent part of the dipolar interaction (see also Eq. 5.1)

$$\nu_{dd,j} = \left(3\cos^2\zeta_{j,k} - 1\right)\ f\left(|r|^3\right), \tag{7.1}$$

Fig. 7.1 shows the regions with two (green) and four (red) solutions for a given distance r_i.

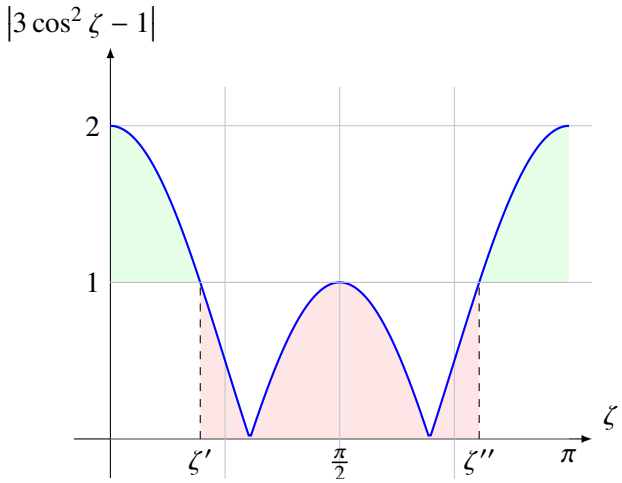

Figure 7.1: Angular dependency of the electron spin dipolar interaction, showing the two regions with two (green area) and four (red area) possible solutions.

Due to the absorption of the interaction sign, the codomain of $\left(3\cos^2\zeta_{j,k} - 1\right)$ is restricted to $[0,2]$, thus combining the possible solutions ζ_k between $\zeta' = 35.27°$ and $\zeta'' = 144.73°$. Due to the pseudo-random values of the sample distances r_i, zero solutions are possible if the measured interaction strength is higher than

$$\nu_{dd,j} > 2\ f\left(|r_i|^3\right). \tag{7.2}$$

This second step has to be done for each dipolar coupling $\nu_{dd,j}$ individually, resulting in

$$K = \prod_{\forall j} k(\nu_{dd,j}) \tag{7.3}$$

possible solutions. Due to the decreasing dipolar coupling strength for an increasing distance r_i, this equation has a minimum for an overestimation and a maximum for an underestimation of the inter-spin-distance. Therefore, it can be useful to implement a break after convergence, and at the same time starting with $|\boldsymbol{r}_{\mathrm{ee,max}}|$ while decreasing the distance.
As final simulation step for one sampled value r_i, the overlap of the obtained possible solutions has to be calculated. This is done by the ICM method, creating cones with the obtained possible solution angles $\zeta_{j,k}$ around the magnetic field vectors $\boldsymbol{B}_j$. For those cones the extreme value of the scalar product has to be found for each combination of each time two out of the j cones of all K solutions. It is apparent, that the granularity of the sampled cones, similar to the original ICM, drastically impacts the runtime of the simulation. In the overlap calculation, a confidence interval for the acceptance can be defined, usually set to 95 %, reducing the returned space of false possible solutions tremendously.
In order to obtain the final solutions, the returned solution vectors have to be used to re-calculate the dipolar couplings resulting for the given conformation. By comparison with the dipolar couplings obtained by the original measurement, the space of false possible solutions can be reduced even further. Here, the deviation can be calculated according to

$$\Delta\nu_{\mathrm{dd}} = \left\{ \sum_{\forall j} (\nu_{dd,j,\mathrm{sim}} - \nu_{dd,j,\mathrm{meas}})^2 \right\}^{\frac{1}{2}}, \tag{7.4}$$

eliminating all sets with a deviation higher than a threshold value $\Delta\nu_{\mathrm{dd,max}}$. Since the comparison also takes the orientations and thus, the angle between the spin connecting vector and the magnetic field vector into account, a minimum of Eq. 7.4 is found for the underlying inter-electron-spin distance *and* orientation.

7.2 Functionality- and Quality-Test of the Simulation

For the validation of the simulation, first, three magnetic field vectors have to be assumed. This is done twice to compare the solutions for the same electron spin distance reconstruction.
The first set (Fig. 7.2a) starts with one B-field aligned along NV4 ([111]), and the other two freely rotated with respect to this axis by each two random rotations between 0° and 180°. The second set (Fig. 7.2b) takes the same rotation angles, but starts with the first B-field axis aligned along NV3 ($[\bar{1}\bar{1}1]$). Yet, both starting orientations can also be chosen without any further restrictions. Here, they are aligned along the NV axes due to simplicity and because measurements would be done in a same manner.
Secondly, as the intention is to verify the reconstruction of an electron spin distance, an arbitrarily oriented electron spin connection vector of length $|\boldsymbol{r}_{\mathrm{ee}}| = 5$ nm is defined. For this vector, both sets of the three magnetic field orientations are used to calculate the dipolar interaction strengths,

normally obtained through the measurement. It is important to note that due to the measurement scheme (AXY-N measurement presented in Sec. 3.2.3), the sign of the dipolar interaction gets neglected and thus, only the positive values for the dipolar interaction strengths are determined. Using those three dipolar interaction values without the inter-spin distance, the simulation is monitored for its convergence by reconstructing the underlying electron spin connection. As given in Tab. 7.1 for the set shown in (Fig. 7.2a), the reconstruction shows a good agreement with the obtained dipolar interaction (smallest $\Delta\nu_{\mathrm{dd}}$) for the originally used values.

Table 7.1: Electron spin distance reconstruction for a simulated system of two electron spins measured for three magnetic field orientations. The first row (green) shows the values from the system simulation (ground truth), while the red marked rows show the configuration with the smallest deviation to the simulated values. Only the subspace for 5 nm is given, though the reconstruction is performed for possible distances $\boldsymbol{r}_{\mathrm{ee}} \in [4.2, 5.8]$ nm with a step size of 0.1 nm.

$\lvert r_{ee}\rvert$ in nm	$\nu_{\mathrm{dd},1,\mathrm{sim}}$ in kHz	$\nu_{\mathrm{dd},2,\mathrm{sim}}$ in kHz	$\nu_{\mathrm{dd},3,\mathrm{sim}}$ in kHz	$\Delta\nu_{\mathrm{dd}}$ in kHz
5.0000	437.4888	153.4428	568.4867	0
5.0000	326.8971	79.3405	440.5122	184.6596
5.0000	-341.8694	-366.6680	-330.4881	333.5437
5.0000	437.6176	-152.5171	568.1585	0.9905
5.0000	-326.8658	-388.6853	-313.1909	364.3521
5.0000	-138.4508	-330.4792	-95.9731	586.5448
5.0000	-205.7582	-351.2722	-173.5698	498.7934
5.0000	-212.7618	-280.5646	-181.6440	465.0908
5.0000	-165.3552	-248.9485	-126.9904	527.3491
5.0000	-165.3552	-248.9485	-126.9904	527.3491
5.0000	-212.7618	-280.5646	-181.6440	465.0908
5.0000	-205.7582	-351.2722	-173.5698	498.7934
5.0000	-138.4508	-330.4792	-95.9731	586.5448
5.0000	-326.8658	-388.6853	-313.1909	364.3521
5.0000	437.6176	-152.5171	568.1585	0.9905
5.0000	-341.8694	-366.6680	-330.4881	333.5437
5.0000	326.8971	79.3405	440.5122	184.6596

In Tab. 7.1 two rows are highlighted as possible solutions. Both describe the same problem, but due to the use of the scalar product in the simulation, they are the anti-parallel solution vectors resulting in the same dipolar coupling strengths.
Comparing both reconstructions shown in Fig. 7.2, the simulation converges towards the same result vector even so very different starting problems are passed. Yet, it got evident that dependent on the orientation difference between the B-field vectors and the solution electron spin connection vector, the simulation can be very time and resource consuming. In order to avoid these problems, a break condition and a *divide and conquer* like algorithm can be implemented, reducing the

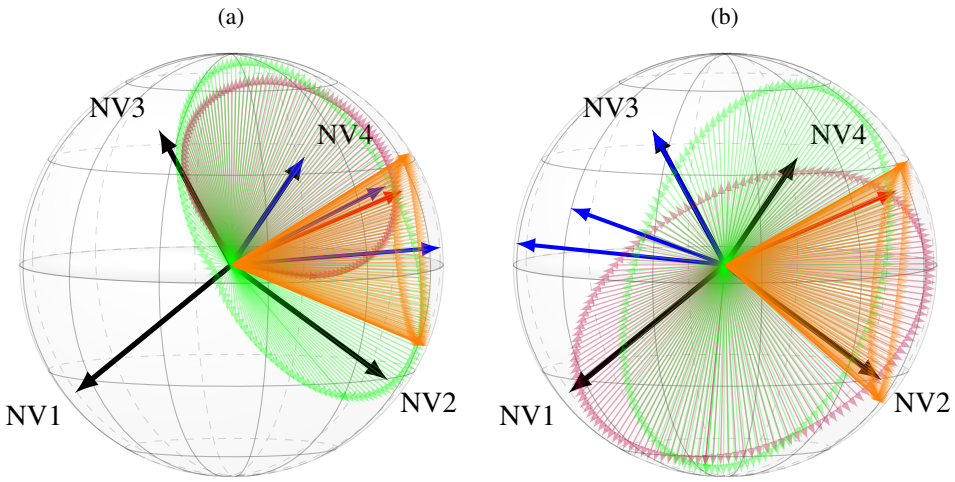

Figure 7.2: Result for the reconstruction of the electron spin distance. (a) The first set of three B-field vectors (blue) with the first vector aligned along NV4. The other two vectors are obtained by random rotations of the first B-field vector. (b) The second set of three B-field vectors (blue) achieved by the same rotation angles, yet NV3 as starting axis. For both reconstructions, the same electron spin vector is used and the solution is shown as the intersection of the three cones (red vector).

calculation effort.

Since the magnetic field vectors are not the same for all problems, a solution similar to the intersecting sphere model (Sec. 6.2.2) can not be implemented. Such a model would require fixed axes for the creation of a general and well defined system of equations.

Overall, this method opens up a reliable possibility to reconstruct the distance between two electron spins, based on the interaction measured by the help of a NV centre. Although an individual reconstruction is time costly, it needs to be done only once for a given set of interacting spins, thereby, lessening the effect of the long calculation time in relation to the measurement time of the contributing dipolar interactions. Furthermore, due to the structure of the simulation, it is possible to extend the number of reconstructed electron spin distances. In doing so, the number of possible solutions calculated in Eq. 7.3 increases due to the increasing number of interactions between n electron spins with

$$\binom{n}{2} = \frac{n!}{2(n-2)!} \tag{7.5}$$

individual interactions.

8 Conclusion and Outlook

This thesis worked towards the reconstruction of an interacting electron spin network, attached as spin-labels to specific sites of biomolecules, such as enzymes or proteins. For this purpose, shallow NV centres in diamond are considered as possible sensors, susceptible enough to measure the interactions on a single molecules level. In particular, we want to reconstruct the distance between individual electron spins based on measurements of their dipolar coupling.

In the first experimental part of this work (chapter 5), we showed that it is possible to use shallow NVs as sensors to measure magnetic resonance signals arising from proximal spins. Furthermore, we are now able to distinguish between electron and nuclear spins, dependent on the sensed interaction and the signal response to a variation of the magnetic field. In order to simplify the detection of electron spins, the demanded go-to targets for the distance reconstruction of molecules, we demonstrated the feasibility of the resonant MW manipulation and spin state sensing of non-NV electron spins, using various NV-based readout methods. Following the results of these EPR sensing measurements, a lack of information about the magnetic field orientation became evident, prohibiting a distance reconstruction with the measured electron spin resonances. In the second part of this thesis (chapter 6), we established a reliable method to reconstruct the three-dimensional orientation of an arbitrarily oriented magnetic field vector applied to the NV centre and its vicinity. This new method allows to obtain all necessary information for the distance reconstruction with a now defined set of measurements. Nevertheless, the results described in chapter 5 cannot be re-evaluated due to the required set of measurements unknown in the first place. Due to the simplicity of the used optical setup and, at the same time, the absence of specific requirements of the employed NV centres, this method is generally feasible and can be performed on most setups and samples without any further complications. This feasibility through simplicity therefore allows us to characterise the magnetic field at the focus of the objectives confocal volume universally, even more, to use this method as an actual calibration for other non-NV-based measurements.
In the last part (chapter 7), we designed a framework to simulate the electron-spin-network configuration, more explicitly, the distance and interactions between the networked electron spins. The used quantities for this reconstruction are dipolar couplings and magnetic field vectors, measurable with the presented measurement sequences, calculations, and the NV as sensor. In order to test the distance reconstruction we used artificial systems of electron spin configurations, showing a reliable convergence of the reconstructed electron spin network independent of the pseudo-measured input. Up to now, this spin-network reconstruction is implemented for only two interacting electron spins, however, the framework here easily allows for an extension with only minor modifications of the code. Yet, due to the mathematical complexity of the reconstruction, this increase of networking spins results in a major increase of the average calculation time.

Recapitulating, we were able to prove the potential of using NVs in diamond as EPR sensors and developed the framing theory and evaluation to combine all necessary quantities for the reconstruction of an interacting electron spin network. From here on, the next step is the reconstruction of the position and distance of an actual spin system, such as surface radicals, commonly located on the diamond surface after a *tri-acid cleaning*[16]. Due to their stable location on the diamond surface, they present an elementary system with a reduced number of degrees of freedom, as for example a fixed height and no disruptive translation or rotation as flexible linkers would exhibit. Therefore, they can now be used to further investigate the still unknown effects of the various parameters on the AXY sensing measurements (exemplary measurements described in Sec. 5.3.3).

After reconstructing the spatial structure of the surface radicals, it is important to increase the degrees of freedom in a well-controlled manner. One way to achieve this may rely on *DNA origami* structures. These structures can be designed to label site-specifically, allowing to create an electron spin network with a desired number of spin labels in defined distances with respect to each other.[87] This step can be divided into two tasks: the nano-positioning of the DNA on the diamond surface and stabilising the photo-stability of the electron spin labels. Considering the first task, one solution to position and bind the DNA onto the diamond may be based on carboxylation, a surface functionalisation method allowing to tether DNA strands to hydroxide ions on the diamond surface.[88] Alternative ways are offered by diamond surface treatment as used for nano-diamonds, attaching DNA-origamis via charge and hydrophobic interactions in order to have fluorescent centres in close proximity.[89] Now, further considering the second task, the electron spin labels require a higher photo-stability, otherwise prohibiting long DEER measurements due to photo-bleaching of the antennas.[17,88] Here, various improvements can be done. Firstly, and following the measurement schemes presented in chapter 5, the performed sensing schemes can be optimised in terms of measurement time, reducing the photo-bleaching effect by a shorter measurement duration. Secondly, and in order to overcome the short lifetime, different labelling schemes, such as as ionised metal ions, can be used as more stable spin labels. Here, different metal centres as Cu^{2+} or Mn^{2+} were already established in DEER experiments performed with biomolecules, proving to be reliable and stable antennas for dipolar coupling measurements.[90]

9 Appendix

A.1: Unitary Transformation

In order to investigate interactions in quantum mechanics and quantum optics, a commonly used tool is the unitary transformation into the *rotating frame*. In order to resolve part of the time evolution, this transformation allows a change of the reference frame, resulting in a more simple system to interpret.
If the system Hamiltonian $\mathcal{H}_S$ is assumed to be in the Schrödinger picture, the time evolution of the state $|\Psi\rangle_S$ can be calculated as

$$i\hbar\frac{\partial\,|\Psi\rangle_S}{\partial \mathrm{t}} = \mathcal{H}_S\,|\Psi\rangle_S\,. \tag{9.1}$$

Taking the unitary operator $U = e^{i\frac{At}{\hbar}}$ with A a hermitian operator, the state transformation from the Schrödinger picture into the rotating frame is

$$|\Psi\rangle = U\,|\Psi\rangle_S\,. \tag{9.2}$$

Combining Eq. 9.2 with the Schrödinger equation (Eq. 9.1), it transforms as

$$\begin{aligned} i\hbar\frac{\partial U\,|\Psi\rangle_S}{\partial \mathrm{t}} =& i\hbar U\frac{\partial\,|\Psi\rangle_S}{\partial \mathrm{t}} + i\hbar\frac{\partial U}{\partial \mathrm{t}}\,|\Psi\rangle_S \\ =& \left(U\mathcal{H}_S U^\dagger + i\hbar\frac{\partial U}{\partial \mathrm{t}}U^\dagger\right)|\Psi\rangle_S \end{aligned} \tag{9.3}$$

Hence, the transformation into the rotating frame is given as

$$\mathcal{H} = U\mathcal{H}_S U^\dagger + i\hbar\frac{\partial U}{\partial \mathrm{t}}U^\dagger. \tag{9.4}$$

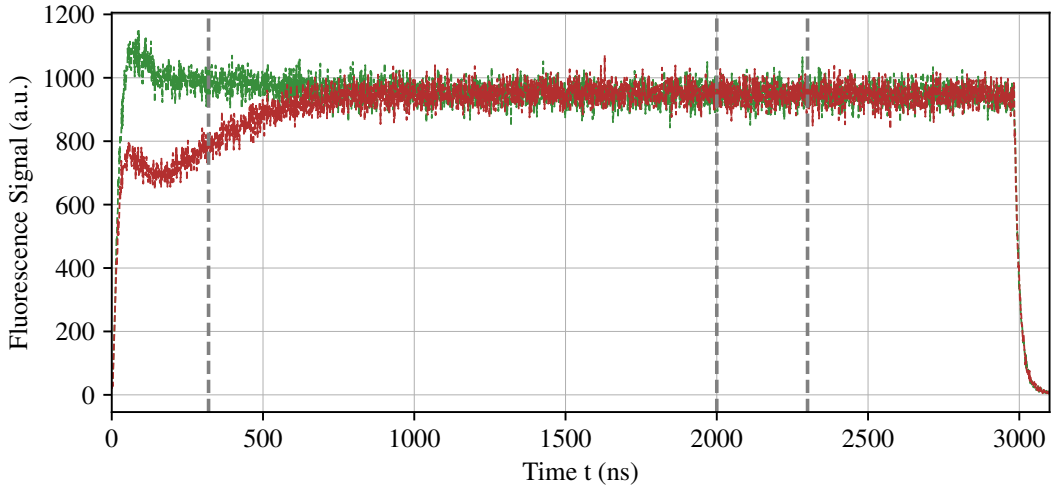

Figure 9.1: Fluorescence signal of the NV for a 3 µs laser pulse. The green data illustrates the signal obtain for the NV initially in the bright state, while the red data corresponds to the fluorescence signal for the NV initially in the dark state. For the normalisation, the count signal after $\tau_{\text{ref}} \sim 1.5\,\mu\text{s}$ is used. The sum of counts framed by the dashed lines and the fluorescence signals are used for the state read-out (0 ns – 300 ns) and the normalisation (1500 ns – 1800 ns) of the NV spins state.

A.2: Readout and State Information

In order to optically initialise the NV in the $m_s = 0$ ground state, a green laser (532 nm) has to be applied to the NV for roughly 1 μs. The optical excitation allows an all-optical read-out of the initial NV state by detection of the fluorescence signal.[20]
For the determination of the initial state of the NV, the laser illumination is prolonged and lasts 3 μs. In the first 300 ns of this illumination, the NV initial spin state information is contained. The acquired counts during this illumination are used as *NV state signal*. The second part after 1.5 μs contains the steady state signal of the bright state $m_s = 0$ and is used as *NV reference signal* (exemplary data shown in Fig. 9.1).

For the calculation of the fluorescence signal, the signal of both intervals are compared:

$$\text{Intensity} = \frac{\text{NV state signal}}{\text{NV reference signal}}. \tag{9.5}$$

During the performed experiments, the average count rate is between $50\frac{\text{k\#}}{s}$ and $150\frac{\text{k\#}}{s}$. Therefore, the expected number of incident photons during the 300 ns of the NV state signal detection is roughly $0.01 - 0.05$. For the purpose of signal identification, the signal has to overcome the photon shot noise limitation $\sqrt{N}$ of the N detected photons, and, thus, it is essential to repeat the individual read-out many times:
In terms of the in this work used resonance detection methods, as for instance the XY and AXY methods and a sensed frequency of ~ 300 kHz, this results in $\sim 10^5$ detection intervals per second.

A single sequence with an alternating read-out consists normally of ~ 400 points, resulting in less than 10 photons detected per second and single point read-out.

A.3: Setup Components

Part Description	Supplier	Part Number
Arbitrary Waveform Generator	Tektronix	AWG 70001a
Avalanche Photo Diode	Excelitas	SPCM-AQRH-14
Digital-Analog Converter	National Instruments (NI)	NI USB-6343
Diode Laser	Toptica	iBeam Smart 515-S
Fibre Coupler	Schäfter+Kirchhoff	60FC-F-4-M12NIR-10
FPGA	Opal Kelly	XEM6310-LX45
Microwave Amplifier	Amplifier Research (ar)	50HM1GAB-47M1
Microwave Switch	Mini Circuits	ZASWA-2-50DR+
Microwave Wire	Goodfellow	CU005171 Cu Wire
Multi Axis Positioning System	Physical Instruments (PI)	LS110 12" 2SM
		2x LS110 6" 2SM
		PRS-110 PK24501B
		2x SMC Hydra Pollux
Objective	Nikon	CFI P-Apo 100x Oil-Objective
Optical Components	AHF	Bandpass-Filter F47-515
		Langpass-Filter F76-631
	Thorlabs	Beam Sampler BSF20-F
		Lens AC254-100-B-ML-1"
		Lens AC254-060-B-ML-1"
		Norland Optical Adhesive NOA63
		Pinhole P25S
		sm Fiber Patch P1-630A-FC-2
		$\frac{\lambda}{2}$-Plate AQWP05M-600
Vector Signal Generator	Rohde & Schwarz	SMIQ03B
2D Piezo Stage System	Physical Instruments (PI)	C-867.260 Piezo Controller
		M-686 XY Stage
3D Piezo Stage System	Physical Instruments (PI)	E-727.3RDA

A.4: CAD-Constructions

All CAD-Constructions have been created in Autodesk Inventor Professional 2019.

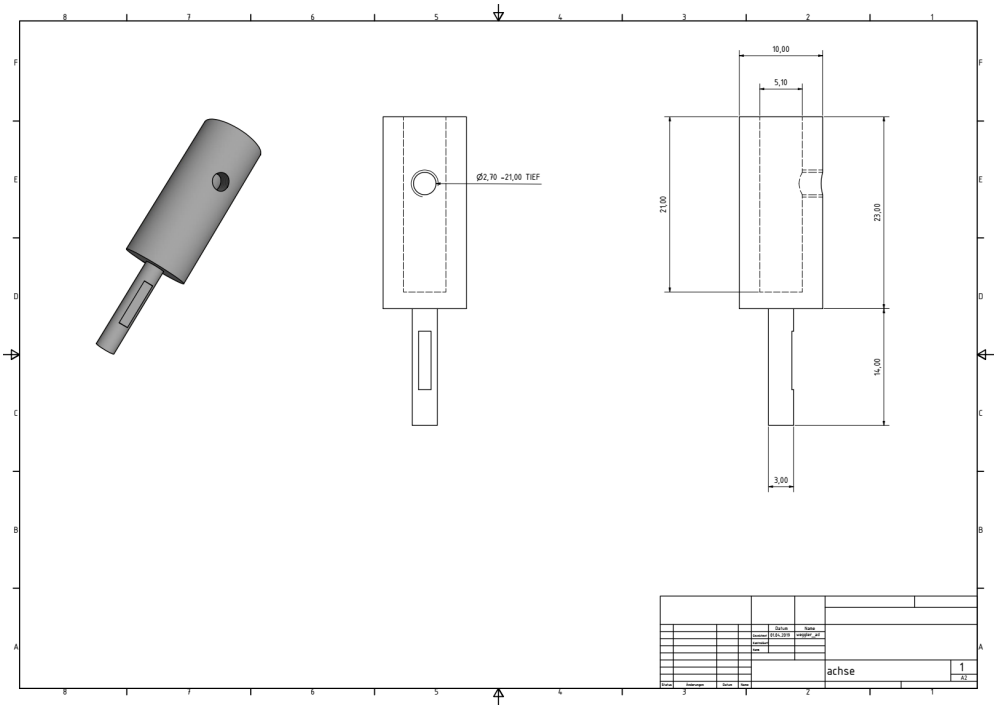

CAD technical drawing: Shaft adapter for the motor of the $\frac{\lambda}{2}$ rotation stage.

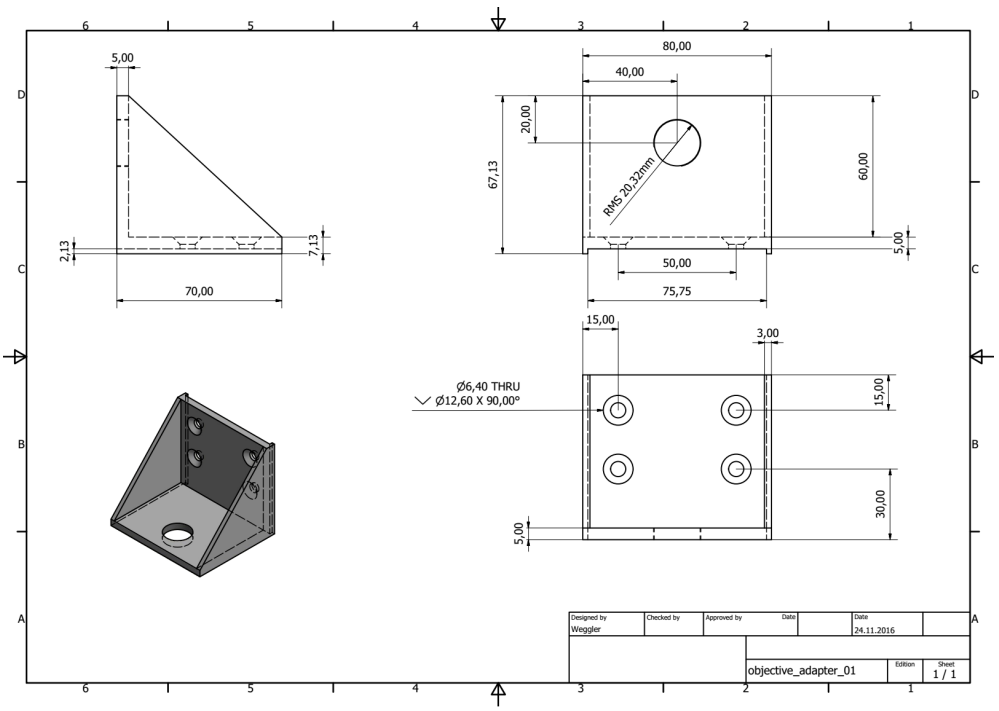

CAD technical drawing: Objective adapter for the translation of the microscope objective along the optical path (focusing on the diamond surface).

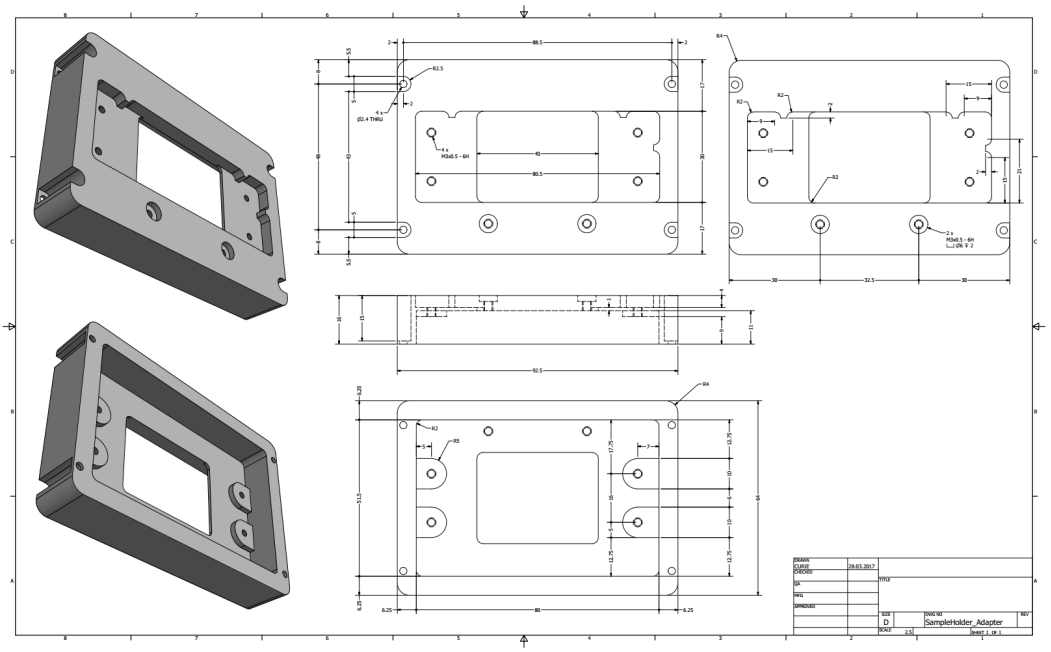

CAD technical drawing: Adapter to attach the sample holder to the 3D piezo stage of the sample positioning.

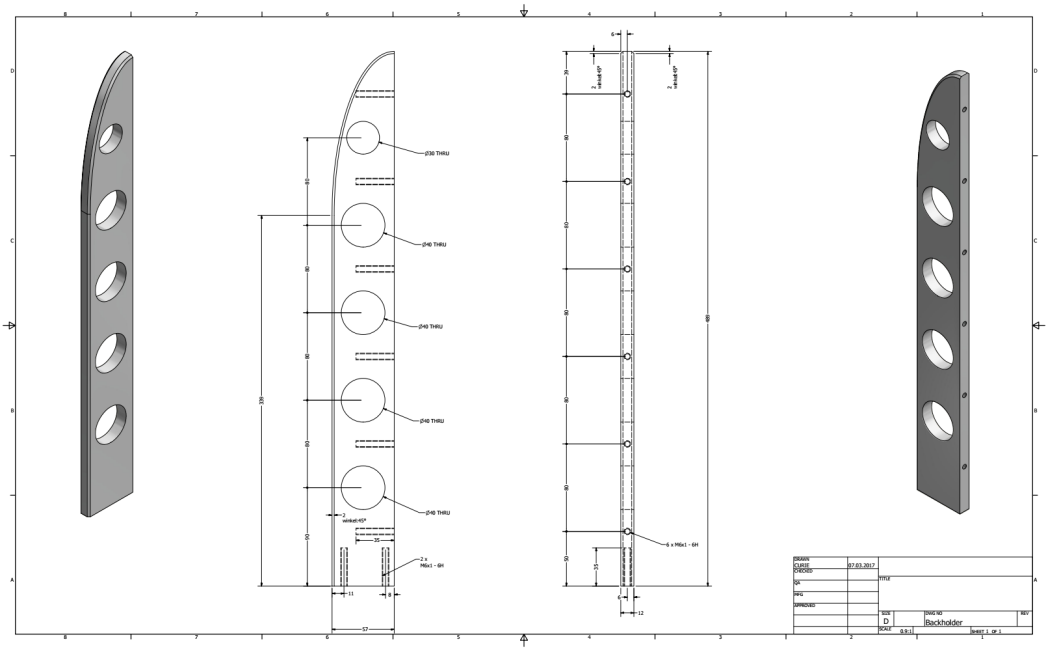

CAD technical drawing: Support mount for the translation stage assembly (for 12" linear stage).

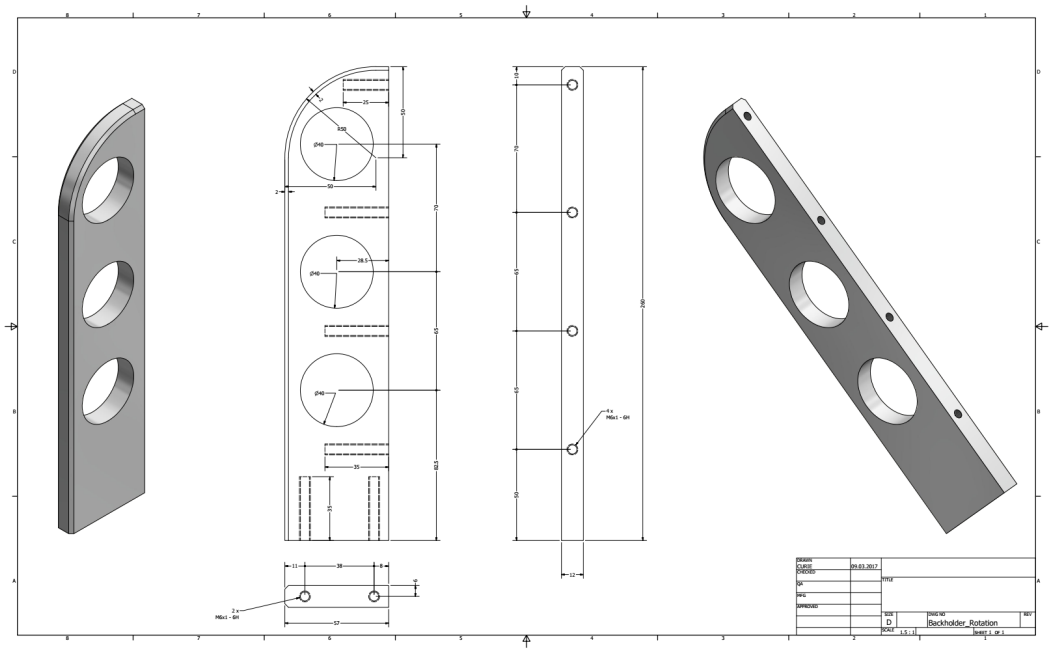

CAD technical drawing: Support mount of the translation stage assembly (for 6" linear stage and the rotation stage).

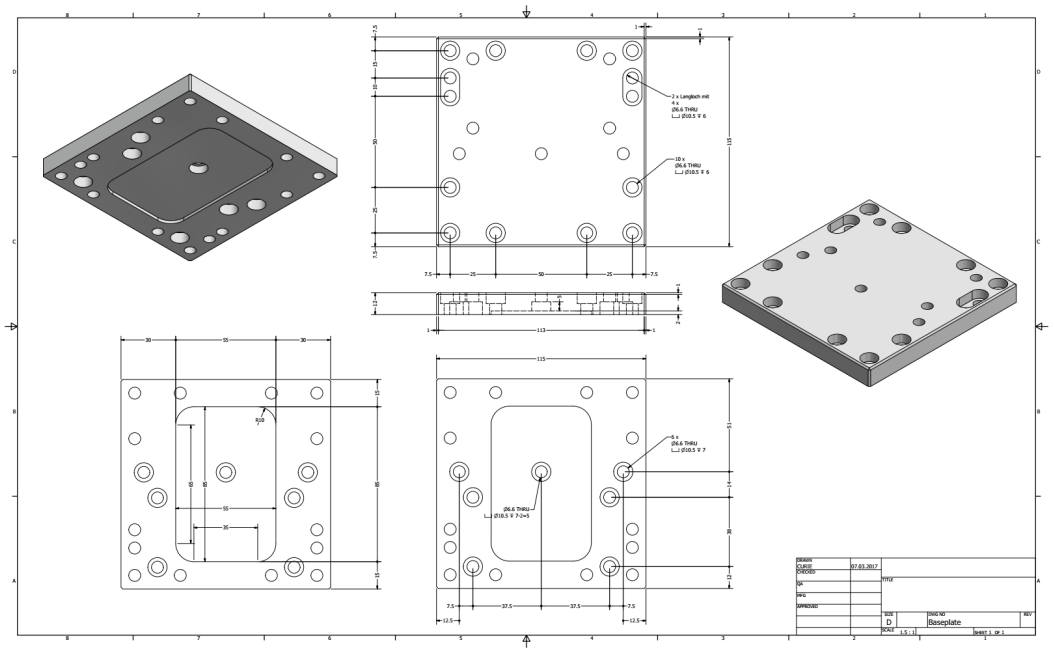

CAD technical drawing: Base of the stage assemblies.

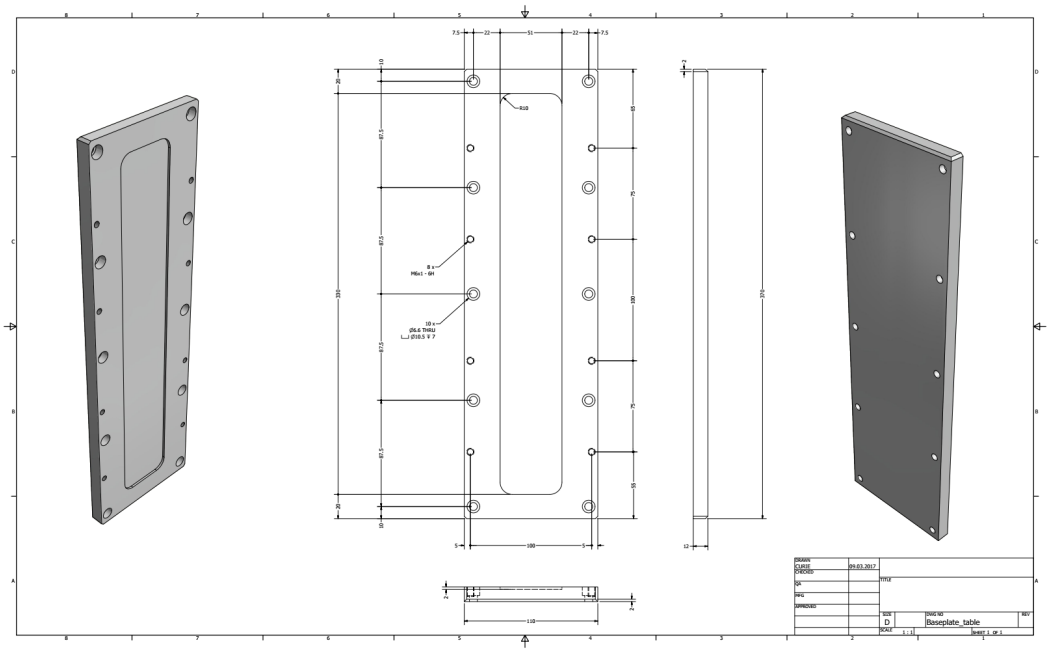

CAD technical drawing: Table-base of the entire magnet stage assembly.

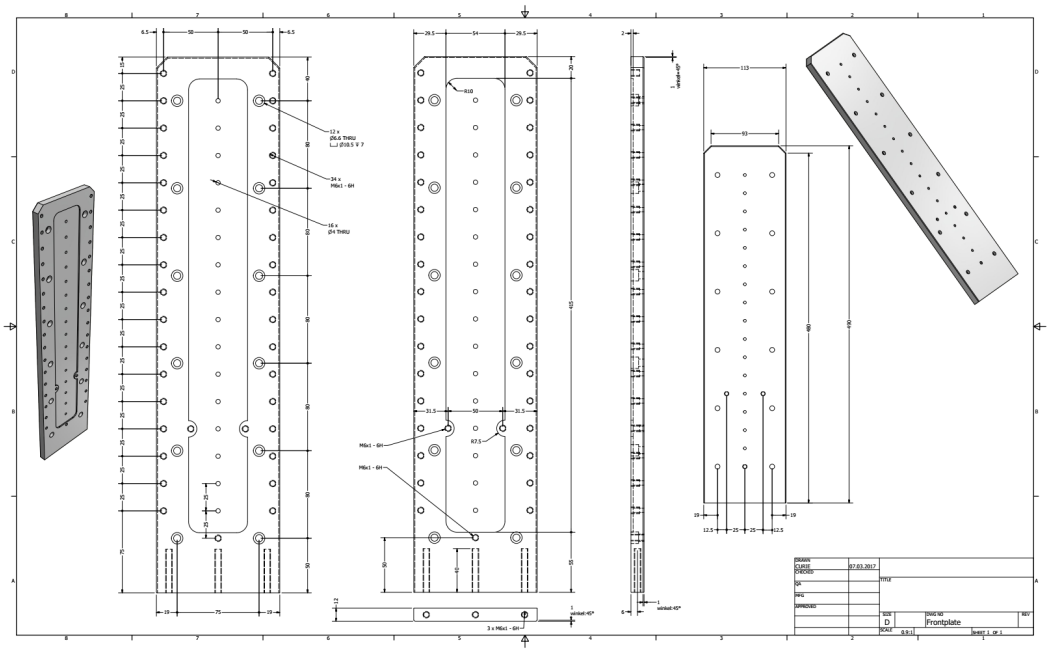

CAD technical drawing: Back-plate for the vertical assembly of the 12" linear stage.

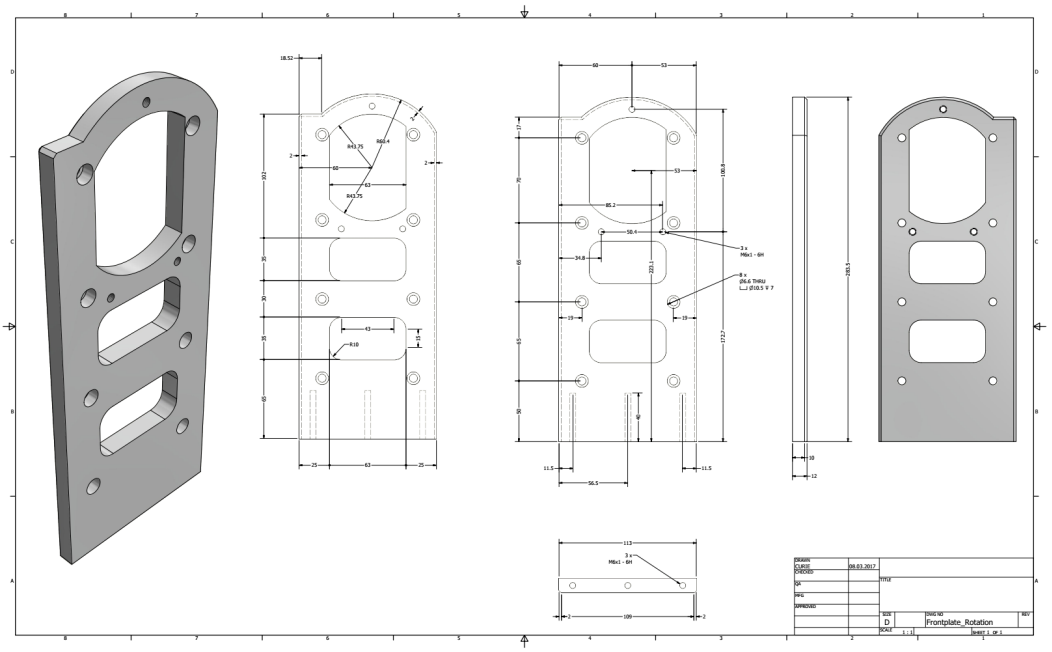

CAD technical drawing: Back-plate for the horizontal assembly of the rotation stage.

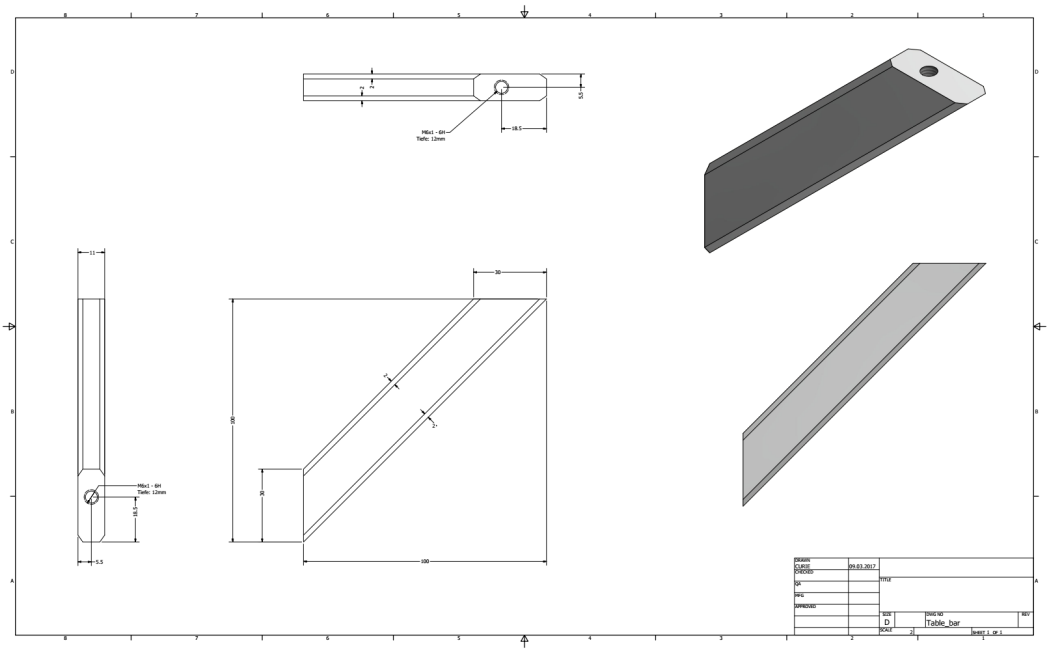

CAD technical drawing: Force transmission bar for the table assembly.

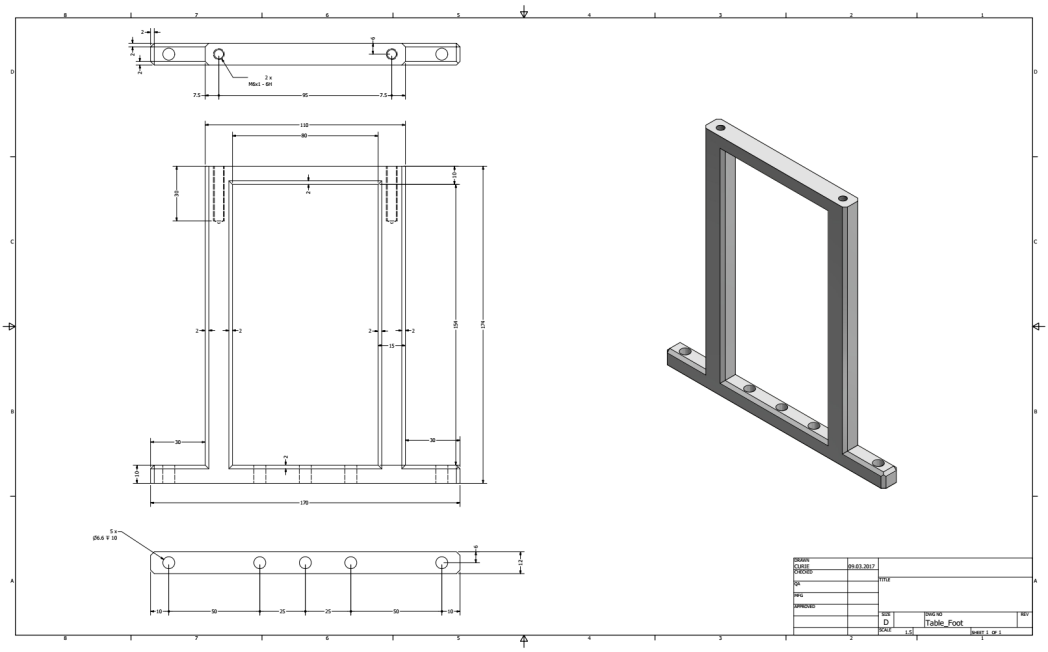

CAD technical drawing: Middle pillar of the table assembly.

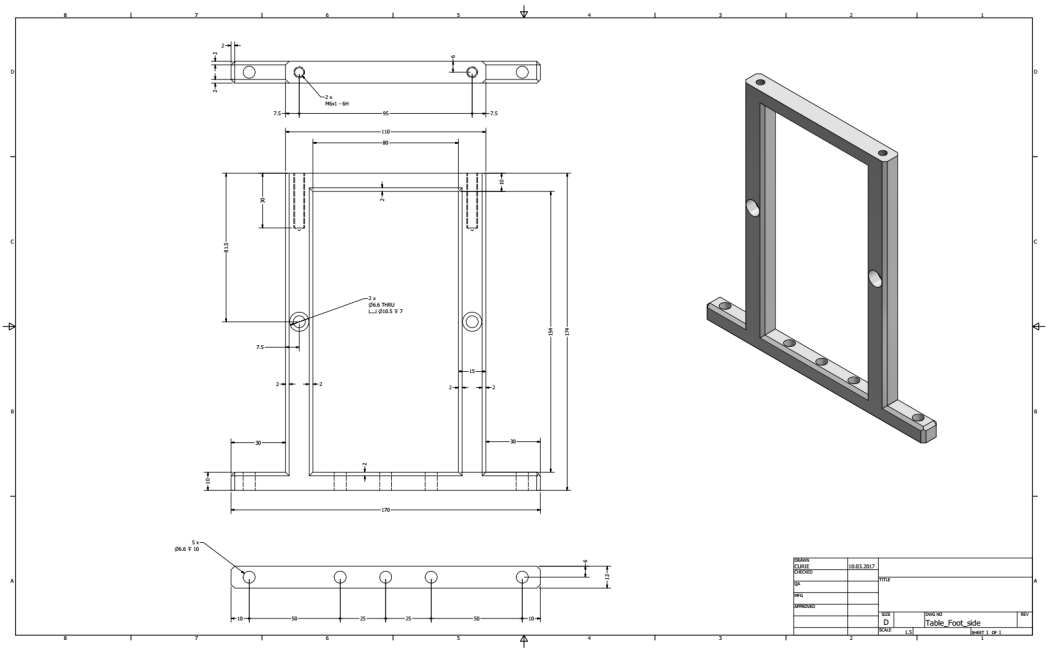

CAD technical drawing: Side pillar of the table assembly.

A.5: Lambda-Half Plate Rotation Stage

An image of the whole assembly of the rotation stage with the $\lambda/2$-plate mounted in the setup is shown in Fig. 9.2.

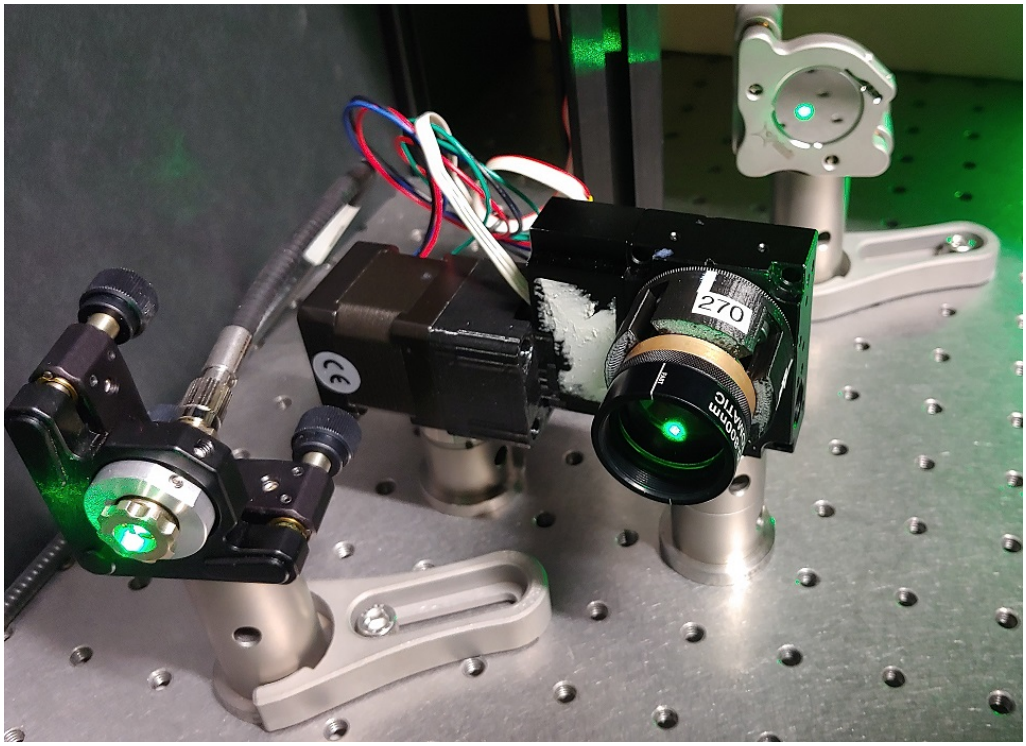

Figure 9.2: Image of the home-build rotation stage for the $\lambda/2$-plate in the optical pathway.

The control itself is done via an '*Arduino Nano*' in combination with the '*Pololu A4988 Stepper Motor Driver Carrier*' and a '*Pololu NEMA14 Stepper Motor*'. There are nine cables connected to the Arduino:

- two for the power supply of the stepper-driver board (orange=5V, yellow=gnd),
- three for the stepper motor control (red=D6=step, orange=D7=direction, yellow=D8=enable/sleep),
- two for the zero switch of the rotation stage (purple1=D4, purple2=gnd),
- and two to the bottom of the Arduino for the **Light-Emitting Diode** (LED) control (black=gnd, red=D5=+(pwm-controlled)).

Additionally, the two power supply cables for the stepper motor, the five connections from the Arduino are attached to the Stepper Motor Driver Carrier:

- the power supply for the stepper motor (white=+=9V,black=-=gnd),
- the power supply for the stepper driver (orange=+=5V, yellow=-=gnd),

- and the motor control (S=step=red, D=direction=orange, E=enable=yellow).

The stepper motor itself has to be attached to the white socket on the stepper driver board and the direction of the zero-switch should does not matter. It has to be ensured, that the extra power supply can deliver at least 12 V and 1 A.
The $\lambda/2$-plate is screwed into a $M25$ thread which is glued onto a 3D printed adapter. Via four $M3$ screws, the waveplate and adapter are connected to the rotation mount.
For an additional illumination of the sample, the LEDs can be used as a faint light source.
To connect the Arduino to the PC, a **COmmunication Port** (COM)-Port connection needs to be operated with:

- 115200 baud
- 8 Bits
- Parity None
- One stop bit
- No flow control

For the hardware programming, *arduinoC* is used and the communication can be done with the following COM-commands:

- PWM <value> can be set between 0 and 255 and will set the brightness of the LEDs
- ROT <value> will rotate the stage by <value> degree, > 0 will rotate **clock wise** (CW), < 0 will rotate **counter-clock wise** (CCW)
- GOTO <value> will rotate table to <value> degree
- GET will return the position if zeroed
- ZERO will find the zero position
- HELP will print this help

All input for the stage control has to be floating point (one floating point digit) in degree and integer for the LED control. The conversion between *microsteps*, *steps*, and *input towards the wished amount of the degree to turn the stage* is given by *steps to turn = angle(in degree)×90*.
If the switch is not touched, the ZERO command rotates the stage CCW with full speed until it finds the switch position. Afterwards, it turns the stage in 1° steps CW slowly back until it touches the switch. If the switch is touched when the ZERO command is called, the stage rotates for 5° CW and then performs the same approach as in the previous case.
As a speed-up, the stage decides to turn CW or CCW, dependent on the shortest way to the input value. One full rotation takes roughly 90 s and the duration for the rotation command is returned after sending the command.

List of Figures

List of Tables

List of Acronyms

ac alternating current.

APD Avalanche Photo-Diode.

AWG Arbitrary Waveform Generator.

CCW counter-clock wise.

COM COmmunication Port.

cryo EM Cryogenic Electron Microscopy.

CVD Chemical Vapour Deposition.

CW clock wise.

DD Dynamical Decoupling.

DEER Double Electron-Electron Resonance.

EPR Electron Paramagnetic Resonance.

fcc face-centred cubic.

FID Free Induction Decay.

FPGA Field-Programmable Gate Array.

FRET Förster Resonance Energy Transfer.

FWHM Full Width Half Maximum.

HPHT High-Pressure High Temperature.

ICM Intersecting-Cone-Model.

LED Light-Emitting Diode.

MW microwave.

NMR Nuclear Magnetic Resonance.

NV Nitrogen Vacancy.

ODMR Optically Detected Magnetic Resonance.

PELDOR Pulsed ELectron-electron DOuble Resonance.

PID Proportional-Integral-Derivative.

pp Peak-to-Peak.

QuBit Quantum Bit.

SNR signal to noise ratio.

TTL Transistor–Transistor Logic.

USB Universal Serial Bus.

XRC X-Ray Crystallography.

ZFS Zero-Field Splitting.

Bibliography

[1] Matthew P Blakeley, Samar S Hasnain, and Svetlana V Antonyuk. Sub-atomic resolution x-ray crystallography and neutron crystallography: promise, challenges and potential. *IUCrJ*, 2(4):464–474, 2015. doi:10.1107/S2052252515011239.

[2] Joachim Frank. Advances in the field of single-particle cryo-electron microscopy over the last decade. *Nature protocols*, 12(2):209–212, 2017. doi:10.1038/nprot.2017.004.

[3] THOMAS M JOVIN and DONNA J ARNDT-JOVIN. Fret microscopy: digital imaging of fluorescence resonance energy transfer. application in cell biology. In *Cell Structure and Function by Microspectrofluorometry*, pages 99–117. Elsevier, 1989. doi:10.1016/B978-0-12-417760-4.50012-4.

[4] K Ravi Acharya and Matthew D Lloyd. The advantages and limitations of protein crystal structures. *Trends in pharmacological sciences*, 26(1):10–14, 2005. doi:10.1016/j.tips.2004.10.011.

[5] Vanessa Cabra and Montserrat Samsó. Do's and don'ts of cryo-electron microscopy: a primer on sample preparation and high quality data collection for macromolecular 3d reconstruction. *JoVE (Journal of Visualized Experiments)*, 95:e52311, 2015. doi:10.3791/52311.

[6] Eitan Lerner, Thorben Cordes, Antonino Ingargiola, Yazan Alhadid, SangYoon Chung, Xavier Michalet, and Shimon Weiss. Toward dynamic structural biology: Two decades of single-molecule förster resonance energy transfer. *Science*, 359(6373), 2018. doi:10.1126/science.aan1133.

[7] Rahul Roy, Sungchul Hohng, and Taekjip Ha. A practical guide to single-molecule fret. *Nature methods*, 5(6):507–516, 2008. doi:10.1038/NMETH.1208.

[8] M Beckers, F Drechsler, T Eilert, J Nagy, and J Michaelis. Quantitative structural information from single-molecule fret. *Faraday discussions*, 184:117–129, 2015. doi:10.1039/c5fd00110b.

[9] Nicole Malkusch, Thilo Dörfler, Julia Nagy, Tobias Eilert, and Jens Michaelis. smfret experiments of the rna polymerase ii transcription initiation complex. *Methods*, 120:115–124, 2017. doi:10.1016/j.ymeth.2017.04.011.

[10] Julia Nagy, Tobias Eilert, and Jens Michaelis. Precision and accuracy in smfret based structural studies—a benchmark study of the fast-nano-positioning system. *The Journal of chemical physics*, 148(12):123308, 2018. doi:10.1063/1.5006477.

[11] Björn Hellenkamp, Sonja Schmid, Olga Doroshenko, Oleg Opanasyuk, Ralf Kühnemuth, Soheila Rezaei Adariani, Benjamin Ambrose, Mikayel Aznauryan, Anders Barth, Victoria

Birkedal, et al. Precision and accuracy of single-molecule fret measurements—a multi-laboratory benchmark study. *Nature methods*, 15(9):669–676, 2018. doi:10.1038/S41592-018-0085-0.

[12] Robert M Clegg. The history of fret. In *Reviews in fluorescence 2006*, pages 1–45. Springer, 2006. doi:10.1007/0-387-33016-X_1.

[13] Adam Muschielok and Jens Michaelis. Application of the nano-positioning system to the analysis of fluorescence resonance energy transfer networks. *The journal of physical chemistry B*, 115(41):11927–11937, 2011. doi:10.1021/jp2060377.

[14] Tobias Eilert, Eleni Kallis, Julia Nagy, Carlheinz Roöcker, and Jens Michaelis. Complete kinetic theory of fret. *The Journal of Physical Chemistry B*, 122(49):11677–11694, 2018. doi:10.1021/acs.jpcb.8b07719.

[15] Gunnar Jeschke and Yevhen Polyhach. Distance measurements on spin-labelled biomacromolecules by pulsed electron paramagnetic resonance. *Physical Chemistry Chemical Physics*, 9(16):1895–1910, 2007. doi:10.1039/b614920k.

[16] AO Sushkov, I Lovchinsky, N Chisholm, Ronald Lee Walsworth, Hongkun Park, and Mikhail D Lukin. Magnetic resonance detection of individual proton spins using quantum reporters. *Physical review letters*, 113(19):197601, 2014. doi:10.1103/PhysRevLett.113.197601.

[17] Fazhan Shi, Qi Zhang, Pengfei Wang, Hongbin Sun, Jiarong Wang, Xing Rong, Ming Chen, Chenyong Ju, Friedemann Reinhard, Hongwei Chen, et al. Single-protein spin resonance spectroscopy under ambient conditions. *Science*, 347(6226):1135–1138, 2015. doi:10.1126/science.aaa2253.

[18] NB Manson, JP Harrison, and MJ Sellars. Nitrogen-vacancy center in diamond: Model of the electronic structure and associated dynamics. *Physical Review B*, 74(10):104303, 2006. doi:10.1103/PhysRevB.74.104303.

[19] Fedor Jelezko, T Gaebel, I Popa, A Gruber, and Jorg Wrachtrup. Observation of coherent oscillations in a single electron spin. *Physical review letters*, 92(7):076401, 2004. doi:10.1103/PhysRevLett.92.076401.

[20] Joanne Harrison, MJ Sellars, and NB Manson. Optical spin polarisation of the nv centre in diamond. *Journal of luminescence*, 107(1):245–248, 2004. doi:10.1016/j.jlumin.2003.12.020.

[21] Lawrence S Pan and Don R Kania. *Diamond: electronic properties and applications*. Springer Science & Business Media, 2013. doi:10.1007/978-1-4615-2257-7.

[22] Pierre Cartigny. Stable isotopes and the origin of diamond. *Elements*, 1(2):79–84, 2005. doi:10.2113/gselements.1.2.79.

[23] W Kaiser and WL Bond. Nitrogen, a major impurity in common type i diamond. *Physical Review*, 115(4):857, 1959. doi:10.1103/PhysRev.115.857.

[24] HB Dyer, FA Raal, L Du Preez, and JHN Loubser. Optical absorption features associated with paramagnetic nitrogen in diamond. *Philosophical Magazine*, 11(112):763–774, 1965. doi:10.1080/14786436508230081.

[25] FP Bundy, H Tracy Hall, HM Strong, and RH Wentorf. Man-made diamonds. *nature*, 176 (4471):51–55, 1955. doi:10.1038/176051a0.

[26] Mutsukazu Kamo, Yoichiro Sato, Seiichiro Matsumoto, and Nobuo Setaka. Diamond synthesis from gas phase in microwave plasma. *Journal of Crystal Growth*, 62(3):642–644, 1983. doi:10.1016/0022-0248(83)90411-6.

[27] Shreya Nad, Yajun Gu, and Jes Asmussen. Growth strategies for large and high quality single crystal diamond substrates. *Diamond and related materials*, 60:26–34, 2015. doi:10.1016/j.diamond.2015.09.018.

[28] JJ Gracio, QH Fan, and JC Madaleno. Diamond growth by chemical vapour deposition. *Journal of Physics D: Applied Physics*, 43(37):374017, 2010. doi:10.1088/0022-3727/43/37/374017.

[29] Thomas Unden, Nikolas Tomek, Timo Weggler, Florian Frank, Paz London, Jonathan Zopes, Christian Degen, Nicole Raatz, Jan Meijer, Hideyuki Watanabe, et al. Coherent control of solid state nuclear spin nano-ensembles. *npj Quantum Information*, 4(1):1–6, 2018. doi:10.1038/s41534-018-0089-8.

[30] Gordon Davies, Simon C Lawson, Alan T Collins, Alison Mainwood, and Sarah J Sharp. Vacancy-related centers in diamond. *Physical Review B*, 46(20):13157, 1992. doi:10.1103/PhysRevB.46.13157.

[31] Sébastien Pezzagna, Detlef Rogalla, Dominik Wildanger, Jan Meijer, and Alexander Zaitsev. Creation and nature of optical centres in diamond for single-photon emission—overview and critical remarks. *New Journal of Physics*, 13(3):035024, 2011. doi:10.1088/1367-2630/13/3/035024.

[32] J Meijer, B Burchard, M Domhan, C Wittmann, Torsten Gaebel, I Popa, F Jelezko, and J Wrachtrup. Generation of single color centers by focused nitrogen implantation. *Applied Physics Letters*, 87(26):261909, 2005. doi:10.1063/1.2103389.

[33] Marcus W Doherty, Julia Michl, Florian Dolde, Ingmar Jakobi, Philipp Neumann, Neil B Manson, and Jörg Wrachtrup. Measuring the defect structure orientation of a single nv-centre in diamond. *New Journal of Physics*, 16(6):063067, 2014. doi:10.1088/1367-2630/16/6/063067.

[34] N Aslam, G Waldherr, P Neumann, F Jelezko, and J Wrachtrup. Photo-induced ionization dynamics of the nitrogen vacancy defect in diamond investigated by single-shot charge state detection. *New Journal of Physics*, 15(1):013064, 2013. doi:10.1088/1367-2630/15/1/013064.

[35] Liam Paul McGuinness. *Nanoscale quantum sensing using nitrogen-vacancy centres in diamond*. PhD thesis, The University of Melbourne, 2012.

[36] Michael Lurie Goldman, Alp Sipahigil, MW Doherty, Norman Ying Yao, SD Bennett, M Markham, DJ Twitchen, NB Manson, Alexander Kubanek, and Mikhail D Lukin. Phonon-induced population dynamics and intersystem crossing in nitrogen-vacancy centers. *Physical review letters*, 114(14):145502, 2015. doi:10.1103/PhysRevLett.114.145502.

[37] Hermann Haken and Hans Christoph Wolf. *Molecular physics and elements of quantum chemistry: introduction to experiments and theory*. Springer Science & Business Media, 2013. doi:10.1007/978-3-662-08820-3.

[38] GD Fuchs, VV Dobrovitski, R Hanson, A Batra, CD Weis, T Schenkel, and DD Awschalom. Excited-state spectroscopy using single spin manipulation in diamond. *Physical review letters*, 101(11):117601, 2008. doi:10.1103/PhysRevLett.101.117601.

[39] A Batalov, C Zierl, T Gaebel, P Neumann, I-Y Chan, G Balasubramanian, PR Hemmer, F Jelezko, and J Wrachtrup. Temporal coherence of photons emitted by single nitrogen-vacancy defect centers in diamond using optical rabi-oscillations. *Physical review letters*, 100(7):077401, 2008. doi:10.1103/PhysRevLett.100.077401.

[40] VM Acosta, A Jarmola, E Bauch, and D Budker. Optical properties of the nitrogen-vacancy singlet levels in diamond. *Physical Review B*, 82(20):201202, 2010. doi:10.1103/PhysRevB.82.201202.

[41] National Institute of Standards and Technology. The nist reference on constants, units, and uncertainty, 2019. URL `https://physics.nist.gov/cgi-bin/cuu/Category?view=html&All+values.x=80&All+values.y=11`.

[42] Jacek W Hennel and Jacek Klinowski. Magic-angle spinning: a historical perspective. In *New techniques in solid-state nmr*, pages 1–14. Springer, 2005. doi:10.1007/b98646.

[43] NRS Reddy, NB Manson, and ER Krausz. Two-laser spectral hole burning in a colour centre in diamond. *Journal of Luminescence*, 38(1-6):46–47, 1987. doi:10.1016/0022-2313(87)90057-3.

[44] S Felton, AM Edmonds, ME Newton, PM Martineau, D Fisher, DJ Twitchen, and JM Baker. Hyperfine interaction in the ground state of the negatively charged nitrogen vacancy center in diamond. *Physical Review B*, 79(7):075203, 2009. doi:10.1103/PhysRevB.79.075203.

[45] P Reichart, G Tamanyan, DN Jamieson, S Prawer, F Jelezko, T Gaebel, I Popa, M Domhan, J Wrachtrup, et al. Implantation of labelled single nitrogen vacancy centers in diamond using 15n. *arXiv preprint cond-mat/0511722*, 2005. doi:10.1063/1.2158700.

[46] Jianming Cai, Fedor Jelezko, Martin B Plenio, and Alex Retzker. Diamond-based single-molecule magnetic resonance spectroscopy. *New Journal of Physics*, 15(1):013020, 2013. doi:10.1088/1367-2630/15/1/013020.

[47] JC Cordes. The secular approximation with dipole-dipole interaction. *Journal of Physics B: Atomic and Molecular Physics*, 20(7):1433, 1987. doi:10.1088/0022-3700/20/7/012.

[48] A Gruber, A Dräbenstedt, C Tietz, L Fleury, J Wrachtrup, and C Von Borczyskowski. Scanning confocal optical microscopy and magnetic resonance on single defect centers. *Science*, 276(5321):2012–2014, 1997. doi:10.1126/science.276.5321.2012.

[49] Gopalakrishnan Balasubramanian, IY Chan, Roman Kolesov, Mohannad Al-Hmoud, Julia Tisler, Chang Shin, Changdong Kim, Aleksander Wojcik, Philip R Hemmer, Anke Krueger, et al. Nanoscale imaging magnetometry with diamond spins under ambient conditions. *Nature*, 455(7213):648–651, 2008. doi:10.1038/nature07278.

[50] K Jensen, VM Acosta, A Jarmola, and D Budker. Light narrowing of magnetic resonances in ensembles of nitrogen-vacancy centers in diamond. *Physical Review B*, 87(1):014115, 2013. doi:10.1103/PhysRevB.87.014115.

[51] A Dréau, J-R Maze, M Lesik, J-F Roch, and V Jacques. High-resolution spectroscopy of single nv defects coupled with nearby 13 c nuclear spins in diamond. *Physical Review B*, 85 (13):134107, 2012. doi:10.1103/PhysRevB.85.134107.

[52] Philipp Neumann. *Towards a room temperature solid state quantum processor-the nitrogen-vacancy center in diamond*. PhD thesis, 3. Physikalisches Institut der Universität Stuttgart, 2012.

[53] NV Vitanov, BW Shore, L Yatsenko, K Böhmer, T Halfmann, T Rickes, and K Bergmann. Power broadening revisited: theory and experiment. *Optics communications*, 199(1-4): 117–126, 2001. doi:10.1016/S0030-4018(01)01495-X.

[54] A Jarmola, VM Acosta, K Jensen, S Chemerisov, and D Budker. Temperature-and magnetic-field-dependent longitudinal spin relaxation in nitrogen-vacancy ensembles in diamond. *Physical review letters*, 108(19):197601, 2012. doi:10.1103/PhysRevLett.108.197601.

[55] Jeronimo R Maze, Anaïs Dréau, Victor Waselowski, Hector Duarte, Jean-François Roch, and Vincent Jacques. Free induction decay of single spins in diamond. *New Journal of Physics*, 14(10):103041, 2012. doi:10.1088/1367-2630/14/10/103041.

[56] Nicolaas Bloembergen, Edward Mills Purcell, and Robert V Pound. Relaxation effects in nuclear magnetic resonance absorption. *Physical review*, 73(7):679, 1948. doi:10.1103/PhysRev.73.679.

[57] Erwin L Hahn. Spin echoes. *Physical review*, 80(4):580, 1950. doi:10.1103/PhysRev.80.580.

[58] L Childress, MV Gurudev Dutt, JM Taylor, AS Zibrov, F Jelezko, J Wrachtrup, PR Hemmer, and MD Lukin. Coherent dynamics of coupled electron and nuclear spin qubits in diamond. *Science*, 314(5797):281–285, 2006. doi:10.1126/science.1131871.

[59] Lorenza Viola and Seth Lloyd. Dynamical suppression of decoherence in two-state quantum systems. *Physical Review A*, 58(4):2733, 1998. doi:10.1103/PhysRevA.58.2733.

[60] Herman Y Carr and Edward M Purcell. Effects of diffusion on free precession in nuclear magnetic resonance experiments. *Physical review*, 94(3):630, 1954. doi:10.1103/PhysRev.94.630.

[61] Saul Meiboom and David Gill. Modified spin-echo method for measuring nuclear relaxation times. *Review of scientific instruments*, 29(8):688–691, 1958. doi:10.1063/1.1716296.

[62] Terry Gullion, David B Baker, and Mark S Conradi. New, compensated carr-purcell sequences. *Journal of Magnetic Resonance (1969)*, 89(3):479–484, 1990. doi:10.1016/0022-2364(90)90331-3.

[63] Michael Loretz, JM Boss, Tobias Rosskopf, HJ Mamin, D Rugar, and Christian L Degen. Spurious harmonic response of multipulse quantum sensing sequences. *Physical Review X*, 5(2):021009, 2015. doi:10.1103/PhysRevX.5.021009.

[64] Nan Zhao, Jan Honert, Bernhard Schmid, Michael Klas, Junichi Isoya, Matthew Markham, Daniel Twitchen, Fedor Jelezko, Ren-Bao Liu, Helmut Fedder, et al. Sensing single remote nuclear spins. *Nature nanotechnology*, 7(10):657, 2012. doi:10.1038/nnano.2012.152.

[65] TH Taminiau, JJT Wagenaar, T Van der Sar, F Jelezko, Viatcheslav V Dobrovitski, and R Hanson. Detection and control of individual nuclear spins using a weakly coupled electron spin. *Physical review letters*, 109(13):137602, 2012. doi:10.1103/PhysRevLett.109.137602.

[66] J Casanova, Z-Y Wang, JF Haase, and MB Plenio. Robust dynamical decoupling sequences for individual-nuclear-spin addressing. *Physical Review A*, 92(4):042304, 2015. doi:10.1103/PhysRevA.92.042304.

[67] Andreas Albrecht and Martin B Plenio. Filter design for hybrid spin gates. *Physical Review A*, 92(2):022340, 2015. doi:10.1103/PhysRevA.92.022340.

[68] Zhen-Yu Wang, Jacob E Lang, Simon Schmitt, Johannes Lang, Jorge Casanova, Liam McGuinness, Tania S Monteiro, Fedor Jelezko, and Martin B Plenio. Randomization of pulse phases for unambiguous and robust quantum sensing. *Physical review letters*, 122(20): 200403, 2019. doi:10.1103/PhysRevLett.122.200403.

[69] Fazhan Shi, Qi Zhang, Boris Naydenov, Fedor Jelezko, Jiangfeng Du, Friedemann Reinhard, and Jörg Wrachtrup. Quantum logic readout and cooling of a single dark electron spin. *Physical Review B*, 87(19):195414, 2013. doi:10.1103/PhysRevB.87.195414.

[70] Arthur Schweiger and Gunnar Jeschke. *Principles of pulse electron paramagnetic resonance*. Oxford University Press on Demand, 2001. doi:10.1007/BF03166113.

[71] MS Grinolds, M Warner, Kristiaan De Greve, Yuliya Dovzhenko, L Thiel, Ronald Lee Walsworth, Sungkun Hong, P Maletinsky, and Amir Yacoby. Subnanometre resolution in three-dimensional magnetic resonance imaging of individual dark spins. *Nature nanotechnology*, 9(4):279, 2014. doi:10.1038/NNANO.2014.30.

[72] Emma L Rosenfeld, Linh M Pham, Mikhail D Lukin, and Ronald L Walsworth. Sensing coherent dynamics of electronic spin clusters in solids. *Physical review letters*, 120(24): 243604, 2018. doi:10.1103/PhysRevLett.120.243604.

[73] P Neumann, R Kolesov, B Naydenov, J Beck, F Rempp, M Steiner, V Jacques, G Balasubramanian, ML Markham, DJ Twitchen, et al. Quantum register based on coupled electron spins in a room-temperature solid. *Nature Physics*, 6(4):249–253, 2010. doi:10.1038/NPHYS1536.

[74] Bernhard Grotz, Johannes Beck, Philipp Neumann, Boris Naydenov, Rolf Reuter, Friedemann Reinhard, Fedor Jelezko, Jörg Wrachtrup, David Schweinfurth, Biprajit Sarkar, et al. Sensing external spins with nitrogen-vacancy diamond. *New Journal of Physics*, 13(5):055004, 2011. doi:10.1088/1367-2630/13/5/055004.

[75] Russell G Larsen and David J Singel. Double electron–electron resonance spin–echo modulation: Spectroscopic measurement of electron spin pair separations in orientationally disordered solids. *The Journal of chemical physics*, 98(7):5134–5146, 1993. doi:10.1063/1.464916.

[76] Yu D Tsvetkov, Aleksandr Dmitrievich Milov, and Aleksandr Georgievich Maryasov. Pulsed electron–electron double resonance (peldor) as epr spectroscopy in nanometre range. *Russian Chemical Reviews*, 77(6):487, 2008. doi:10.1070/RC2008v077n06ABEH003782.

[77] Peter P Borbat, Elka R Georgieva, and Jack H Freed. Improved sensitivity for long-distance measurements in biomolecules: five-pulse double electron–electron resonance. *The journal of physical chemistry letters*, 4(1):170–175, 2013. doi:10.1021/jz301788n.

[78] Abdelghani Laraoui, Jonathan S Hodges, Colm A Ryan, and Carlos A Meriles. Diamond nitrogen-vacancy center as a probe of random fluctuations in a nuclear spin ensemble. *Physical Review B*, 84(10):104301, 2011. doi:10.1103/PhysRevB.84.104301.

[79] Timo Weggler, Christian Ganslmayer, Florian Frank, Tobias Eilert, Fedor Jelezko, and Jens Michaelis. Determination of the three-dimensional magnetic field vector orientation with nitrogen vacany centers in diamond. *Nano Letters*, 2020. doi:10.1021/acs.nanolett.9b04725.

[80] Jan M Binder, Alexander Stark, Nikolas Tomek, Jochen Scheuer, Florian Frank, Kay D Jahnke, Christoph Müller, Simon Schmitt, Mathias H Metsch, Thomas Unden, et al. Qudi: A modular python suite for experiment control and data processing. *SoftwareX*, 6:85–90, 2017. doi:10.1016/j.softx.2017.02.001.

[81] X-D Chen, C-H Dong, F-W Sun, C-L Zou, J-M Cui, Z-F Han, and G-C Guo. Temperature dependent energy level shifts of nitrogen-vacancy centers in diamond. *Applied Physics Letters*, 99(16):161903, 2011. doi:10.1063/1.3652910.

[82] Ariful Haque and Sharaf Sumaiya. An overview on the formation and processing of nitrogen-vacancy photonic centers in diamond by ion implantation. *Journal of Manufacturing and Materials Processing*, 1(1):6, 2017. doi:10.3390/jmmp1010006.

[83] Linh M Pham, Stephen J DeVience, Francesco Casola, Igor Lovchinsky, Alexander O Sushkov, Eric Bersin, Junghyun Lee, Elana Urbach, Paola Cappellaro, Hongkun Park, et al. Nmr technique for determining the depth of shallow nitrogen-vacancy centers in diamond. *Physical Review B*, 93(4):045425, 2016. doi:10.1103/PhysRevB.93.045425.

[84] BJ Maertz, AP Wijnheijmer, GD Fuchs, ME Nowakowski, and DD Awschalom. Vector magnetic field microscopy using nitrogen vacancy centers in diamond. *Applied Physics Letters*, 96(9):092504, 2010. doi:10.1063/1.3337096.

[85] Jennifer M Schloss, John F Barry, Matthew J Turner, and Ronald L Walsworth. Simultaneous broadband vector magnetometry using solid-state spins. *Physical Review Applied*, 10(3): 034044, 2018. doi:10.1103/PhysRevApplied.10.034044.

[86] Feng-Jian Jiang, Jian-Feng Ye, Zheng Jiao, Zhi-Yong Huang, and Hai-Jiang Lv. Estimation of vector static magnetic field by a nitrogen-vacancy center with a single first-shell 13c nuclear (nv–13c) spin in diamond. *Chinese Physics B*, 27(5):057601, 2018. doi:10.1088/1674-1056/27/5/057601.

[87] Christian Steinhauer, Ralf Jungmann, Thomas L Sobey, Friedrich C Simmel, and Philip Tinnefeld. Dna origami as a nanoscopic ruler for super-resolution microscopy. *Angewandte Chemie International Edition*, 48(47):8870–8873, 2009. doi:10.1002/anie.200903308.

[88] Fazhan Shi, Fei Kong, Pengju Zhao, Xiaojun Zhang, Ming Chen, Sanyou Chen, Qi Zhang, Mengqi Wang, Xiangyu Ye, Zhecheng Wang, et al. Single-dna electron spin resonance spectroscopy in aqueous solutions. *Nature Methods*, 15(9):697–699, 2018. doi:10.1038/s41592-018-0084-1.

[89] Tao Zhang, Andre Neumann, Jessica Lindlau, Yuzhou Wu, Goutam Pramanik, Boris Naydenov, Fedor Jelezko, Florian Schüder, Sebastian Huber, Marinus Huber, et al. Dna-based self-assembly of fluorescent nanodiamonds. *Journal of the American Chemical Society*, 137(31):9776–9779, 2015. doi:10.1021/jacs.5b04857.

[90] Dinar Abdullin and Olav Schiemann. Pulsed dipolar epr spectroscopy and metal ions: Methodology and biological applications. *ChemPlusChem*, 2020. doi:10.1002/cplu.201900705.

List of Publications

[i] Thomas Unden, Nikolas Tomek, Timo Weggler, Florian Frank, Paz London, Jonathan Zopes, Christian Degen, Nicole Raatz, Jan Meijer, Hideyuki Watanabe, Kohei M Itoh, Martin B Plenio, Boris Naydenov, Fedor Jelezko. Coherent control of solid state nuclear spin nano-ensembles. *npj Quantum Information, 4(1):1-6*, 2018.

[ii] Timo Weggler, Christian Ganslmayer, Florian Frank, Tobias Eilert, Fedor Jelezko, and Jens Michaelis. Determination of the three-dimensional magnetic field vector orientation with nitrogen vacancy centers in diamond. *Nano Letters*, 2020.

List of Conferences

IQST day 2019	Oral Presentation	Probing Magnetic Fields with NVs in Diamond
IQST day 2018	Poster Presentation	Structural information of biological macromolecules using a single quantum sensor 2.0
IQST day 2017	Poster Presentation	Structural information of biological macromolecules using a single quantum sensor 1.0